Investigation of supramolecular assemblies based on *de novo* coiled coil peptidic scaffolds

Inaugural-Dissertation

To obtain the academic degree

Doctor rerum naturalium (Dr. rer. nat)

Submitted to the Department of Biology, Chemistry and Pharmacy

of Freie Universität Berlin

by

Ana Rita de Lima Fernandes

First reviewer: Prof. Dr. Beate Koksch (Freie Universität Berlin)

Second reviewer: Prof. Dr. Kevin Pagel (Freie Universität Berlin)

Disputation: 17.09.2019

Declaration

This PhD thesis was carried out from April 2015 to April 2019 under supervision of Prof. Dr. Beate Koksch at the Institute of Chemistry and Biochemistry in the Department of Biology, Chemistry and Pharmacy of Freie Universität Berlin.

I declare that this PhD thesis was prepared autonomously. Third party content, quotes or images are referred to the original work. Additional contributions are:

- Electron microscopy studies were acquired by PD Dr. Christoph Böttcher and Dorian Mikolajczak at the BioSupraMol core facility of Freie Universität Berlin (Germany).
- UV-vis absorbance and fluorescence studies were performed in collaboration with Dr. Hans von Berlepsch.
- Infrared nano-spectroscopy were performed by Katerina Kanevche and Emanuel Pfitzner from the Department of Physics, Freie Universität Berlin, Arnimallee 14, 14195 Berlin.
- Computational modelling was performed by Natalia Ernst and PD Dr. Marcus Weber from the Zuse Institute Berlin (ZIB), Takustrasse 7, 14195 Berlin.
- ^{19}F MRI was performed by Dr. Sonia Waiczies and Dr. Min-Chi Ku from the Berlin Ultrahigh Field Facility, Max Delbrück Center for Molecular Medicine, Berlin, Germany.

Publications

Vukelić, S., Moschner, J., Huhmann, S., **Fernandes, R.**, Berger, A.A., and Koksch, B., *Synthesis of side-chain fluorinated amino acids and their effects on the properties of peptides and proteins*, in Modern Synthesis Processes and Reactivity of Fluorinated Compounds: Progress in Fluorine Science, 1st Ed., 2016.

Posters

Rita Fernandes, Natalia Ernst, Hans v. Berlepsch, Dorian J. Mikolajczak, Marcus Weber, Christoph Böttcher, Beate Koksch, '*pH triggers the assembly of a helical peptide into distinct microscale ordered structures*', 8th Peptide Engineering Meeting, 8th-10th November 2018, Berlin. **Wiley Poster Prize.**

Presentations

Fluorination of self-assembling peptides, FLUORINE21 5th Scientific Training Workshop, Gothemburg, Sweden, June 2017.

Protein Engineering Through Fluorinated Amino Acids, FLUORINE21 3rd Scientific Training Workshop, Münster, Germany, November 2016.

Fluorine in Peptide and Protein Engineering, XV Iberian Peptide Meeting, Porto, Portugal, February 2016.

Protein Engineering Through Fluorinated Amino Acids, GRK 1582 Kollegseminar, Berlin, Germany, January 2016.

Fluorine Modification of Ubiquitin, FLUORINE21 2nd Scientific Training Workshop, Dublin, Ireland, September 2015.

Acknowledgements

I would like to thank my supervisor Prof. Dr. Beate Koksch for giving me the opportunity to do my research work in her group. I am thankful for her support and for the freedom to develop a new research area in her group.

Many thanks to my collaboration partners Dr. Marcus Weber, Natalia Ernst, Katerina Kanevche, Emanuel Pfitzner and Dr. Hans von Berlepsch for the valuable work and fruitful discussions. A special thanks to Dr. Christoph Böttcher for his guidance and great contribution for the development of the projects described in this thesis.

I would like to thank current and past members of the Koksch group, for all the help and good atmosphere throughout these years. A special thanks to Elsa, Jason and Stella for the friendship since day one. Thank you, Dorian and Jakob, for all your help in the lab and for all the good moments outside of it. Thank you, Dr. Allison Berger, for proof-reading the thesis and for the valuable comments.

Thank you for my family and friends in Portugal, who have believed in me and supported me throughout these years away from home.

A big thanks to my friends in Germany and to my friends from the Fluor21 network.

Most of all, I am thankful for Tony. Thank you for the constant care, love and laughs.

Abstract

The ability of peptides to self-assemble into defined supramolecular structures has been of interest to scientists for decades. The expansion of our understanding of the relationships between amino acid sequence and assembly has been accompanied by a growing number of supramolecular structures. There are still, however, some challenges that must be overcome for these materials to be suitable for real-world applications. In particular, the development of simple scaffolds that can self-assemble into stable and ordered structures in a controllable and predictable manner must continue to be pursued.

In this context, the results presented in this thesis reports on the development of new, simple and robust coiled-coil peptidic scaffolds that can assemble into different micro- and nanoscale structures. The highlight of this work is the development of a simple 29-mer coiled-coil Cy5 dye conjugate that undergoes stimuli-triggered aggregation resulting in the formation of microscale membranes and rods under acidic and neutral pH conditions, respectively. Spectroscopic and electron microscopy analyses revealed that the presence of Cy5 at the *N*-terminus was crucial for the formation of high aspect ratio assemblies, whereas peptide sequence governed responsiveness towards pH and structural morphology. Subsequently, a series of newly designed sequences were synthesized and tested to further understand the underlying driving forces for assembly, and to manipulate peptide stability and self-assembly. The first redesigned series aimed to study the impact of substitution of Cy5 with analogous but simpler aromatic systems. It was found that only a compromise between hydrophobicity, charge, and size of the aromatic moieties leads to high order assemblies. In the second redesigned series, the substitution of residues within the hydrophobic core with a fluorinated amino acid or a natural analogue were performed in an attempt to improve peptide stability. The findings showed that the nature and the packing of the side-chains in the helical core were critical for peptide stability and for pH-sensitive aggregation. The final redesign aimed to study the influence of residues placed in solvent exposed positions of the coiled-coil motif on peptide conformation and stability. The results demonstrated that the nature of substitution does not affect the secondary conformation. However, peptides possessing an overall positive net charge exhibit higher thermal stability.

The peptides presented here enable the development of pH-sensitive supramolecular structures, which have potential applications in biomedicine or material sciences.

Zusammenfassung

Die Fähigkeit von Peptiden, sich in definierte supramolekulare Strukturen zu organisieren erregt die Aufmerksamkeit von Wissenschaftlern bereits seit Jahrzehnten. Die Erweiterung unseres Verständnisses der Beziehungen zwischen Aminosäuresequenz und räumlichen Aufbau wurde von einer wachsenden Anzahl von supramolekularen Strukturen begleitet. Es gibt jedoch noch einige Herausforderungen, die zu bewältigen sind, damit diese Materialien für reale Anwendungen verwendbar sind. Insbesondere die Entwicklung einfacher Gerüste, die sich zu stabilen und geordneten Strukturen in einer kontrollierbaren und vorhersehbaren Weise selbst anordnen können, muss weiterverfolgt werden.

In diesem Zusammenhang berichteten die in dieser Arbeit vorgestellten Ergebnisse über die Entwicklung neuer, einfacher und robuster Coiled-Coil-Peptidgerüste, die zu unterschiedlichen Strukturen im Mikro- und Nanomaßstab zusammengesetzt werden können. Das Highlight dieser Arbeit ist die Entwicklung eines einfachen 29-mer-Coiled-Coil-Cy5-Farbstoff Konjugats, das eine reizausgelöste Aggregation erfährt, die im sauren pH Bereich zu einer Bildung von Membranen, und im neutralen zu einer Bildung von Stäben im Mikromaßstab führt. Spektroskopische und elektronenmikroskopische Analysen zeigten, dass das Vorhandensein von Cy5 am *N*-Terminus entscheidend für die Bildung von Anordnungen mit hohem Seitenverhältnis ist, während die Peptidsequenz die Empfindlichkeit gegenüber pH-Wert und Strukturmorphologie steuert. Darauffolgend wurde eine Serie von neu gestalteten Sequenzen synthetisiert und untersucht, um die zugrunde liegenden treibenden Kräfte für die Anordnung zu verstehen, und die Peptidstabilität und Selbstanordnung zu manipulieren. Die erste überarbeitete Serie zielte darauf ab, die Auswirkungen der Substitution von Cy5 mit analogen, aber einfacheren aromatischen Systemen zu untersuchen. Es wurde festgestellt, dass nur ein Kompromiss zwischen Hydrophobie, Ladung und Größe der aromatischen Einheiten zu Strukturen höherer Ordnung führen. In der Bestrebung die Peptidstabilität zu verbessern, wurden in der zweiten überarbeiteten Serie die Reste innerhalb des hydrophoben Kerns mit einer fluorierten Aminosäure oder einem natürlichen Analog substituiert. Die Ergebnisse zeigten, dass die Beschaffenheit und die Packung

der Seitenketten im hydrophoben helikalen Kern entscheidend für die Peptidstabilität und für pH-sensitive Aggregation sind. Die letzte Neugestaltung zielte darauf ab, den Einfluss lösungsmittelexponierter Reste des Coiled-Coil Motifs auf die Peptidkonformation und -Stabilität zu untersuchen. Die Ergebnisse zeigten, dass die Art des Substituenten die sekundäre Konformation nicht beeinflusst. Peptide, die eine positive Gesamtladung aufweisen, zeigten jedoch eine höhere thermische Stabilität.

Die hier vorgestellten Peptide ermöglichen die Entwicklung pH-sensitiver supramolekularer Strukturen, mit potenziellen Anwendungen in der Biomedizin und den Materialwissenschaften.

Symbols and Abbreviations

Å	Angstrom (1 Å = 10^{-10} m)
aa	amino acid
ac.	acetylated
AFM	atomic force microscopy
ATR	attenuated total reflection
Boc	*tert*-butyloxycarbonyl
calc.	calculated
CD	circular dichroism
DCM	dichloromethane
DIC	diisopropylcarbodiimide
DIPEA	*N*,*N*-diisopropylethylamine
DMF	dimethylformamide
eq.	equivalents
ESI	electron spray ionization
ESI-ToF	electron spray ionization - time of flight
Et_2O	diethyl ether
FAA(s)	fluorinated amino acid(s)
FL	fluorescence
Fmoc	9-*N*-fluorenylmethyloxycarbonyl
HATU	1-[bis(dimethylamino)methylene]-1*H*-1,2,3-triazolo[4,5-b]pyridinium3-oxide hexafluorophosphate
HCTU	*O*-(1*H*-6-Chlorobenzotriazole-1-yl)-1,1,3,3-tetramethyluronium hexafluorophosphate
HFIP	1,1,1,3,3,3-hexafluoro-2-propanol
HOAt	1-hydroxy-7-azabenzotriazole
HOBt	1-hydroxy-benzotriazole
HPLC	high performance liquid chromatography
IR	infrared
LD	linear dichroism
m/*z*	mass per charge
MD	molecular dynamics
MeCN	acetonitrile
MeOH	methanol

MRE	molar residual ellipticity
MS	mass spectrometry
M_W	molecular weight
obs.	observed
PDB	protein data bank
Pip	piperidine
pK_a	negative logarithmic acid dissociation constant
RP-HPLC	reversed phase high performance liquid chromatography
rpm	rotations per minute
rt	room temperature
SPPS	solid phase peptide synthesis
TBTU	*O*-(Benzotriazol-1-yl)-*N*,*N*,*N*',*N*'-tetramethyluronium tetrafluoroborate
*t*Bu	*tert*-Butyl
TEM	transmission electron microscopy
TFA	trifluoroacetic acid
TFE	2,2,2-trifluoroethanol
TIS	triisopropylsilane
T_M	melting temperature
UV	ultraviolet
vdW	van der Waals
λ	wavelength

Abbreviations of the 20 canonical amino acids are in accordance with the one- and three-letter code recommended by the IUPAC-IUB Joint Commission on Biochemical Nomenclature (JCBN) [*Eur. J. Biochem.* **1984**, *138*, 9–37].

Abbreviations for fluorinated amino acids used in this thesis are given below. The abbreviations correspond to the L-amino acids.

(3*R*)-4^3-F_3Val (2*S*,3*R*)-4,4,4-trifluorovaline

IUPAC: (2*S*,3*R*)-2-amino-4,4,4-trifluoro-3-methylbutanoic acid

(3*S*)-4^3-F_3Val (2*S*,3*S*)-4,4,4-trifluorovaline

IUPAC: (2*S*,3*S*)-2-amino-4,4,4-trifluoro-3-methylbutanoic acid

Table of Contents

1. Introduction

Supramolecular structures are abundant throughout natural systems. One example is protein fibrous structures that are vital elements of eukaryotic cells and that can be found in the cytoskeleton, providing cells with shape, structural support and protection against mechanical stress, and in the extracellular matrix, where they play important roles in cell adhesion, motility, and elasticity.[1–5] Their unique morphology and functions were optimized through millions of years of natural evolution. Inspired by their properties and with the aim of developing simple, tunable and biocompatible scaffolds for applications in medicine and biotechnology, for decades, scientists have been studying and mimicking these naturally occurring constructs.

Supramolecular chemistry, defined by the 1987 Nobel Prize winner Jean-Marie Lehn as the "*chemistry beyond the molecule*", has the goal of the design of simple motifs that can self-assemble through noncovalent interactions in order to create complex and defined structures.[6] The aim of a synthetic chemist is then to predict and control the information stored at the molecular level and to translate it into a nano- or microscale level. Practically speaking, this can be achieved either by a top-down approach, by resolving a problem from high to low level, or by a bottom-up approach, by controlling the assembly of the monomeric units.[7,8] While top-down strategies offer high control and reproducibility, and are commonly used for nanografting and nanolithography, their inherent low resolution and biocompatibility limits their use for the fabrication of biomaterials.[9–11] In contrast, bottom-up processes involve the rational design of simple building blocks that can predictably and controllably self-assemble by a combination of reversible and weak noncovalent forces.[12–14]

In this context, versatility, accessibility, structural and chemical diversity of proteins and peptides have made them suitable units for the development of new materials. In addition, because these biomacromolecules are generally biocompatible, they are promising for applications in drug encapsulation and delivery, tissue regeneration and tissue engineering.[15] Throughout recent years, by *de novo* designing supramolecular aggregates based on peptidic scaffolds, several relationships between sequence, folding, and assembly have been drawn. Generally speaking, synthetic peptide structures can be divided according to the

main individual folding motifs (α-helical or β-sheet) or as peptide amphiphiles (peptides functionalized with different chemical moieties). To date, most artificial constructs are based on the β-sheet motif. However, because of the more straightforward relationships between sequence and structure, a growing effort is being made in the area of self-assembly coiled-coil scaffolds, with several successful examples of fibers and hydrogels being reported in literature.[7,16]

Different strategies can be explored to promote and control peptide self-assembly. For example, an increase in the hydrophobic character of a peptide through introduction of fluorinated variants of natural amino acids or the conjugation of aromatic systems often results in the increase of peptide stability and propensity to self-assemble.[17,18] An alternative approach is to take advantage of the weak nature of noncovalent interactions and altering them with external stimuli, such as pH, temperature, ionic strength, and light.[19] Nevertheless, despite all the advancements, there are some limitations in this area of research. In particular, simpler morphologies and functionalized structures must still be developed to improve suitability for real-world applications.

In this context, this thesis describes the *de novo* design and characterization of new coiled-coil scaffolds that respond to pH and temperature stimuli.

2. Peptide-based supramolecular assembly

2.1. Peptide self-assembly

Owing to their chemical, functional and structural diversity, predictable sequence-to-structure relationship, biocompatibility, and easy and straightforward synthesis, peptides are ideal scaffolds for the development of highly defined and tunable structures.[8,13,20–25] Peptides are known to self-assemble into a wide variety of structures, such as fibrils, fibers, vesicles, membranes and fibrillar networks (gels) (**Figure 2.1**). Peptide-based materials are predominantly made of α-helix or β-sheet peptides, the two main folding motifs, and to a lesser extent peptide hybrid materials. Examples include peptide amphiphiles where an alkyl chain is attached to a peptide, and short aromatic peptide amphiphiles.[26]

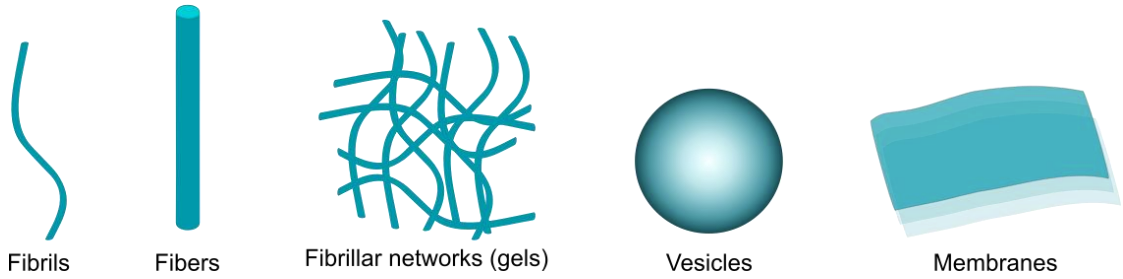

Figure 2.1. Examples of peptide-based self-assembly structures.

Self-assembly is mediated by a combination of weak non-covalent interactions that include hydrophobic and electrostatic interactions, hydrogen bonding, van der Waals (vdW) and π–π stacking.[27] In a peptidic context, different interactions can be easily introduced using different classes of amino acids (**Table 2.1**). Nonpolar (e.g. leucine, isoleucine, valine) and aromatic (phenylalanine, tyrosine and tryptophan) amino acids are the main mediators of hydrophobic interactions and π–π stacking, respectively. Polar (e.g. serine, threonine, glutamine) and ionizable (e.g. lysine, glutamic acid, arginine) residues can form hydrogen bonding and electrostatic interactions, respectively. In addition, peptide assembly can also be influenced by disulfide bonds between cysteine residues or conformationally constrained residues such as proline or glycine.[19]

Table 2.1. Types of noncovalent interactions promoted by canonical amino acids and their dependence. Based on Mart *et al.*[19]

Interaction	Amino acid(s)	Influenced by
Electrostatic	Arginine, Aspartic acid, glutamic acid, histidine and lysine	pH
Hydrophobic effect	Alanine, isoleucine, leucine, methionine, phenylalanine, tryptophan, tyrosine and valine	Solvent, ionic strength, temperature
Hydrogen bonding	Asparagine, glutamine, serine, threonine	Solvent, temperature

When combined, these dynamic interactions direct a peptide's structural conformation and its interaction with the environment.[8,27] Furthermore, these interactions can be rationally triggered by local external stimuli, such as pH, temperature, ionic strength, light, or by the addition of metals.[19,28–30]

2.2. Coiled-coil scaffolds

2.2.1. The α–helical coiled coil motif

In pioneering work published in the 1950s, Crick suggested that α-helices do not pack together as straight rods, but instead they twist around each other forming a super-helix, also referred to as *coiled-coil* (**Figure 2.2**).[31,32] However, it was only in 1991 that the first crystal structure of a parallel dimeric coiled-coil was first solved.[33] Since then, coiled-coils have become one of the best-understood protein folding motifs. Proteins relying in this motif have a large variety of sequences, structures and functions: from DNA transcription factors such as GCN4,[34] Jun and Fos,[35] fibrous components of the cytoskeleton (intermediate filament proteins),[36] and as vesicular trafficking of neurotransmitters (SNARE proteins)[37].

Coiled-coils are amphipathic structures characterized by a periodicity of seven amino acids, the *heptad repeat*, denoted as (***abcdefg***)$_n$ (**Figure 2.2 C**). The 3.6 residues per turn and 1.5 Å rise per residue, implies that hydrophobic (*H*) amino acids are usually placed every three or four residues apart from polar (*P*)

residues.[38–40] In most constructs, positions ***a*** and ***d*** are occupied by apolar amino acids (Ala, Ile, Leu, Val). In aqueous environment, two or more helices come together to bury the hydrophobic residues from the solvent forming a hydrophobic interface.[38] Within the core, the amino acids are arranged in a *knob-into-hole*s packing motif: the side chains (the knobs) of one helix are placed into a diamond-shaped arrangement (the holes) formed between the side chains of the neighbouring helix.[32,36] Positions ***e*** and ***g*** are commonly occupied by helix-inducing charged residues (Arg, Glu, Lys). These positions play an important role in peptide assembly as they can form interhelical salt-bridges.[38] The remaining ***b***, ***c*** and ***f*** positions, which are located in the most solvent exposed regions, are commonly occupied with polar or charged residues.[38] These positions can provide additional intrahelical salt-bridges and therefore can also stabilize the helical bundles.

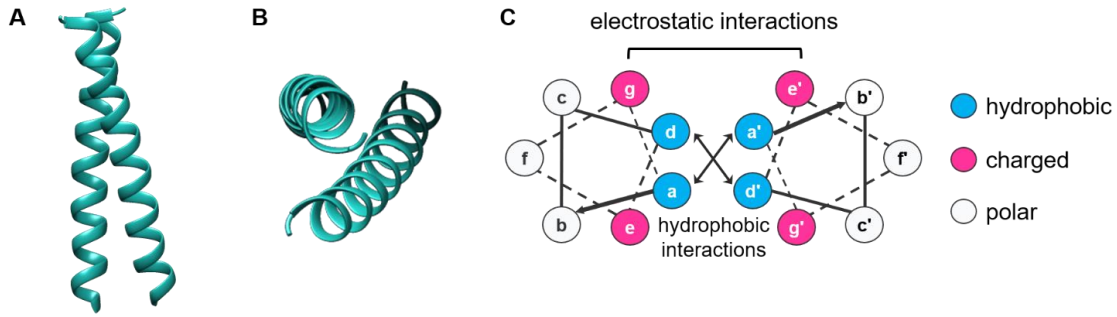

Figure 2.2. The coiled-coil motif. (**A**) Lateral view of a dimeric coiled-coil; (**B**) top-view of a dimeric coiled-coil. (**C**) helical wheel representation of the coiled-coil motif looking down parallel dimeric helices. (for **A** and **B** PDB code: 2zta. Rendered with UCSF Chimera[41]).

The arrangement of Leu or β-branched amino acids within the hydrophobic helical core has a great influence on oligomerization state and helix orientation. Harbury *et al.* demonstrated that in dimeric, trimeric and tetrameric parallel coiled-coils different knob-into-holes packing geometries occur between positions ***a*** and ***d*** (**Figure 2.3**).[42] For dimeric parallel coiled-coils, a perpendicular or a parallel knob-into-holes packing can occur. In perpendicular packing, the side chains of residues at ***d*** positions pack against the side chains of residues at ***d'*** positions, with their Cα-Cβ bond vectors pointing towards the helical interface and each other (**Figure 2.3 A**). This type of packing arrangement excludes the β-branched Ile and Val while favouring Leu residues.[42] In fact, placement of Leu in all ***d*** positions gives the natural

leucine zipper folding motif, with an example being GCN4 (a DNA transcription factor).[34,38] In parallel packing, the side chains of residues at ***a*** positions pack side-by-side with the side chains of residues at ***a'*** positions, with their Cα-Cβ bond vectors pointing away from the interface (**Figure 2.3 B**). In this case, β-branched amino acids are favoured because they project their side chain back into the hydrophobic interface.[38] For tetrameric parallel coiled-coils the packing geometry is reversed, i.e., perpendicular packing in positions ***a*** and parallel in positions ***d***. For trimeric coiled-coils position ***a*** resembles position ***d*** and the angle between both Cα-Cβ bond vectors is intermediate (acute packing, **Figure 2.3 C**).[43] In this case, both branched and unbranched residues are well-tolerated.

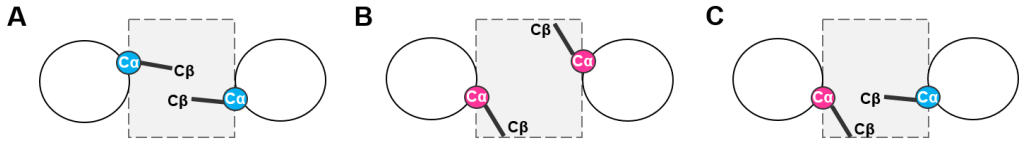

Figure 2.3. Different packing arrangements in parallel coiled-coils. A. Perpendicular packing. **B.** Parallel packing. **C.** Acute packing. (Based on O'Shea *et al*[44] and Harbury *et al*[42]).

The number of helices in coiled-coil bundles can be altered by specific mutations within the helical core. Harbury *et al.* showed that a single residue at ***a*** position (Asn16) of GCN4 promotes dimer formation.[42] The same group reported that a specific mutation within the helix could direct the number of helices between two, three, and four.[42,45] By substituting Asn16 with the polar Gln and Lys, Gonzalez *et al.* showed that the Asn16-Lys retained its ability to exclusively form dimers, while an Asn16-Gln mutant produced a mixture of dimers and trimers.[46] Several other studies have reported on the introduction of polar residues as a tool to direct the helical arrangement of coiled-coils.[47–50] Interhelical interactions between residues in positions ***e*** and ***g*** and intrahelical interactions between these residues and the residues in the hydrophobic core determine coiled-coil orientation (parallel or antiparallel) and specificity (homo- or heteromeric oligomers).[50–54]

As evidenced by the moderately simple and straightforward design rules and the diversity in sequence and structure, coiled-coils are an excellent target for protein engineering and for the design of new biomaterials.

2.2.2. Supramolecular assemblies based on *de novo* coiled coil scaffolds

Significant studies have been directed towards the development of new supramolecular assemblies based on *de novo* designed coiled-coil scaffolds. In 1997, Kojima *et al.* first reported a *de novo* designed coiled-coil peptide capable of self-assembling into fibres of several microns in length and 5–10 nm wide.[55] Interestingly, by reversing the primary sequence the authors reported the formation of more stable and longer fibers.[56] The same group showed that a Leu residue at the *C*-terminus is crucial for helical stabilization and fiber formation.[57]

Potekhin *et al.* developed a blunt ended coiled-coil peptide (α-FFP) that self-assembles into different structures upon pH change.[58] This 34-mer peptide was designed to form pentameric bundles by incorporation of Ala at the ***e*** position. Under acidic pH, long fibrils made up of about 80 peptides with an average 3.0 nm width were formed; at neutral pH, spherical particles with diameters between 10 and 15 nm were observed. Further peptide redesigns, with substitution of the charged residues with uncharged amino acids allowed the assembly into fibrils under physiological conditions.[59] According to the proposed model, each peptide strand is formed by a head-to-tail alignment of each α-helix that wrap around the coiled-coil axis in a left-handed superhelical motif (**Figure 2.4**).

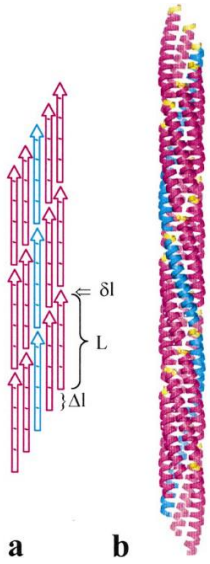

Figure 2.4. Fibril formation model proposed by Potekhin *et al*.[58] (**a**) Two-dimensional representation of the head-to-tail staggering of the each α-helix (pink arrows), with L as the number of amino acids in the peptide sequence, Δl the axial shift and δl the residue equivalents. (**B**) structural model. Reprinted with permission from Potekhin *et al*.[58]

Conticello and co-workers reported a 42-mer α-helical coiled-coil (YZ1) that was able to self-assemble into nanofibrils by a combination of interhelical electrostatic interactions and a staggered placement of the helical strands (*sticky-end* effect previously introduced by Woolfson *et al*.[60]).[61] Fiber formation was achieved by heating peptide solutions to temperatures above the melting point followed by slow peptide annealing to 4 °C. A myriad of techniques including negative staining TEM, wide-angle X-ray diffraction and NMR spectroscopy provided good evidence for an α-helical conformation within the structures. Subsequent peptide redesigns resulted in pH[62] and metal ion[63] switch fibers (**Figure 2.5 A**). In a similar assembly arrangement, Wagner *et al.* introduced a GCN4 derived peptide (CpA) that assembled into nanofilaments and nanoropes.[64] The key design element was the presence of two Ala residues between two heptad repeats that introduced a phase shift in the hydrophobic surface and promoted self-assembly by a staggered arrangement of each helix (**Figure 2.5 D-F**).

More recently, Gribbon *et al.* reported the design of a single α-helical coiled coil peptide (Magic Wand, MW) capable of forming stable and ordered microfibrous architectures to complementary interhelical electrostatic interactions.[65] In the same year, a three heptad long coiled-coil capable of forming nanofibers was reported by the Hartgerink group.[66] The proposed model consisted of a concentration-dependent assembly of blunt-ended coiled-coils that further undergoes longitudinal polymerization into fibrils (**Figure 2.6**). The placement of charged amino acids in the most solvent exposed positions of the coiled-coil domain (positions ***b***, ***c*** and ***f***) allowed for the lateral assembly of the fibrils into fibres. In addition, in neutral pH and high concentrations, the peptides further associate into self-supporting hydrogels.

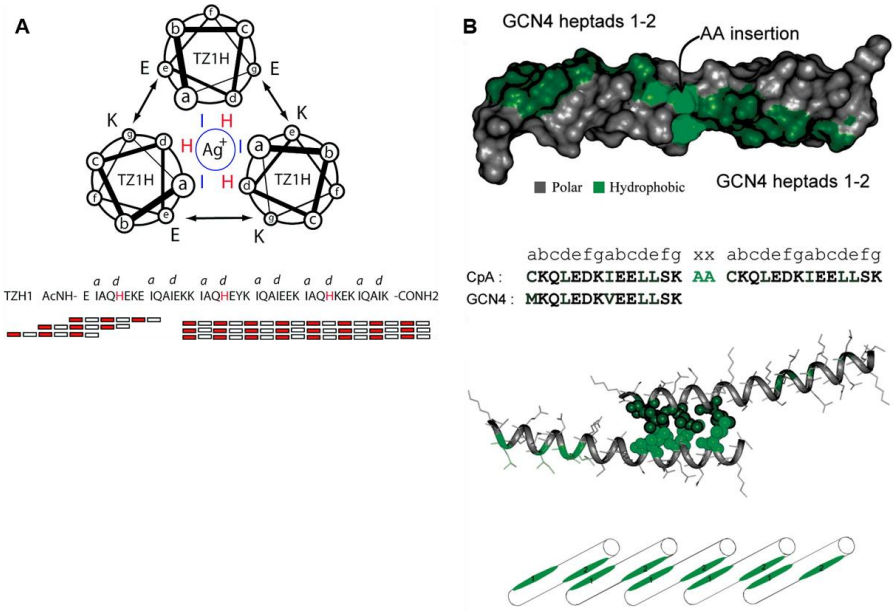

Figure 2.5. Examples of fiber forming homo-oligomeric coiled-coils. A. TZH1, metal ion switch fibers with helical wheel representation of the trimeric coiled-coil system with His residues for Ag^{+} binding sites, and primary sequence and the proposed staggered arrangement of the peptides. **B.** CpA, nanoropes and nanofilaments forming peptide. Surface representation and primary sequence, with hydrophobic residues highlighted in green and proposed phase shift and staggered arrangement of the helices. **A.** Reprinted with permission from Dublin *et al*.[63] Copyright © 2008 American Chemical Society. **B.** Adapted from Wagner *et al*.[64] Copyright 2005 National Academy of Sciences.

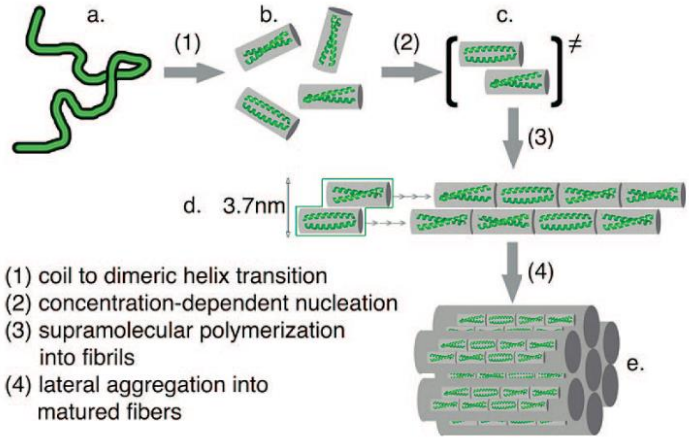

Figure 2.6. Polymerization and fiber formation of a blunt-ended coiled-coil peptide proposed by the Hartgerink group. (Reprinted with permission from Dong *et al*.[66] Copyright © 2008 American Chemical Society).

In contrast to the above examples that mainly report on homo-oligomeric systems, the Woolfson group introduced a heterodimeric system capable of forming gigadalton fibers, the so-called self-assembling fiber peptides (SAF) (**Figure 2.7**).[60] Two 28-mer (SAF-p1 and SAF-p2), derived from the natural GCN4 leucine zipper was able to assemble into microfibrous structures. Electron microscopy of matured SAF solutions revealed thick α-helical fibres with 40-50 nm diameter and several micrometres in length (**Figure 2.7 B, C**).[60] However, the conditions for fiber formation were limited to temperatures up to 15 °C, pH 7.0 and in the absence of salts. With biological applications in mind, the group further altered the SAF system to improve fiber stability and to alter morphology. Co-assembly of the first generation of SAF peptides with a more positively charged peptide (SAF-p2a)[67] or a non-linear peptide (T-SAF)[68] directed the formation of kinked or branched fibers, respectively. Extension of the primary sequence by addition of an extra heptad (SAF-p1-ext, SAF-p2a-ext) resulted in fibers more stable against higher temperatures (up to 65 °C) and ionic strengths (up to 250 mM KCl).[69] In an extension to these studies, the group also introduced a *C*-terminal thioester moiety for chemoselective ligation to a wild-type SAF (SAF-p1E:SAF-p2a; SAF-p1: SAF-p2aE) or a homodimeric self-templating peptide system (STePE).[70]

The key design aspects for the SAF include complementary charged residues in positions ***e*** and ***g*** to promote the lateral association of the peptides, the introduction of one asparagine in different heptads of each peptide, and overhanging ends, or "*sticky-ends*", to promote the longitudinal elongation of the fibers. With cryo-TEM, cryo-tomography, X-ray crystallography, and computational modelling were used to described the structure with 8 Å resolution (**Figure 2.7 D, E**). As previously reported,[71] cryo-TEM imaging confirms order in both the width and the length of the fiber. Several distances were determined: 4.18 nm spaced striations perpendicular to the long fiber axis, that closely corresponds to the value expected for the length of a coiled-coil (the raise per residue in a coiled-coil is 0.148 nm[72]); 1.8 nm spaced striations parallel to the long fiber axis, that corresponds to a hexagonal packing of the coiled-coils; 12.54 nm diffraction pattern that matches the superhelical pitch for the coiled-coil. Taken together, the authors proposed that the SAF coiled-coils are arranged along the length of the fiber in a hexagonal geometry that is mediated by side-chain salt bridges (**Figure 2.7 F**).[73]

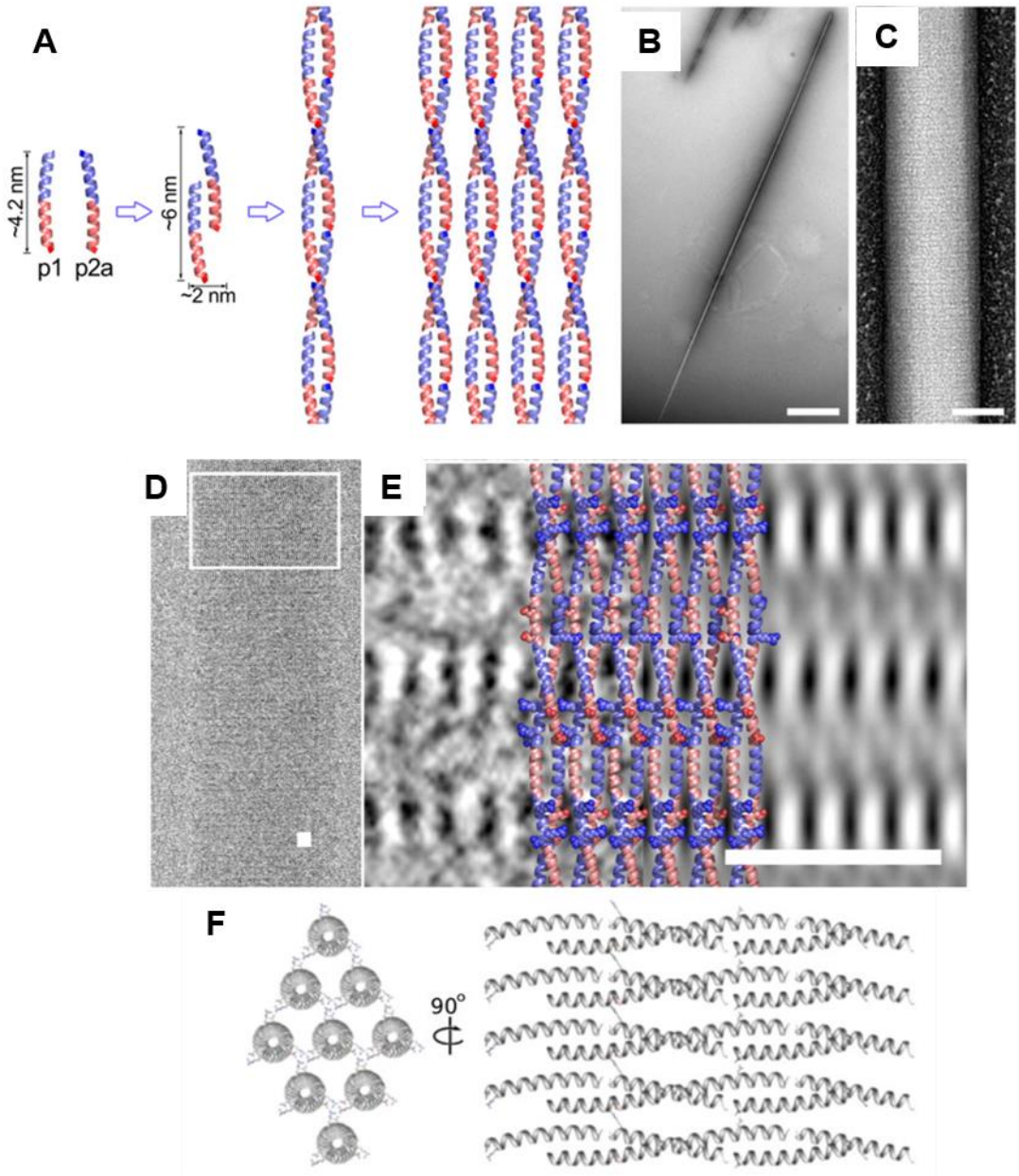

Figure 2.7. Proposed arrangement of self-assembly fiber peptides (SAF) within the gigadalton peptide fibers. (**A**) Two 28-mer coiled-coil peptides co-assemble into heterodimers that further undergo lateral stacking, due to interhelical electrostatic interactions, and longitudinal elongation, due to the sticky-end effect. (**B-C**) Representative transmission electron micrographs of long, unbranched and striated fibers. Scale bars: **B.** 2 µm, **C.** 50 nm. (**D**) cryo-TEM of the gigadalton fibers with region used for detailed analysis; (**E**) Cartoon representation of the coiled-coils along the length of the structure; (**F**) Hexagonal pattern and sticky end arrangement of the SAF. (Reprinted from Sharp *et al*.[73] Copyright 2012 National Academy of Sciences).

In addition to fibrils and fibers, coiled-coils can also assemble into more complex structures such as nanotubes,[74–77] micro-nets,[78] cages,[79] hydrogels,[80] dendrimers,[81] and tetrahedrons[82].

As previously stated, peptide self-assembly can be controlled by applying external stimuli. Apostolovic *et al.* comprehensively collected a large number of examples of coiled-coils sensitive to different environmental cues.[83] Among the different external stimuli, pH variation is perhaps the most commonly used method to trigger or alter supramolecular assembly. In coiled-coils, sensitivity towards pH is easily achieved by incorporating acidic and basic amino acids. In general, the reported coiled-coils show higher helicity and stability when buffered under acidic conditions (pH < 5). In addition, a helix to disordered transition is usually achieved by titration from acidic to neutral conditions. A recent example was reported by Nambiar *et al.* in which is described a trimeric coiled-coil system functionalized with bipyridines capable of reversible assembly into high-order structures upon pH changes (**Figure 2.8**).[84] The robustness of the scaffold was established by the maintenance of helical conformation with the introduction of up to three bipyridines per helix. However, the morphology of the final structures was noticeably different: under benign conditions, the peptides self-assembled into striated high-order structures, that by increasing the bipyridine content per trimer, varied from a rectangular-shaped to a square-shaped morphology. When buffered at pH 3.0, disruption of the supramolecular constructs, likely due to protonation of the bipyridines, and formation of 2−3 nm unassembled trimer coiled-coils was observed. Interestingly, reconversion into the high-order blocks could be achieved over several pH cycles.

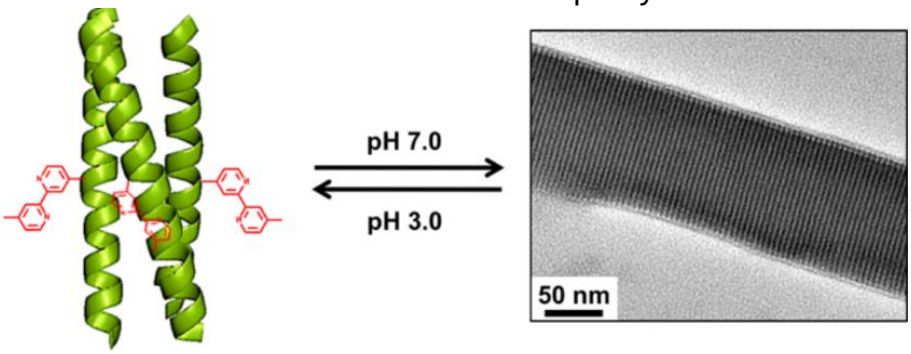

Figure 2.8. Trimeric coiled-coils functionalized with bipyridine showing pH sensitive self-assembly. (Reprinted with permission from Nambiar *et al*.[84] Copyright © 2018 American Chemical Society).

In addition, variation of the ionic strength of peptide solutions can be used not only to change coulombic interactions, and therefore pH sensitivity, but also to promote an increase of thermal stability. Owing to the relationship with hydrophobic effect, temperature can be a powerful tool to drive aggregation,[85] and to promote or accelerate the transition from helical to amyloid conformation.[86] Coiled-coil thermal stability is dependent on the hydrophobic character and length. Other environmental cues such as peptide concentration, solvent, light irradiation, and the addition of metals can also be used to influence peptide assembly.

2.2.3. Applications of supramolecular peptide-based materials

As the field of biomaterials based on peptidic scaffolds is in an emerging stage, their real-life applications are still rare. However, several *in vitro* and small animal studies have demonstrated their potential for applications in drug encapsulation and delivery, biomimetics of cellular components, tissue imaging and tissue engineering.[24,87–89]

A significant proportion of the work in this area has been focused on peptides based on β-sheet forming sequences and peptide amphiphiles. An example was reported by Zhang *et al.* with the formation of nanofibers consisting of a peptide amphiphile capable of encapsulate paclitaxel, a hydrophobic drug used against several types of cancer, and the uptake into cancer cells.[90] Nanofiber formation was only achieved by the conjugation of a truncated cell penetrating peptide (TAT_{48-60})[91] with four octanoic acid (C_8) hydrophobic chains (the introduction of one or two octanoic chains failed to allow the formation of nanofibers). CD analysis revealed that the conjugate adopted a β-sheet conformation. TEM analysis revealed that, despite the maintenance of the width, the nanofibers were less rigid with increased amount of drug loaded within the lumen. Interestingly, Lim *et al.* described a versatile strategy for the self-assembly into spherical or short-length cylindrical micelles by varying the number of hydrophobic chains (in this case of stearic acid, C_{18}) conjugated to TAT.[92] As a proof of concept, the authors reported the successful encapsulation of a hydrophobic dye within the short-length cylindrical micelles.

Coiled-coil based biomaterials have been relatively less reported. Following the classification proposed by Conticello *et al.*, coiled-coil materials exist in two main

categories: those consisting of only peptide or protein scaffolds and those consisting of peptides conjugated to other chemical moieties.[93]

Banwell *et al.* have developed a hydrogelating system (hSAF) based on their previous reported coiled-coil SAF, where the outer-most solvent exposed positions of the coiled-coil were replaced with alanine, to promote hydrophobic interactions, or glutamine, to promote hydrogen bonding.[80] With these alterations, the authors were able to control the thermal stability of the three-dimensional gels, with the glutamine-rich peptide melting upon heating, and the alanine-rich peptide showing a slight increase in strength as function of temperature. Further peptide redesign by the introduction of a tryptophan residue allowed for the formation of biocompatible hydrogels that were able to support cell growth and proliferation. In a following study, the same group reported on the decoration of the hSAF gels with an integrin-binding motif (RGDS) for neural tissue engineering.[94]

Inspired by a hydrogel forming chimeric protein consisting of leucine zipper motifs flanked by dentin matrix protein domain,[95] Huang *et al*. reported a tuneable hydrogelating system for tissue engineering applications.[96] Peptide redesign consisted in a RGDS motif between two six heptad long peptides each with a cysteine at the *N*-terminal (A2), and two 9-mer spacer without (C1) and with a cysteine residue at the C-terminal. The introduction of the RGDS motif into the hydrogel forming system was crucial for a higher level of cell adhesion, cell proliferation and neovascularization.

Zacco *et al*. described a fiber-forming coiled-coil scaffold for the decoration with a glycopeptide ligand for bioanalytical assays in vaccines (**Figure 2.9**).[97] Key coiled-coil design features included the introduction of opposite charged amino acids in positions *b*, *c, e* and *g* to promote peptide stability and induce fiber formation, an extra half heptad repeat at the *N*-terminus to facilitate longitudinal fibre growth, and the introduction of a Lys(Mtt) in position 17 for an orthogonal ligand conjugation. Introduction of the multivalent ligand that consisted on an immunogenic epitope derived from *Diphtheria* toxin[98] and a mannose derivative as carbohydrate was performed still on resin. A series of peptide variants consisting of only coiled-coil and epitope or coiled-coil and sugar were synthesized to study the influence of each moiety. The robustness of the scaffold was confirmed by CD and negative-staining

TEM, with the maintenance of an α-helical conformation and fiber formation upon conjugation with the glycopeptide ligand. All peptide variants readily self-assembled under neutral conditions into long, unbranched fibers with an average 2.5 nm diameter and over 100 nm long; concomitant with the individual fibers, bundles of fibers were also observed. Using different binding assays, Zacco *et al*. shown that the conjugation of the glycopeptide ligand in the fiber scaffold results in an increase binding efficiency against an antidiphtheria toxin antibody than when in the absence of peptide scaffold. The authors attribute the increase in efficiency to a higher density and better organization of the ligand when attached to the coiled-coil scaffold.

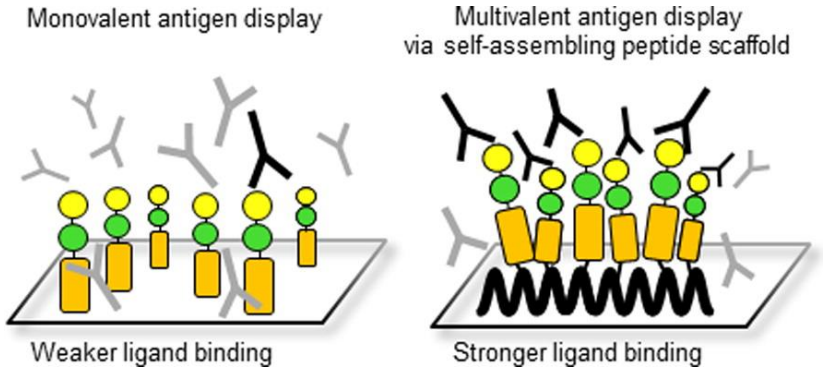

Figure 2.9. Fiber forming coiled-coil scaffold for the decoration with glycopeptide ligand for bioanalytical assays. The decoration of fiber-forming coiled coils (solid black line, left cartoon) with a peptide ligand (yellow rectangle) and carbohydrates (green and yellow circles) results in a stronger binding. (Reprinted with permission from Zacco, E. *et al.*[97] Copyright 2015 American Chemical Society).

Construction of coiled-coil hybrids is usually achieved by introducing a different chemical functionality, usually a polymer or an aliphatic chain. Klok *et al.* have extensively investigated a pH responsive heterodimeric coiled-coil conjugated to polymers[99,100] and hyaluronic acid[101] for cell cargo delivery. The key design element was the use of the previously established heterodimeric E3/K3[102] system that self-assembles under neutral conditions but undergoes unfolding transition at pH 5.[103]

Mikolajczak *et al.* reported the immobilization of the E3/K3 system onto gold nanoparticles for the catalysis of *p*-nitrophenylacetate (*p*NPA) hydrolysis (**Figure 2.10**).[105] The E3 variant was redesigned to include a histidine residue at position 15 (E3H15), thus creating a carboxylate-rich region surrounding the imidazole side-

chain of histidine, and a cysteine at the *N*-terminus, for an easy attachment of the peptide into the gold nanoparticles (Au@E3H15). The local high peptide density provided by the immobilization of an average 265 peptides per nanoparticle resulted in a 11-fold increase in catalytical activity of @AuE3H15 when compared to a solution containing only free E3H15. However, in the presence of equimolar K3, the catalytical activity of either free or immobilized peptide decreased, in particular for the case Au@E3H15 with an average 85 % decrease in catalytical efficiency. The authors attribute this difference to several factors. Namely, the addition of K3 results in a transition from unordered to coiled-coil conformation therefore creating more rigid helices and hindering the formation of binding pockets necessary for accommodating and binding of *p*NPA. In addition, the formation of E315/K3 and @AuE3H15/K3 might further disrupt intermolecular cooperative interactions presumable responsible for the increase in catalytical efficiency of Au@E3H15. Further peptide redesigns included the development of three peptide-Au variants that differed only in the histidine position and their effects on the catalytical activity and substrate specificity,[106] and in the formation of peptide-Au conjugates for a one-pot sequential catalysis of two distinct reactions[107].

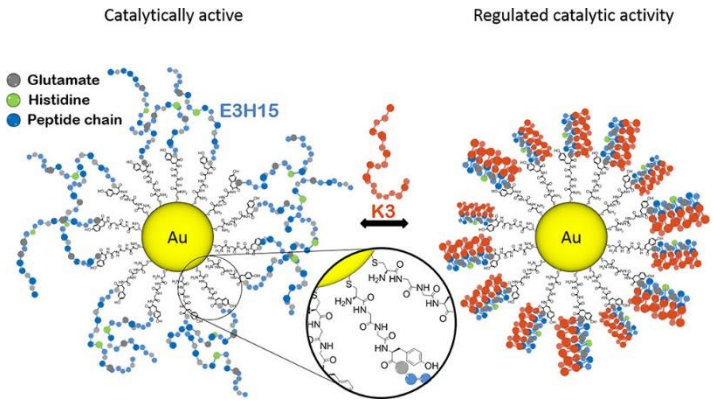

Figure 2.10. Peptide-gold nanoparticle conjugates for ester hydrolysis catalysis. Increased catalytical activity was observed upon immobilization of the histidine-bearing peptide to gold-nanoparticles (Au@E3H15). Regulation of catalytical activity was achieved by addition of the complementary K3. (Reprinted with permission from Mikolajczak, D. J., *et al*.[105] Copyright 2017 American Chemical Society.)

2.3. Fluorine as a modulator of peptides properties

Despite organic fluorides being the least abundant of all naturally occurring organohalides,[108] for decades, incorporation of fluorine into organic compounds is a widely used strategy in several fields. Such applications include organic electronics and solar cells,[109–111] imaging and diagnostic probes (^{18}F PET),[112] reagents and solvents for organic synthesis,[113–115] probes for ^{19}F NMR (nuclear magnetic resonance)[116,117] and ^{19}F MRI (magnetic resonance imaging)[118,119]. However, it´s in the pharmaceutical[108,120,121] and agrochemical[122,123] fields that fluorine has the highest impact with an estimated 20 to 25 % of all drugs[120,121] and 30 % of all agrochemicals[108] possessing at least one fluorine atom. More recently, as the methods to synthesize and to incorporate fluorinated amino acids (FAAs) into peptides and proteins have become more straightforward and powerful, the interest in their use to modulate the physical and chemical properties of these biomacromolecules has increased.[124]

2.3.1. Fluorine: properties and impact in biological relevant molecules

The success of fluorine arises from its peculiar characteristics. Fluorine is the smallest element of Period 2, with a van der Waals radius of 1.47 Å, laying between the radius of hydrogen (1.20 Å) and oxygen (1.52 Å).[125,126] As such, the replacement of hydrogen with fluorine is considered to be sterically conservative, i.e., bioisosteric, and without great disturbance on the steric demand of a molecule.[108,125] Along with this observation, it is well established that increasing the number of fluorine atoms leads to a dramatic increase on the steric demand of alkyl groups.[127] However, the extent to which the steric space is increased is still subject to debate. It was generally accepted that a trifluoromethyl group (CF_3) had the same steric size as an isopropyl group,[127] but with a different shape[108]. More recently it was proposed that the van der Waals (vdW) volume of CF_3 is more closely related to an ethyl group.[108,128,129] Therefore, an higher content of fluorine can alter the preferred conformation of molecules. For example, it has been show that the potency of an inhibitor of cholesteryl ester transfer protein (CETP, a plasma glycoprotein involved in the transference of cholesteryl esters between the lipoproteins[130]) can be

drastically decreased upon substitution of tetrafluoroethyl moiety with a non-fluorinated analogue due to conformational changes in the molecule.[131]

As the most electronegative of all elements, fluorine has a large inductive effect.[124] This property has an enormous consequences on the C-F bond, as it imparts a polarized character and a large dipole moment.[123–125] The average length of a C-F bond is 1.35 Å, a value that again lies between a C-H bond (1.09 Å) and a C-O bond (1.43 Å).[123,125] Substitution of a C-H bond with a C-F bond has dramatic effects. For example, hydroxylation of C-H bonds can be supressed by substitution of a C-H bond with a C-F bond, as in the case of some metabolic processes governed by cytochrome P-450 enzymes.[132]

As result of fluorine's withdrawing effect, the pK_a of surrounding functional groups is directly affected. Therefore, its incorporation can be used to manipulate the acidity or basicity of neighbourhood protic moieties and to delay or inhibit their oxidation.[123,132,133] This is crucial in certain pharmacological events, such as drug absorption and distribution, which are controlled by a balance between charge state and the hydrophobicity.[108] One strategy to improve membrane permeability, and therefore to increase absorption, is to incorporate fluorine near to basic functionalities – known to have limited membrane permeability – as fluorine decreases the pK_a of basic moieties.[108,134]

It´s not surprising that fluorine incorporation is commonly used in the pharmaceutical area. In fact, several of the top selling drugs in the market contain at least one fluorine substituent (**Figure 2.11**).[115,135] In contrast, the use of fluorinated peptide- or peptidomimetic-based drugs is still in its infancy and only few cases of clinical candidates are reported in literature. One example is ulimorelin (**Figure 2.11**), a fluorinated peptidomimetic macrocycle designed as an agonist of a G-protein coupled receptor that showed high potency and good pharmacokinetics in rats, but later failed in trials with primates.[136]

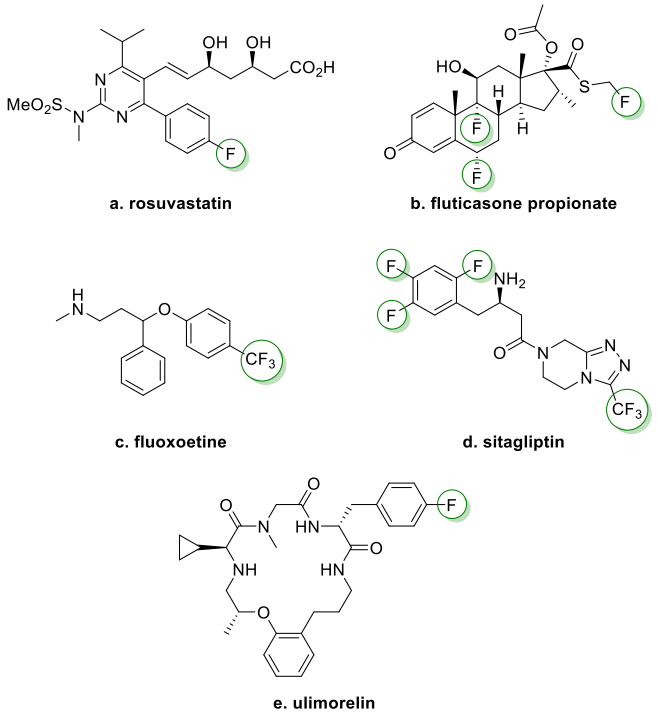

Figure 2.11. Selection of chemical structures from the top selling fluorinated drugs (a-d) and a fluorinated peptidomimetic (e). a. rosuvastatin (trade name *Crestor*), a statin used for the treatment of hypercholesterolemia; **b.** fluticasone propionate that in combination with salmeterol (trade name *Advair Diskus*) is used for the treatment of asthma; **c.** fluoxetine (trade name *Prozac*), an antidepressant drug; **d.** sitaglipin, an antidiabetic drug; **e.** ulimorelin, a fluorinated peptidomimetic clinical candidate.[121,137]

Fluorinated amino acids (FAAs) are an important class of synthetic organic fluorine biomolecules. Since the synthesis of the first fluorine bearing amino acid,[138] FAAs have been used in their free form as ^{19}F-NMR probes for mechanistic enzymatic activity studies,[139] or incorporated into peptides and proteins to modulate their physicochemical properties[140,141]. However, despite all advances in this area, the properties of fluorinated peptides are rarely predictable, greatly depending on the fluorine content and on the incorporation site.

Within this context, the Koksch group has greatly contributed for the development of this field, and while several studies will be described herein, the reader is further referred to the group´s reviews.[124,142–146]

2.3.2. General aspects of fluorinated amino acids

Most studies involve the incorporation of fluorinated derivatives of aliphatic amino acids as the synthetic routes are moderately straightforward and faster (**Figure 2.12**).

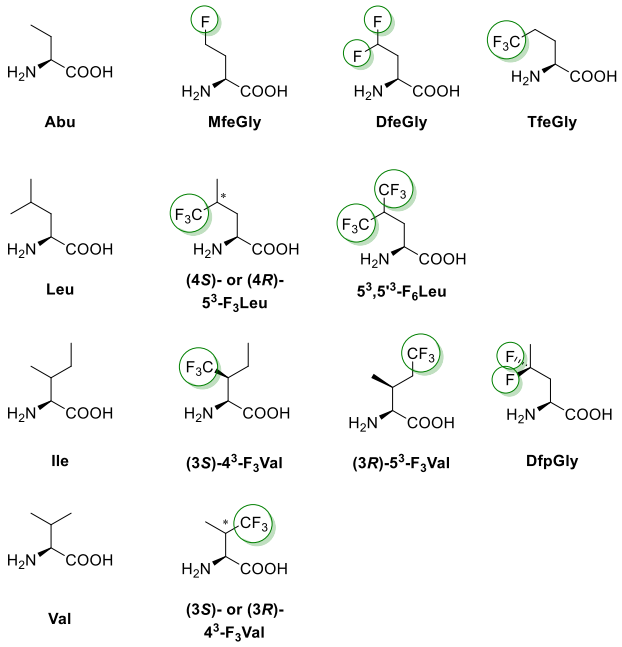

Figure 2.12. Chemical structures of fluorinated analogues of aliphatic amino acids (Abu, Leu, Ile, Val).

There are several important aspects that need to be considered before FAA incorporation. Regardless of the steric similarity between H and F, the hydrophobic character of FAAs is different from their non-fluorinated counterpart. This relationship between size and hydrophobicity can be determined by plotting the calculated vdW volume against the retention time obtained from reverse-phase HPLC assays (**Figure 2.13**).[147–149] For canonical amino acids, the relationship is straightforward: an increase in the side chain volume results in an increase of hydrophobicity, albeit in a non-linear fashion. For FAAs no direct relationship between size and retention time exists. For example, the introduction of one fluorine in the side chain of Abu results in the increase of vdW volume but with the decrease of retention time, i.e., the fluorinated variant is less hydrophobic.[147]

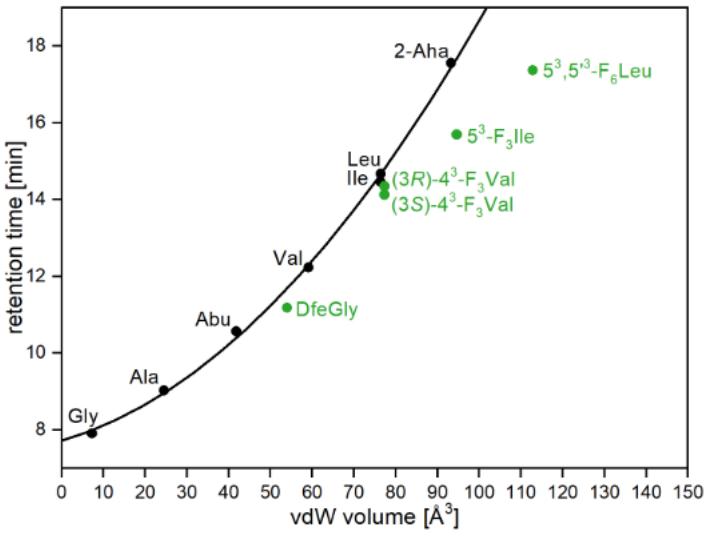

Figure 2.13. Relationship between the van der Waals volume and the retention time by means of reverse-phase HPLC. Reprinted from Huhmann.[150]

In contrast, by increasing the fluorine content to two and three F atoms both size and hydrophobic character increases. Another example are FAAs analogues of Val where both vdW volume of the side chain and retention time increases upon introduction of a trifluoromethyl group. In fact, these amino acids behave more similarly to Leu and Ile.

By combining quantum mechanics and molecular dynamics, it was proposed that introduction of fluorine has two major effects on the hydrophobic character of an amino acid: first, the solvent accessible surface area is increased, resulting in a more favourable hydration energy (less negative); second, the C-F bond is more polarized, resulting in a more energetically favourable electrostatic interaction between F atoms and the solvent.[147,151]

Another important aspect regarding the incorporation FAAs in a peptidic context is the propensity to adopt a specific secondary structure, also referred to as helix propensity. Cheng *et al.* incorporated highly FAAs into a model helical peptide and analysed its impact in the secondary structure by circular dichroism (CD).[152,153] The authors found that fluorination decreases peptide's helicity regarding to their non-fluorinated analogues. More recently, inclusion of different FAAs in the same model peptide gave the same decreasing trend (**Table 2.2**).[148,149,154] Interestingly, these studies show that fluorinated variants of Val show zero helix propensity (**Table 2.2**,

entry 11 and 12). In other words, these amino acids can be better accommodated in a β-sheet conformation.[152]

Chiu *et al.* suggested that the decrease in helix propensity upon fluorine incorporation might be a consequence of the monomeric helix model system in which the fluorinated side chains are exposed to the aqueous solvent, therefore resulting in thermodynamically unfavourable helix formation.[152] This decrease can also be argued with steric arguments. Incorporation of the β-branched Ile and Val causes the side chains to be in close proximity to the peptide backbone, resulting in destabilization of the helical structure when compared with the non-branched Abu and Leu (**Table 2.2**, entry 7 and 10 versus entry 1 and 5); incorporation of the bulkier CF_3 in Ile and Val increases the size of the side chains and abbreviates the distance to the peptide backbone, with further destabilization of the helical structure (**Table 2.2**, entry 8, 9, 11 and 12).[154]

Table 2.2. Calculated fraction of helicity (%) and helix propensity for amino acids and their fluorinated derivatives.

Entry	Amino acid	Fraction of helicity (%)	Helix propensity
1	**Abu**[152,153]	0.522 ± 0.006	1.22 ± 0.14
2	MfeGly[149]	0.48 ± 0.01	0.873 ± 0.068
3	DfeGly[149]	0.40 ± 0.02	0.497 ± 0.060
4	TfeGly[149]	0.22 ± 0.01	0.057 ± 0.022
5	**Leu**[149]	0.502 ± 0.006	1.06 ± 0.12
6	5^3,$5'^3$-F_6Leu[152,153]	0.251 ± 0.006	0.128 ± 0.023
7	**Ile**[148]	0.40 ± 0.01	0.52 ± 0.05
8	4^3-F_3Ile[154]	0.10 ± 0.01	0
9	5^3-F_3Ile[148]	0.31 ± 0.01	0.26 ± 0.03
10	**Val**[154]	0.38 ± 0.01	0.41 ± 0.04
11	(3*S*)-4^3-F_3Val[154]	0.08 ± 0.01	0
12	(3*R*)-4^3-F_3Val[154]	0.11 ± 0.02	0

2.3.3. Incorporation of FAAs in coiled-coils

As previously mentioned in **Section 2.2.1**, it is well established that the major contributor to peptide folding is the hydrophobic effect. This effect stabilizes the folded peptides by burying the hydrophobic residues and exposing the polar residues to the aqueous environment. Since FAAs are *generally* more hydrophobic than their non-fluorinated counterparts, is not surprising that several studies have been focused on the incorporation of fluorinated analogues of Leu, Ile and Val in the hydrophobic positions of coiled-coils to increase peptide stability (**Figure 2.12**).

The first reports of coiled-coil stabilization through incorporation of FAAs were published in the beginning of the 2000's from the groups of DeGrado, Kumar and Tirrell. Tirrell *et al*. studied the incorporation of 5^3-F_3Leu in all ***d*** positions of a GCN4-p1d domain and of 5^3-F_3Ile and 4^3-F_3Val in all ***a*** positions of a *de novo* designed peptide adapted from GCN4, both model peptides capable of DNA binding.[155,156] In all cases, introduction fluorine led to an increased thermal and chemical stability without disturbance of the secondary structure or the ability of the peptides to bind to DNA. In particular, the authors showed that a better accommodation of the branched side-chains of 5^3-F_3Ile within the helical core resulted in an enhanced stabilization of this peptide variant.[156]

By using a different variant of the GCN4 coiled-coil domain, Kumar *et al.* showed that incorporation of diastereomeric mixtures of 5^3-F_3Leu in all ***a*** positions and 4^3-F_3Val in all ***d*** positions, results in both thermal and chemical stabilization regarding to the non-fluorinated wild-type.[157] The authors proposed that the increase on stability might be a consequence of burying the fluorinated moieties apart from the aqueous solvent. The same group also developed a model system comprised of a canonical peptide strand (H) and its fluorinated derivative (F) in which all ***a*** and ***d*** positions were substituted with 5^3,$5'^3$-F_6Leu.[158] The peptides strands were designed to assemble into dimers through disulfide bridges between cysteines positioned at the *N*-terminus, affording homodimeric (HH and FF) and heterodimeric (HF) conjugates. Thermal stability increased with increasing fluorine content (HH < HF < FF). Moreover, the authors showed that subjecting HF to redox conditions resulted in a preferential arrangement into HH and FF dimers, with less 3 % HF. With the almost absent formation of the heterodimeric system, the authors to suggested that

peptide folding is greatly influenced by the "*fluorous effect*" (tendency for perfluorous compounds to self-assemble into a distinct phase apart from aqueous and organic). However, it should be noted that the fluorinated peptide folded into a tetrameric assembly rather than the desired dimeric system, thus complicating the interpretation of the results.

Marsh *et al.* developed an antiparallel tetramer helical model α_4F_n, with *n* as the number of FAAs, in which they systematically introduced 5^3,$5'^3$-F_6Leu in positions ***a*** and ***d*** in the hydrophobic core.[159–161] The inclusion of FAAs did not disturb the folding motif of the peptide variants, although NMR studies suggested that the variants possessing higher fluorine content showed a more structured backbone.[160] Following the same trend as previously described, thermal stability of the peptides increased with the number of fluorinated residues. Importantly, the experimental data showed that stability is position dependant, with higher values for substitutions made at more buried positions on the helical core and also substitutions at all ***a*** or all ***d*** positions.[161] With these results the authors challenged the "fluorous effect" argument by Kumar,[158] by arguing that increased stability is due to the increase of hydrophobicity and an efficient packing of the FAA within the helical core and not because of specific fluorine-fluorine interactions. More recently, the group solved the crystal structures of three tetrameric coiled-coil bundles in which all ***a*** positions were occupied with different FAAs.[162,163] Here, increased stability allied with minimal structural disturbance was observed upon inclusion of the larger FAAs, thus reinforcing the argument that combination between efficient packing and increased hydrophobicity is responsible for the enhanced stability.[162,164]

In contrast, some studies showed that introduction of FAAs causes loss of peptide stability. An example was reported by Montclare *et al*., in which the authors observed a 20-fold loss of thermostability upon replacement of Leu residues with 5^3-F_3Leu in chloramphenicol acetyltransferase (CAT, an enzyme responsible for bacterial resistance against chloramphenicol).[165,166]

The above reported studies deal with the incorporation of several amino acids *per* coiled-coil helix, in which FAAs are usually interacting with FAAs. In contrast, the Koksch group has been focused on interactions between FAAs and canonical amino acids, using single incorporation within the hydrophobic core of model coiled-coils.

To this end, two model systems were developed: a model I comprising of an antiparallel homodimer,[167,168] and a model II comprising of a parallel heterodimer (VPE/ VPK)[169–173]. In both cases, fluorinated analogues of Abu with gradual increase in fluorine content were incorporated into positions ***a*** or ***d*** within the hydrophobic core. The results showed that fluorine's effect strongly depends the fluorine content and on the position of substitution. Namely, introduction of DfeGly, TfeGly, or DfpGly lowered the thermal stability.[170,171] More recently, Huhmann *et al.* showed that 5^3,$5^{'3}$-F_6Leu and (3*R*)- or (3*S*)-4^3-F_3Val can be incorporated in model II without significant disturbance of the helical motif, but with different outcomes in the thermal stability: enhanced for 5^3,$5^{'3}$-F_6Leu, and decreased for (3*R*)- or (3*S*)-4^3-F_3Val.[173] It was argued that this destabilization is a result of a less optimal packing of the fluorinated side chains within the helical core, the reduced helix propensity and the overall lower hydrophobicity (except for TfeGly[149], **Figure 2.13**), when compared with the canonical analogues. Interestingly, DfpGly greatly depended on the substituted position: with a destabilizing effect when incorporated at position ***a*** on model I,[168] and with a stabilizing effect when incorporated at position ***a*** on model II[170]. When incorporated at position ***d*** no clear relationship was observed.[142]

To summarize, the effect of substitution of hydrophobic canonical amino acids with their fluorinated counterparts cannot be predicted and its determined by combination of hydrophobicity, number of substitutions, fluorine content as well as the peptidic environment.

2.3.4. Incorporation of FAA into fiber forming coiled-coil systems

The fluorination effect on coiled-coil systems capable of forming high-ordered aggregates has been seldom explored. To date, the only study was reported.

The Montclare group reported on the incorporation of racemic 5^3-F_3Leu into fiber forming coiled-coils, and its impact against divalent metal ions and the ability of binding to curcumin (**Figure 2.14**).[174] Two canonical peptide sequences Q[175] and C and their fluorinated analogues (Q+TFL and C+TFL) were expressed using Leu auxotrophic *Escherichia coli* strain cells. A histidine tag was coupled to the *N*-terminus, making the peptides responsive to Ni(II) and Zn(II) metal ions. Incorporation of FAAs had a favourable impact on Q+TFL and C+TFL with

increasing of helicity, thermal stability and the ability of assembly into fibers. At pH 8.0, both Q+TFL and C+TFL formed protofibrils with average diameter of 3.6 ± 0.3 nm, that further assembled into larger microscale aggregates with dimensions ranging from 40 nm to 2.0 µm. Under the same conditions, the non-fluorinated peptides did not form fibers. Upon Zn(II) addition, both fluorinated peptides showed increased thermal stability. Moreover, for C+TFL the morphology of the aggregates changed from fibers to sheet-like structures. Interestingly, with the addition of Zn(II) the non-fluorinated peptides C and Q were also aggregated into fibers with sizes ranging from 40 to 569 nm. Addition of Ni(II) had a contrast behaviour: the helical conformation was disrupted for all peptides and only amorphous structures were formed. Furthermore, the addition of the two metal ions influenced the ability of the peptides to bind to curcumin: in the presence of Zn(II), all peptides showed binding to curcumin, with improved binding for the fluorinated peptides; in the presence of Ni(II), no binding occurred. The enhanced binding in the presence of Zn(II) was attributed to the increased helical content and maintenance of the hydrophobic core.

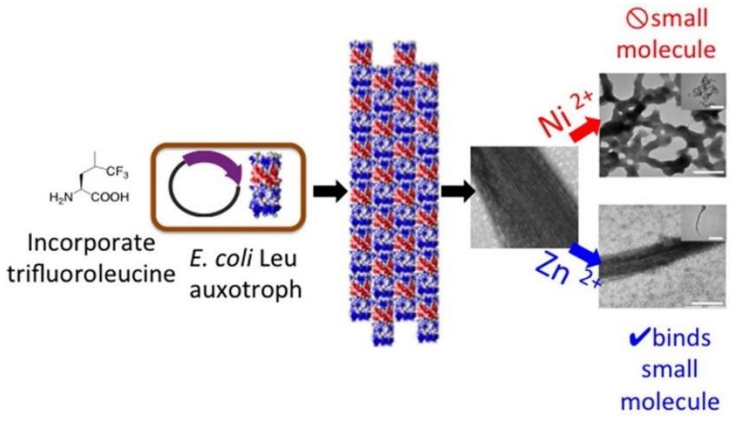

Figure 2.14. Incorporation of racemic 5^3-F_3Leu into fiber forming coiled-coils. Introduction of fluorinated leucine variants resulted in the formation of high aspect ratio fibers. Increased thermal stability of the fluorinated variants, fiber formation for the canonical variants and ability to bind to curcumin was observed only upon Zn(II) addition. (Reprinted with permission from More *et al*.[174]. Copyright © 2015 American Chemical Society).

The same group also reported on the modulation of the properties of soft materials by introduction of a monofluorinated variant of the canonical aromatic phenylalanine (*p*-fluorophenylalanine) into two self-assembly domains (elastine and a coiled-coil region of cartilage matrix proteins). This study showed that fluorination affects the

folding motif, the melting temperature, and the mechanical properties of the aggregates.[176]

2.3.5. ^{19}F Magnetic Resonance Imaging (MRI)

For decades, ^{1}H magnetic resonance imaging (MRI) has been used as a routine diagnostic tool in medicine. While providing high anatomical resolution, the abundance of background signal from endogenous ^{1}H results in low contrast, with the use of contrast agents is often required.[177] In this context, ^{19}F MRI has emerged as promising non-invasive approach to be used as a supplement to ^{1}H MRI.[119] Fluorinated tracers offer several advantages: (1) absence of background signal due to the negligible amount of fluorine in the human body; (2) the large NMR shift range; (3) the similar gyromagnetic ratios between ^{19}F (40.1 MHz T^{-1}) and ^{1}H (42.6 MHz T^{-1}); (4) the 100 % natural abundance of ^{19}F and (5) and ^{19}F sensitivity (83 % of the ^{1}H abundance).[118,119,178,179] However, fluorinated tracers are limited by their long relaxation times that can lead to exceedingly long scanning times.[179]

In literature there are some examples of fluorinated probes that can potentially be used in clinical ^{19}F MRI. Higuchi *et al*. synthesized a fluorinated Congo red derivative as fluorine source for the *in vivo* ^{19}F MRI and ^{1}H MRI detection of amyloid plaques of Alzheimer's diseased mice.[180] Oishi *et al*. described the copolymerization of pH-sensitive PEGylated nanogels with 2,2,2-trifluoroethyl methacrylate as ^{19}F source that was shown to regulate ^{19}F MR signal in response to acidic pH tumour environments.[181] Other examples include the use of perfluoropolyethers (PFPE) for the *in vivo* cell tracking[182,183] and fluorinated nanoparticles for imaging of brain inflammation[184,185].

In contrast, examples of peptides containing fluorinated amino acids as MRI tracers are rare. Kirberger *et al*. has recently developed a series of fluorinated polypeptides with high conformational disorder for ^{19}F MRI.[186] A library of different length peptides consisting of alternating *N*-ε-trifluoroacetylated lysine (TFA-Lys) and lysine residues was synthesized and studied by means of CD, ^{19}F NMR and ^{19}F MRI. When in aqueous environment, the peptides showed an unordered conformation and degenerated ^{19}F NMR resonances, whereas when dissolved in methanol, the peptides revealed an α-helical conformation and resolved ^{19}F resonances. With

these results the authors suggest a different spatial arrangement of the fluorinated side chains within the peptide accordingly to the solvent. As proof-of-concept, a peptide carrying 10 TFA-Lys and 10 lysine residues was conjugated to bovine serum albumin (BSA), therefore creating a ^{19}F MRI tag for large protein constructs. ^{19}F NMR results revealed maintenance of conformational dynamics of the fluorine bearing amino acids, reminiscing the disordered free peptides.

Other examples include a *N*-ε-(trifluoromethoxy)-poly-L-lysine labelled with fluorescein isothiocyanate for bone and cartilage cells tracking,[187] and a system comprised of a fluorinated protease substrate peptide (DEVD(trifluoromethoxy)) and a DOTA ligand complexed with Gd^{3+} for the detection of enzymatic activity[188,189].

3. Motivation and Aim

To successfully build well-defined supramolecular structures that can undergo morphology transition upon external stimuli, a thorough rational design, characterization and understanding of the underlying forces driving the assembly is essential. In this context, the easy of synthesis, chemical diversity, modularity, and defined sequence-to-structure rules makes coiled-coils a promising scaffold for the development of materials for drug delivery, biomimicking systems, and tissue engineering. Despite the recent advancements, one main challenge is the development of simple peptide sequences that can translate into defined high-order architectures. In this context, the goal of this work is to exploit coiled-coils for the formation of stimuli-triggered supramolecular assemblies. This thesis is divided into five sub-sections:

- In Part 1 (Section 4.1) a peptide scaffold capable of self-assembly into completely distinct supramolecular structures depending upon the solution pH is introduced.
- In Part 2 (Section 4.2) the influence of single mutations at the *N*-terminus on the original peptide sequence is explored. These experiments are performed to examine the effect of charge and hydrophobicity at the *N*-terminus on peptide's stability and ability to assemble.
- In Part 3 (Section 4.3) the effect of introduction of fluorinated amino acids of the helical core is analysed. This use of fluorinated variants of canonical amino acids is a common approach for modulating peptides properties. Here, the goal is to comprehend if it has a great influence within a supramolecular context.
- In Part 4 (Section 4.4) different content of acidic and basic residues are introduced in the parental sequence. With these alterations, the goal is to study the overall net charge of the peptides on the secondary conformation and thermal stability.
- In Part 5 (Section 4.5) selected scaffolds are studied for possible application in biomedical and catalysis research areas.

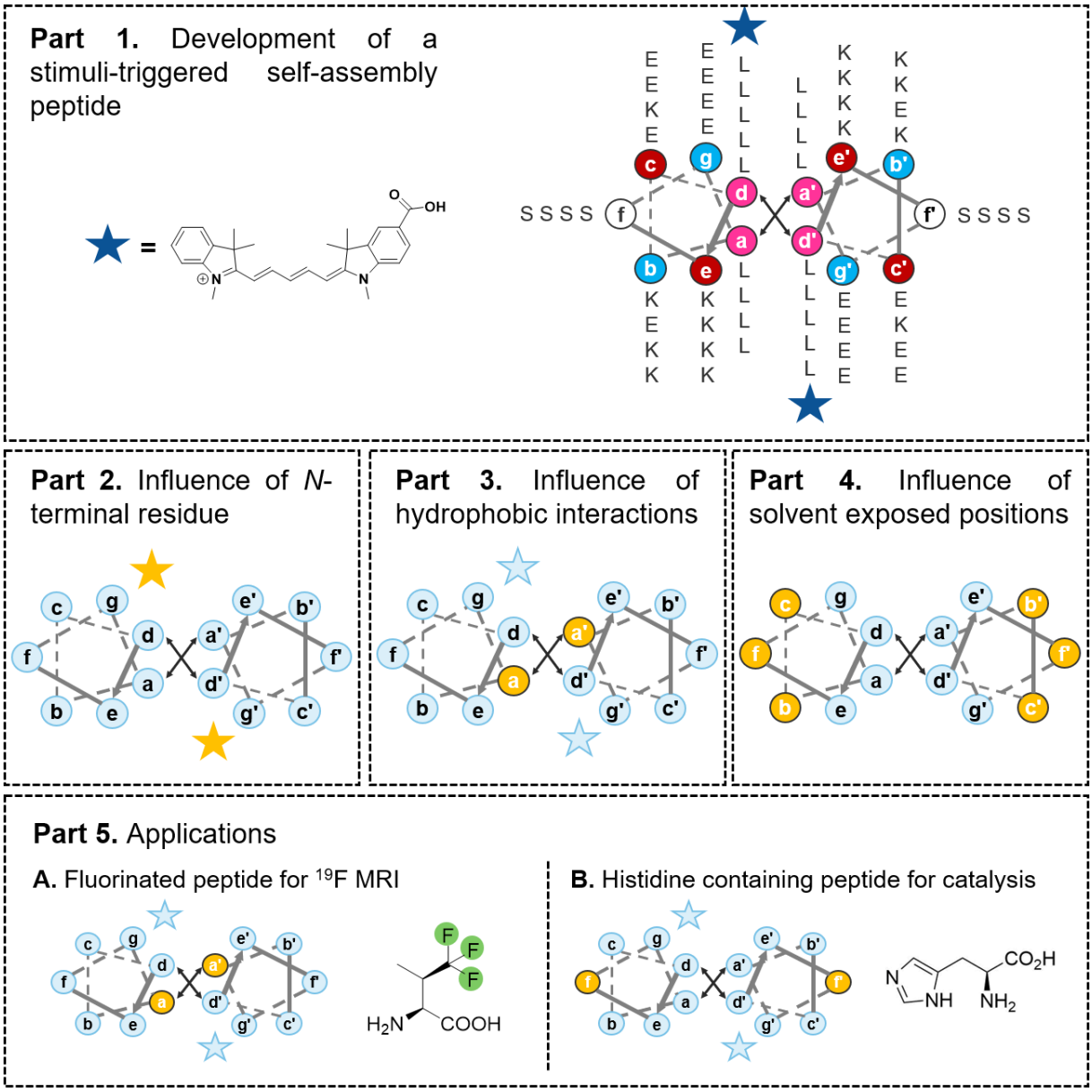

Figure 3.1. Concept to be explored in this thesis. The development of a helical self-assembly peptide sensitive to external stimuli, three approaches to study peptide folding, stability and aggregation, and studies for possible applications.

4. Results and discussion

4.1. Development of a pH-sensitive self-assembly coiled-coil scaffold

To construct a stimuli-responsive peptide, a *de novo* peptide (RF01) was designed based on the rules for the formation of α-helical coiled-coils.[38] This peptide was based on previously fiber-forming peptides reported by the Koksch group (**Section 2.2.3**).[97,190] The simplicity of the scaffold can be observed in **Figure 4.1**. This 29-mer peptide is comprised of only four different amino acids that are regularly distributed in a *hpphppp* pattern, between hydrophobic (*h*) and polar (*p*) residues. Leucine residues were placed in positions ***a*** and ***d*** in order to promote helical assembly and the formation of a hydrophobic core.[38] The core-flanking positions ***e*** and ***g*** were occupied with lysine and glutamic acid, respectively. These charged amino acids are able to form interhelical electrostatic interactions and further stabilize the assemblies. Lysine and glutamic acid were placed in positions ***b*** and ***c*** in a complementary and alternating manner to form intra- and interhelical electrostatic interactions and to promote multi-lateral fiber assembly.[71,97] Position ***f*** was made serine, a small polar amino acid, for solubility purposes.

(A)

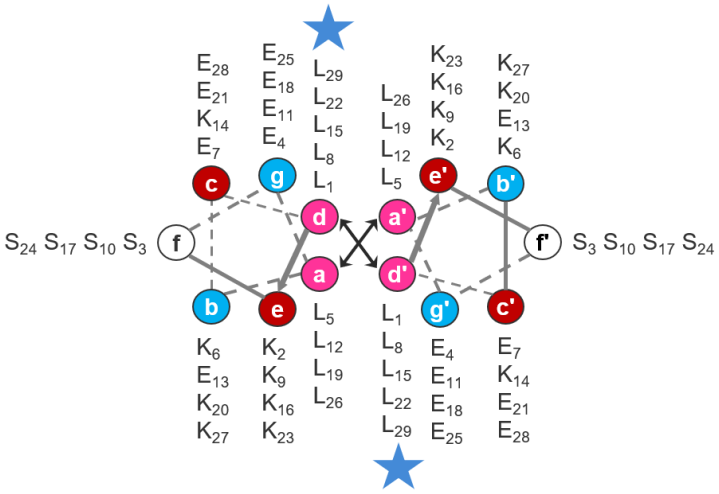

(B)

	N-terminus	*defg*	*abcdefg*	*abcdefg*	*abcdefg*	*abcd*
RF01	Cy5	LKSE	LKELKSE	LEKLKSE	LKELKSE	LKEL

Figure 4.1. Design and sequence of RF01. (**A**) Helical wheel representation of RF01. The yellow star represents the position where the chromophore was introduced. (**B**) Linear sequence of RF01. The *C*-terminus is free.

Two key design features were the introduction of a cationic cyanine dye (Cy5) to the *N*-terminal, and the high content of opposite charged amino acids. It should be highlighted that this specific dye was chosen with the initial purpose of tracking of RF01 into T-cells. Cyanines are a family of dyes used in several applications, for example, in biomolecules labelling, imaging, inhibition of cell growth, laser technology, and semiconducting materials.[191–194] Their general chemical structure is characterized by two nitrogen-bearing heterocyclic components connected by a polymethine bridge made up of an odd number of carbons; their nomenclature follows the number of carbon atoms in the bridge, Cy3 has 3 carbons, Cy5 has 5 carbons and Cy7 has 7 carbons. [195] As shown in **Figure 4.2 A**, the Cy5 used in this study consists of two indole cycles connected by a pentamethine bridge, and a carboxylic moiety for an easy covalent attachment to the peptide sequence. These family of dyes are known to have a high extinction coefficient and fluorescence quantum yield.[192] In addition, they are able to self-assemble through π-π stacking of the planar aromatic systems into two possible stacking geometries, depending if the chromophores stack face-to-face (H aggregates) or edge-to-edge (J aggregates) (**Figure 4.2 B**).[196] H and J aggregation results in different optical properties. That is, in comparison with the unaggregated form, H aggregates are characterized by a maximum in absorbance shifted towards lower wavelengths and quenching of fluorescence; in contrast, J aggregates are highly fluorescent samples with a maximum in absorbance shifted to longer wavelengths. Therefore, the introduction of the Cy5-like can theoretically provide an additional order and direction to the expected supramolecular structures.[197]

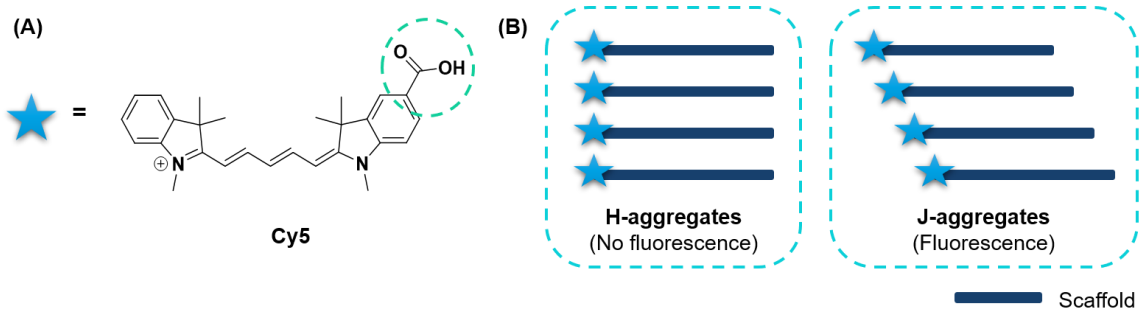

Figure 4.2. Chemical structure of Cy5 and possible aggregation modes for the dye-peptide conjugates. (A) Chemical structure of the Cy5 derivative used in this study, represented here with the free carboxylic group**. (B)** H and J aggregates stacking geometries.

The eight lysine and eight glutamic acid residues, distributed over the positions ***b***, ***c***, ***e*** and ***g***, makes RF01 highly responsive towards pH. By using an iterative Grimsley algorithm in the R program package pIR developed by Audain *et al*.[198], the theoretical isoelectric point (pI) of RF01 sequence without dye was calculated as 6.41. However, assuming that protonation of Cy5 only occurs under strong acidic pH – bellow the pH used in this study – the value can be approximated to 5.05, corresponding to RF01 with an acetylated (capped) *N*-terminus. Therefore, the amount of protonated glutamate residues is expected to increase with the addition of acid. Conversely, the amount of deprotonated lysine residues is expected to increase with the addition of base. Furthermore, considering that the estimated pK_a values in a peptidic environment between 4.25[199] and 4.4[200] for glutamic acid and 10.4[199] for lysine, it is reasonable to assume that under acidic conditions (pH = 3.4) RF01 has an overall positive net-charge, and under basic conditions (pH = 11) RF01 has an overall of negative net-charge.

Behaviour in solution

RF01 was readily dissolved under basic conditions (pH 11) while at either pH 3.4 or pH 7.4 presence of particulates was macroscopically evident. For pH 7.4, large aggregates were initially formed, but after thermal denaturation and solution cooling, a fine precipitate was observed. For pH 3.4, a fine precipitate was observed immediately upon solution preparation (no changes were apparent after thermal treatment). In either case, placement of the vials in an ultrasonic bath for 1 h was unsuccessful to disassemble the large aggregates. With time, the precipitate sedimented at the bottom of the vial (**Figure 4.3**).

The behaviour of RF01 in the different pH environments was analysed using negative staining transmission electron microscopy (TEM) and cryo-TEM. RF01 formed defined supramolecular structures when buffered at pH 3.4 and 7.4. Only amorphous assemblies were observed for pH 11.

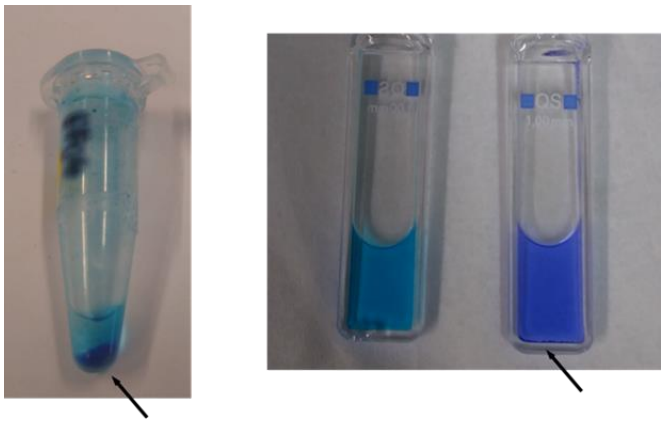

Figure 4.3. Macroscopic evidence of peptide aggregation. From left to right: RF01 at pH 7.4, pH 11 and pH 3.4. For pH 7.4, the fine precipitate was formed after the thermal denaturation experiments. The blue colour originates from of the cyanine dye.

Morphology of the supramolecular structures

cryo-TEM images of RF01 buffered at pH 3.4 revealed the formation of highly ordered membrane-like structures (**Figure 4.4**). These structures spontaneously form after the addition of buffer. These large aspect ratio structures have diameters exceeding 100 nm and several micrometre lengths. Higher magnification revealed a seemingly regular hexagonal pattern with defined periodic spacing (**Figure 4.4 B**).

Cryo-electron tomography was used to obtain 3D reconstructions of the membranes in a frozen-hydrated near-native state. With this technique, micrographs with incrementally tilting a sample around an axis perpendicularly to the electron beam produces are collected and combined to create a projection image.[201]

Figure 4.5 shows the cryo-tomography reconstruction of the fine structural detail of the membranes. An evident well-defined and periodic electronic density can be observed.

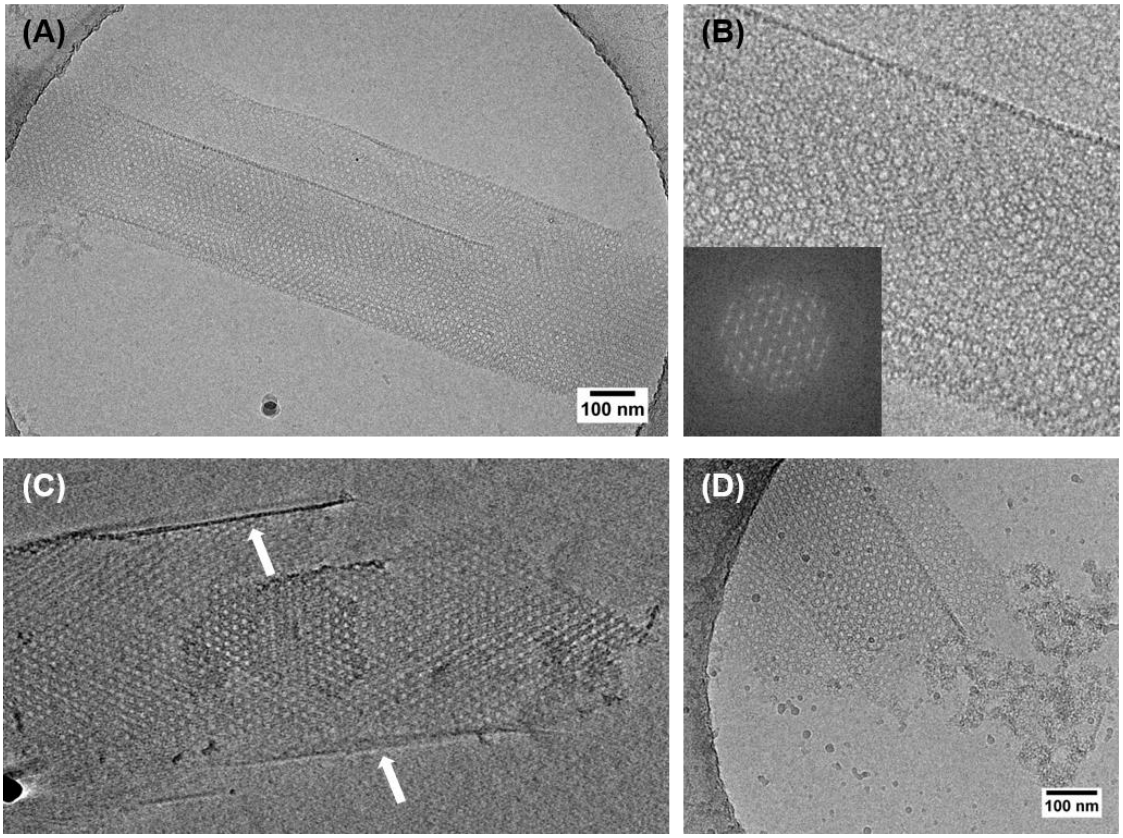

Figure 4.4. **Representative cryo-TEM micrographs of the structures formed at pH 3.4.** (**A**) Cryo-TEM of the membrane; (**B**) zoom of A, revealing the regular hexagonal pattern and FFT analysis (inset) revealing the periodic lattice of the membranes; (**C**) representative image showing out-of-plane regions of the membrane; (**D**) edges revealing disintegration of the membrane. Peptide concentration: 0.1 mM.

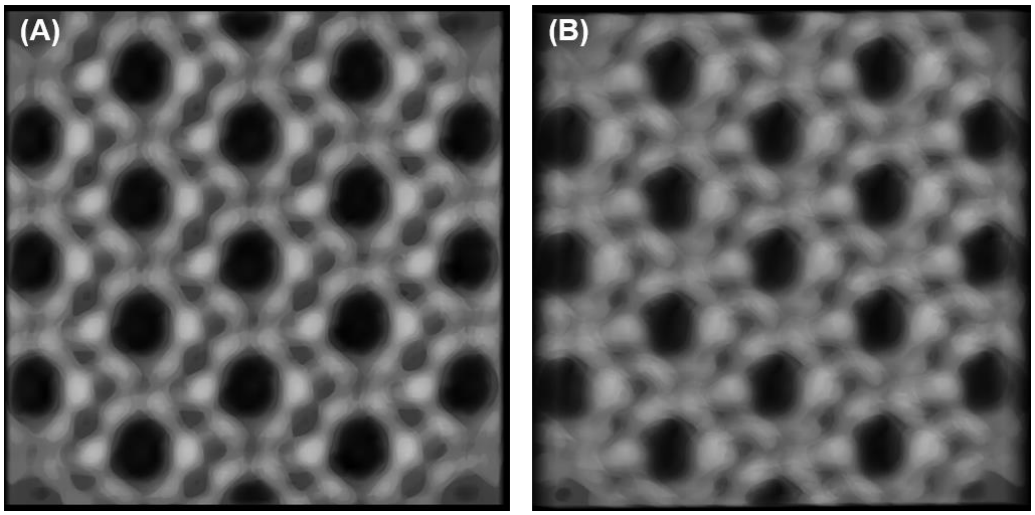

Figure 4.5. cryo-electron tomography reconstruction of the membranes. (**A**) top-view, (**B**) tilted view.

In contrast, when buffered at neutral pH conditions and after thermal annealing, RF01 assembles into long, unbranched rods (**Figure 4.6**). When not subjected to thermal treatment only ill-defined assemblies were observed (**Figure 4.6 A**). The rods exhibit a heterogeneous size distribution, however a consistency of diameters exceeding 100 nm and several micrometres in length was observed. Upon magnification, a periodic pattern of high and low electron density (from now on referred as striations) were clearly observed along the rods (**Figure 4.6 C-F**). Similar structures were already reported by the Woolfson group.[71,73] However, contrary to Woolfson's reports were the striation pattern was only observed perpendicularly to the longitudinal axis (as for example in **Figure 4.6 D-F**), here a parallel pattern regarding to the long rod axis was also present (**Figure 4.6 C**).

cryo-TEM confirms that the striation pattern is native to the structures and not a consequence of the staining solution used in negative-staining TEM (**Figure 4.6 F**). Further analysis of the cryo-TEM were performed by cryo-electron tomography (**Figure 4.7**). This revealed cross-sections with periodic distribution of electron density, i.e., the rods are not solid cylinders. Fast-Fourier transform (FFT) of the striations revealed a consistency of 4.4 nm in all directions (**Figure 4.7**) except one that revealed a 5.08 nm spacing (**Figure 4.7 C** red trace). Interestingly, while the 4.4 nm value matches the expected for a fully folded 30-mer coiled-coil (30 x 0.148 nm = 4.3 nm, with 0.148 nm as the estimated pitch increase per residue in an α-helix)[72], the 5.08 nm spacing matches the expected for RF01 considering the presence of the larger Cy5 moiety. A similar observation was previously reported by Sharp *et al*.[73] The authors suggest that the solid fibers (cryo-tomography showed an uniform internal electron density) were formed by α-helical coiled-coils aligned along the long fiber axis (see **Section 2.2.2**). However, for the rods formed by RF01 the same argument cannot explain the same distance observed for all projection views, the existence of both perpendicular and parallel striations and the 5.08 nm observed in the top-view projection. Furthermore, another evidence supporting a different arrangement of RF01 within the rods is the absence of electron density between the striations, meaning that is not likely that RF01 strands are arranged parallel to the rod long axis.

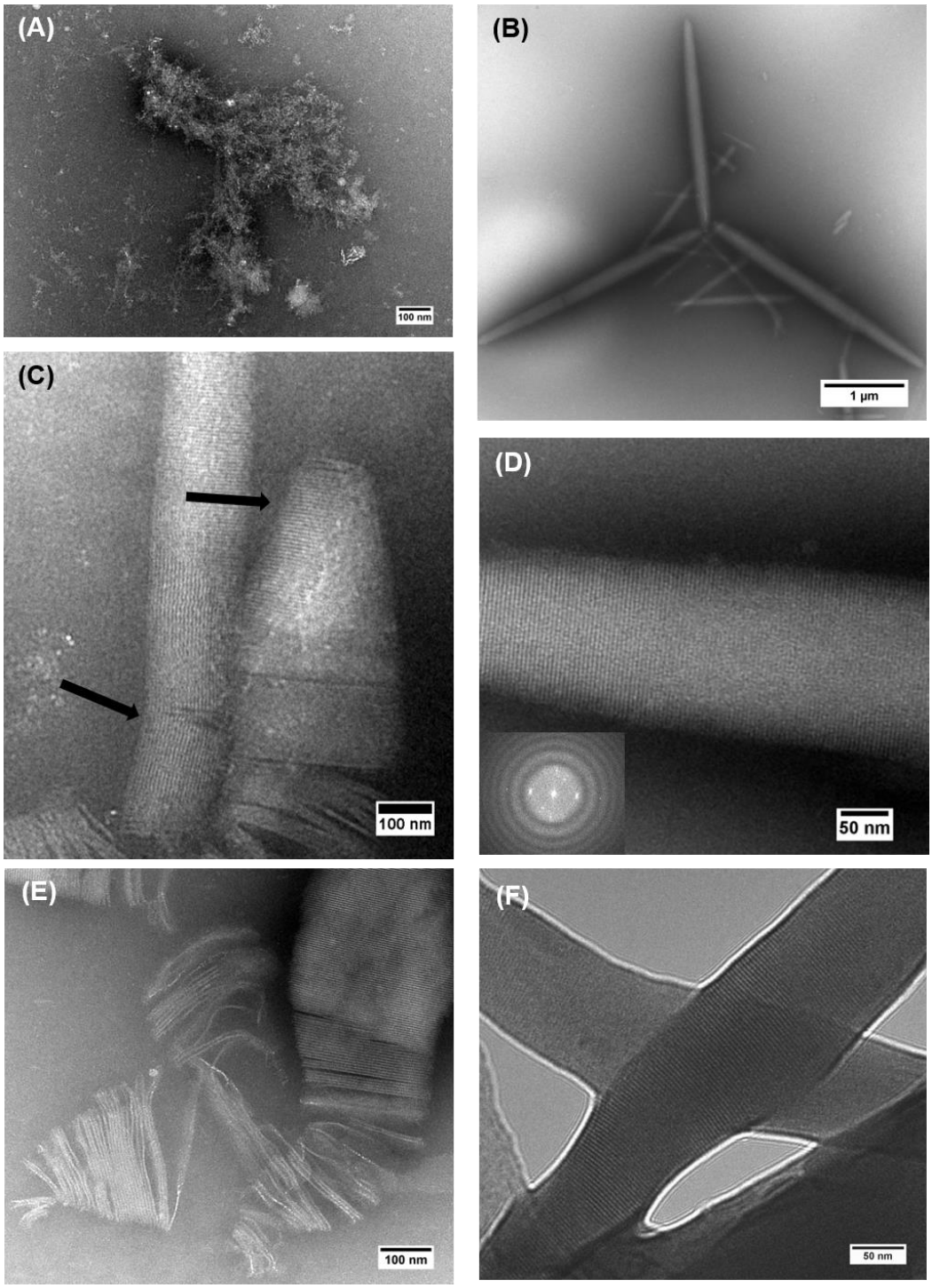

Figure 4.6. Representative TEM micrographs of the structures formed at pH 7.4. (**A**) formation of amorphous structures without thermal annealing; (**B**) heterogeneous distribution of dimensions; (**C**) vertical and horizontal striation pattern; (**D**) higher-magnification of the striations with FFT analysis (inset) revealing the periodicity of the rods; (**E**) threads incorporation into the rods; (**F**) cryo-TEM. Peptide concentration: 0.1 – 0.2 mM.

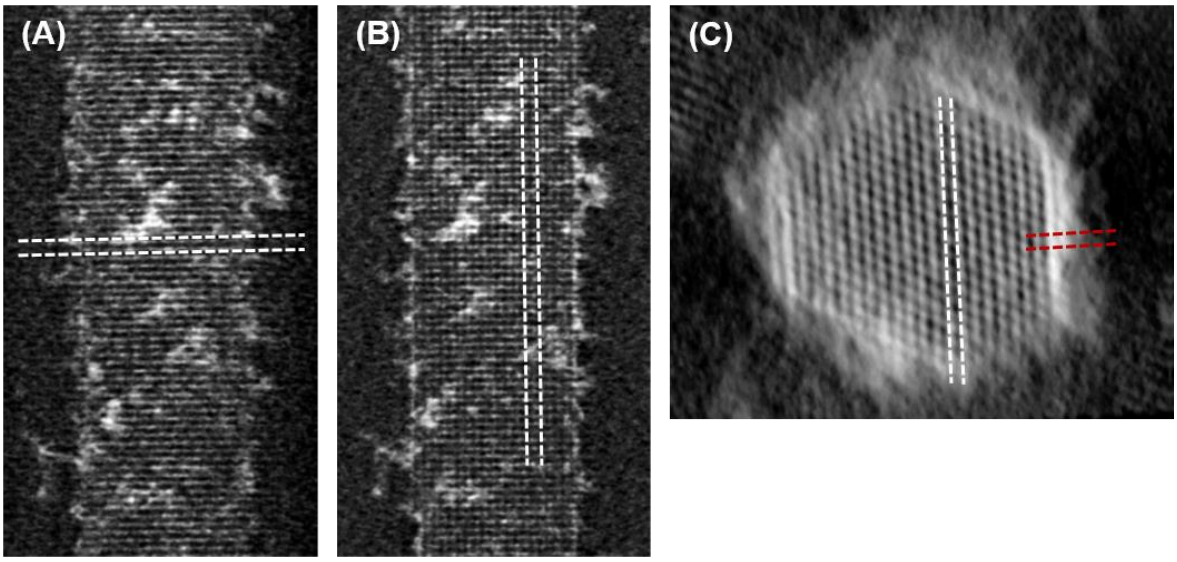

Figure 4.7. Reconstruction of the rods. (**A**) side view 90 °; (**B**) side view 90 ° and 20 ° rotated; (**C**) top view 20 ° rotated. The white dashed trace represents the 4.4 nm distance between striations. The red dashed trace represents a 5.08 nm distance.

In contrast to the previous conditions, cryo-TEM of RF01 buffered at pH 11 only revealed ill-defined aggregates (**Figure 4.8**). However, such structures were also observed for either pH 3.4 and 7.4 and are likely helical oligomers.

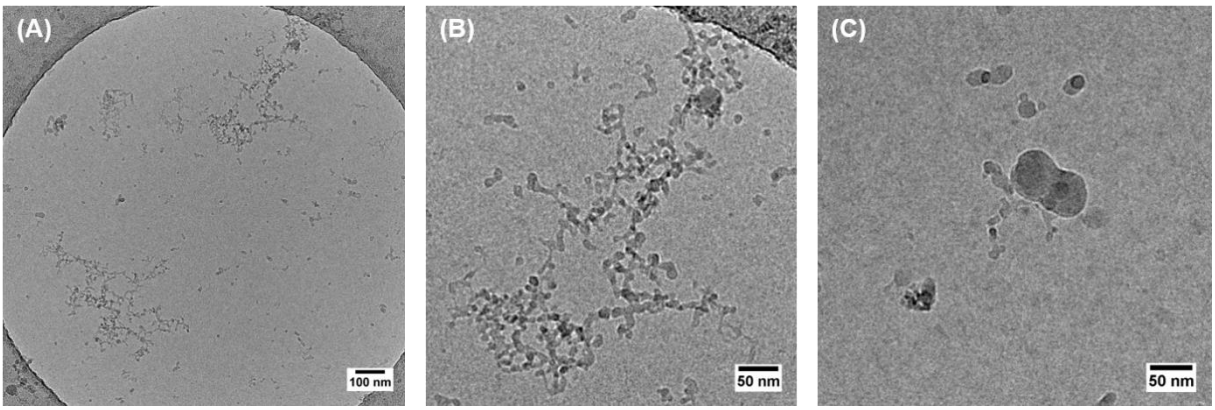

Figure 4.8. Representative cryo-TEM micrographs of the structures formed at pH 11. (**A**) bundles of ill-defined aggregates; (**B**, **C**) zoom of A revealing apparent round shape of the nanoscale assemblies. Peptide concentration: 0.1 mM.

Conformation and stability in solution

Figure 4.9 A, B shows the far-UV CD spectra for RF01 before and after thermal denaturation experiments at pH 3.4 and 7.4. As judged by the double minima around 208 and 222 nm and the maximum around 195 nm, the α-helical conformation is independent on the pH. Both nascent solutions (before the temperature dependent experiments) show very low CD intensity. Because the formation of particulates is macroscopically evident, the low CD intensity is attributed to a lower concentration of peptide available in solution. This observation is in agreement as previously reported by Schöne *et al.*[202] and Gribbon *et al*[65]. Upon a first thermal denaturation, the increase on ellipticity reflects the disruption of the large particulates and the increase of peptide in solution. Further heating and cooling cycles do not result in a significant change of CD intensity. Interestingly, in benign medium, the CD spectrum is distorted regarding to the typical α-helical. That is, the large attenuation of the band around 208 nm and a shifting of the CD spectra towards higher wavelengths, confirms the formation of insoluble fibrous structures.[60,203] The occurrence of aggregation and distortion of the CD spectrum at pH 7.4 makes the determination of the helical content inaccurate. However, a qualitative comparison indicates that under acidic condition the peptide is more helical.

Thermal denaturation experiments at pH 3.4 and 7.4 show that RF01 unfolds with a progressive loss of helical conformation as judging from the attenuation of intensity at 222 nm (**Figure 4.9 C, D**). However, negative ellipticity values suggests residual helical folding to temperatures up to 95 °C. The apparent melting temperature (T_M) could only be determined for neutral pH conditions. Interestingly, the following behaviour was observed: thermal denaturation of a nascent solution shows a T_M of 47 ± 1 °C; following melting experiments resulted in a T_M of 73 °C. That is, a substantial gain in stability is achieved with formation of the compact rod structures. At pH 3.4, RF01 shows no defined thermal transition, i.e., the peptide is highly stable up to 95 °C. The full spectra as function of temperature shows increase of the band at 203 nm with temperature, indicative of an unordered conformation. However, the shoulder at 222 nm and absence of an isodichroic point around 203 nm, corroborates that a mixture of helical and random conformation exists at high temperatures (**Figure 4.9 E, F**).

As peptide concentration and extinction coefficient does not significantly varies in these temperature dependent studies, differences in light scattering can be attributed to changes in the particle size and/ or to the refractive index.[204] Analysis of the dynode response in function of temperature for RF01 at pH 7.4 shows a sharp increase of approximately 20 V and isodichroic point of 78 and 75 °C with the first and second thermal annealing curves, respectively (**Figure 4.10**). These data suggest that formation of large aggregates occurs immediately upon cooling the solution below 78 and 75 °C, respectively.

The increased thermal stability of the RF01 under acidic conditions is likely a consequence of protonation of the glutamic acid. This reduces unfavourable intrahelical repulsive *i, i + 3* and *i, i + 4* interactions between glutamic acids along each helix of the coiled-coil. Although reasonable to assume that interhelical salt-bridges contribute to coiled-coil stability,[33,205,206] the observation that stability increases under acidic conditions is consistent with previous reported synthetic coiled-coils and natural constructs.[52,207–212] In addition, Kohn *et al.* reported on the increased stability of coiled-coils by increased hydrophobicity upon protonation of glutamic acid residues at the flanking positions ***e*** and ***g***.[213]

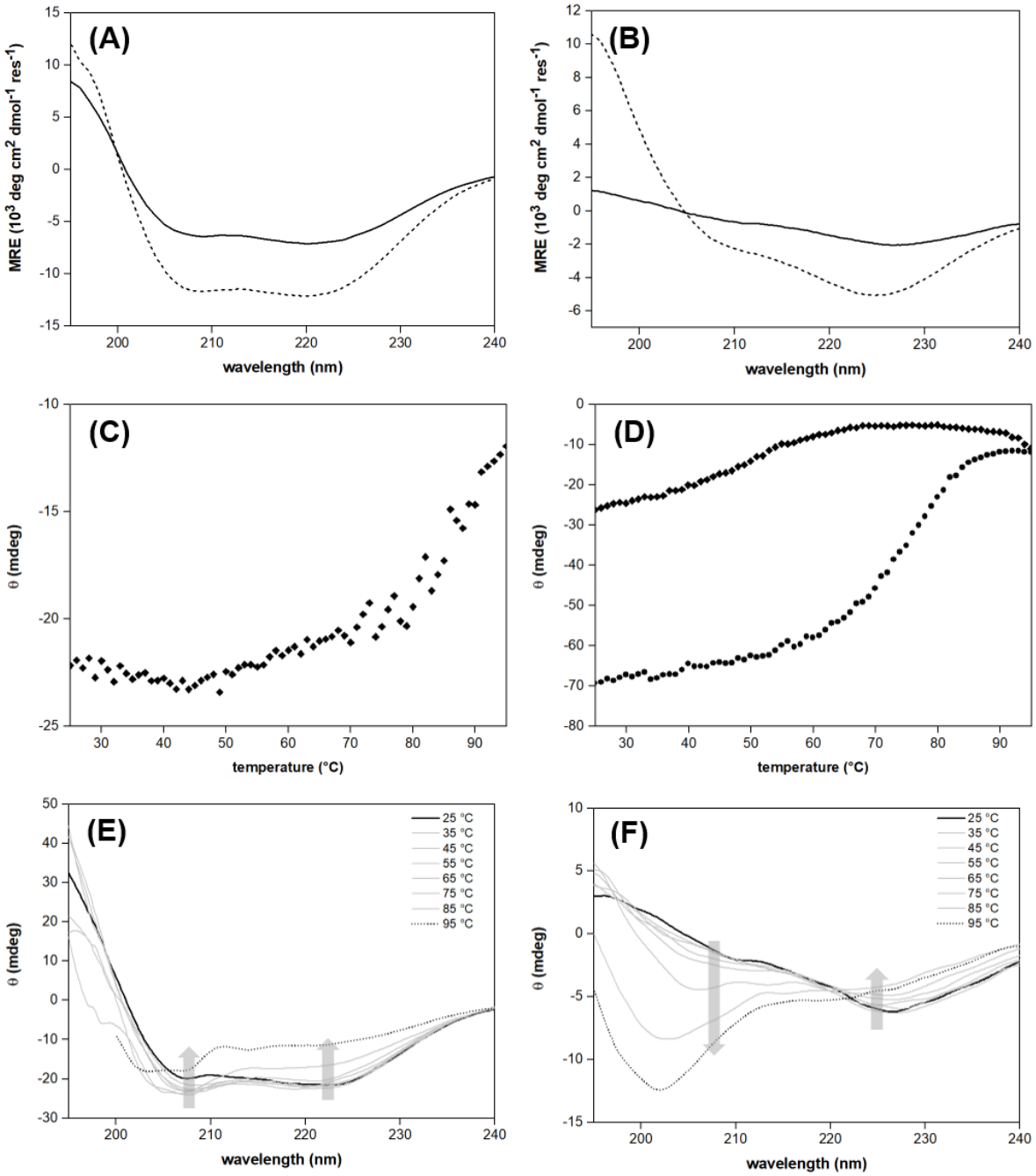

Figure 4.9. CD spectra of RF01 at pH 3.4 and 7.4. (**A**) CD spectra at 25 °C for RF01 at pH 3.4, 0.1 mM peptide; (**B**) CD spectra at 25 °C for RF01 at pH 7.4, 0.1 mM; (**C**) variation of ellipticity at 222 nm as function of temperature at pH 3.4; (**D**) variation of ellipticity at 222 nm as function of temperature at pH 7.4 for first denaturation (diamonds) and second denaturation (circles); (**E**) full spectra as function of temperature from 20 to 95 °C (at 3 °C min^{-1}) at pH 3.4; (**F**) full spectra as function of temperature from 20 to 95 °C (at 3 °C min^{-1}) at pH 7.4 CD after solution preparation (solid trace) and after the thermal denaturation experiment (dashed trace). Heating: 25 to 95 °C (at 3 °C min^{-1}).

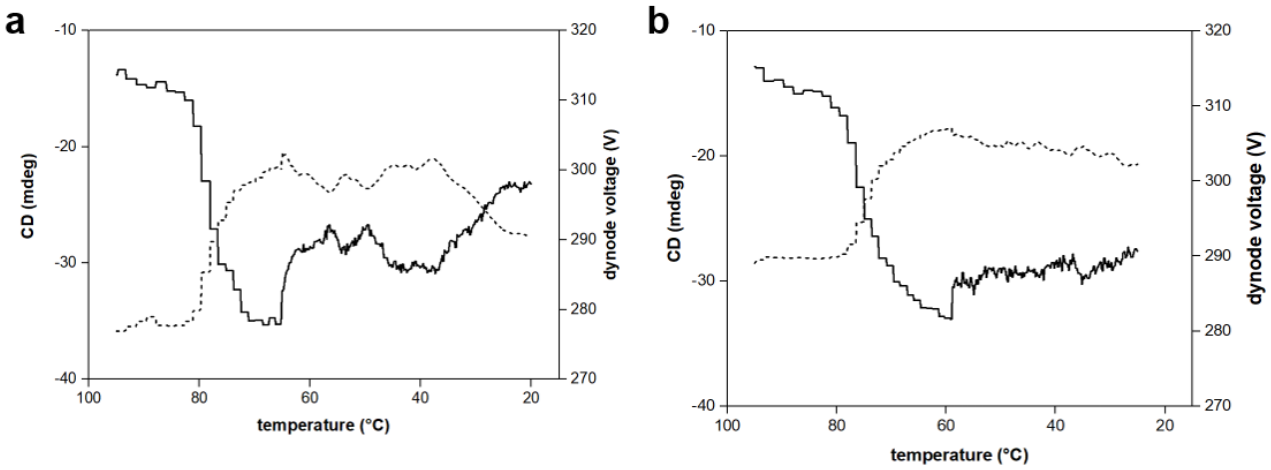

Figure 4.10. Thermal annealing of RF01 at pH 7.4. CD spectrum (right axis and solid trace) and dynode spectra (left axis and dotted trace) as function of temperature for (**a**) first thermal annealing and (**b**) second thermal annealing (24 h after the first thermal annealing experiment). Peptide concentration: 0.2 mM at pH 7.4 cooling rate of 95 to 20 °C at 3 °C min^{-1}.

The spatial arrangement of the peptide-dye conjugates within the different supramolecular morphologies have a strong influence in the properties of the cyanine dye. To study the impact of the formation of the membranes and rods, the higher wavelength region of the visible-spectrum was analysed by CD, UV-vis absorbance and fluorescence. **Figure 4.11 A** shows the CD spectra of RF01 buffered at pH 7.4. Here, strong absorption with peaks at 656.5 nm, 634.5 nm and a shoulder at 622.5 nm was observed after rods formation, suggesting chirality transference from the peptide backbone. No such behaviour occurred for RF01 solution at pH 3.4. **Figure 4.11 B** and **C** shows the UV-absorbance and fluorescence spectra for RF01 under pH 3.4 and 7.4, and for a methanolic solution of Cy5 without peptide. Under both pH conditions, the hypsochromic shift of the absorption maxima and the quenching of fluorescence indicates that the dyes form H-aggregates. That is, the dyes are face-to-face stacked within the membranes and rods.

The complex UV-absorbance spectra observed for RF01 at pH 3.4, with three main bands at 554, 603 and 650 nm, suggests the formation of different kind of H aggregates (**Figure 4.11 B**, red trace). However, the origin and cause of such behaviour will not be discussed in this thesis

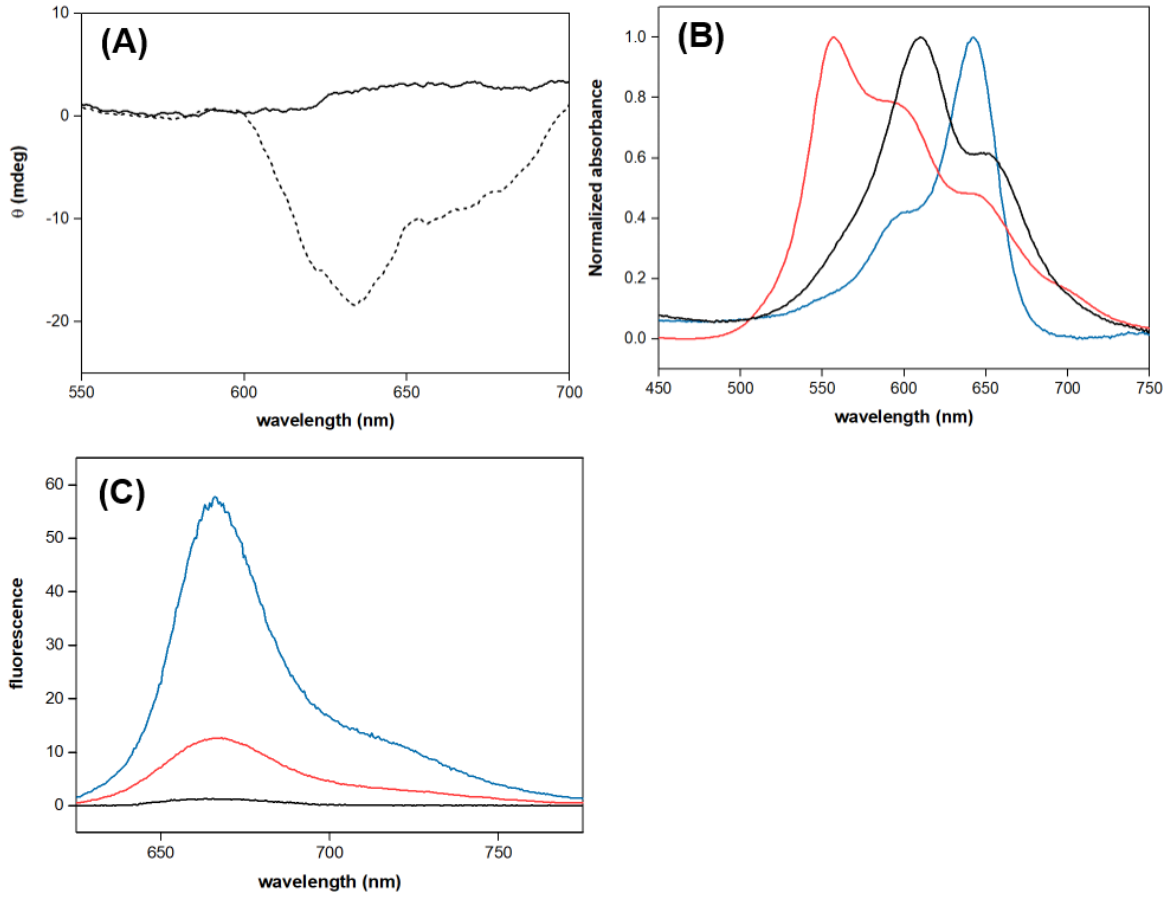

Figure 4.11. Higher wavelength spectroscopic studies of RF01 at pH 3.4 and 7.4. (**A**) Higher wavelength CD spectra for of a nascent solution (solid trace) and after the thermal denaturation experiment (dashed trace) buffered at pH 7.4; (**B**) normalized UV-absorbance spectra at pH 3.4, pH 7.4 and Cy5 monomer in methanol (two main absorption bands can be observed for Cy5 monomer: a main band at around 642 nm, corresponding to the monomer absorption band, and the second maximum at 602 nm, corresponding to a vibrational sub-band.[214,215]); (**C**) fluorescence spectra at pH 3.4, pH 7.4 and cy5 monomer in methanol. (**B,C**) pH 3.4 (red trace), pH 7.4 (black trace) and Cy5 monomer (blue trace)

As a control peptide, RF09 was synthesized lacking any dye or aromatic moiety at the terminus, i.e., with a free *N*-terminus. CD analysis shows maintenance of the helical motif with the double minima around 208 and 222 nm for all pH conditions (**Figure 4.12 A, B**). In contrast to RF01, RF09 shows a significant attenuation of the band at 222 nm and increase at around 208 nm. The ratio between ellipticity at 222 and 208 nm is occasionally used as an indicator of quaternary interaction. That is, $\theta_{222nm}/\theta_{208nm}$ values above 1.0 are usually observed for a canonical coiled-coil

conformation, whereas lower values usually indicate single α-helical interactions.[102,216] Therefore, RF09 is assumed to be in a single α-helical conformation. However, it should be noted that the origin and effect of peptide sequence on this ratio is not well defined.[217]

Thermal unfolding and annealing behaviour of RF09 at pH 7.4 was studied using the same conditions as for RF01 (**Figure 4.12 C, D**). This uncapped peptide shows cooperative thermal unfolding and refolding transitions. The second thermal denaturation experiment performed 24 h after the first experiment, results in a slight increase of the T_M (48.3 *vs* 51.8 °C, respectively). As expected, the dynode voltage for both thermal annealing experiments remains virtually unaltered as function of temperature (**Figure 4.12 E**).

As expected, no membranes or rod were observed by cryo-TEM. Under acidic conditions, RF09 self-assembled into long and flexible fibers made by the lateral association of thin fibrils (**Figure 4.13 A**), whereas under neutral conditions only ill-formed nanoaggregates were observed (**Figure 4.13 B**). These results indicate that the amino acid sequence had an intrinsic propensity to self-assemble under acidic conditions but Cy5 was crucial for the assembly into the high-order architectures.

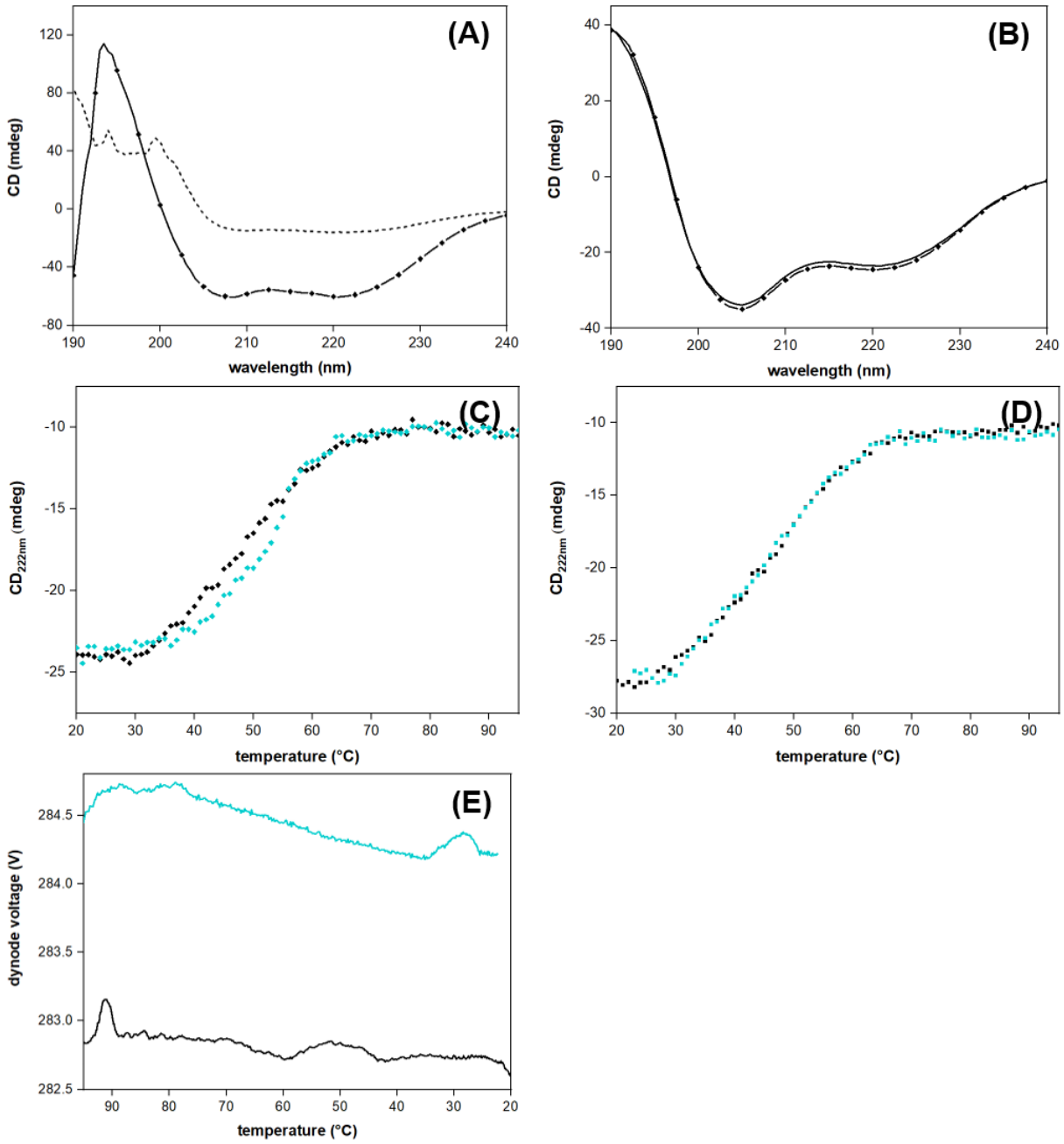

Figure 4.12. CD studies of RF09. (**A**) CD spectra at pH 3.4 (squared traced) and pH 11 (dashed trace); (**B**) CD spectra at pH 7.4 before (solid traced) and after (squared trace) thermal denaturation experiments; (**C**) first (black squares) and second thermal denaturation; (**D**) first (black squares) and second thermal annealing; (**E**) dynode spectra as function of temperature for first (black trace) and second (blue trace). Peptide concentration: 0.1 mM. Heating at rate of 20 to 95 °C at 3 °C min^{-1}, and cooling at rate of 95 to 20 °C at 3 °C min^{-1}.

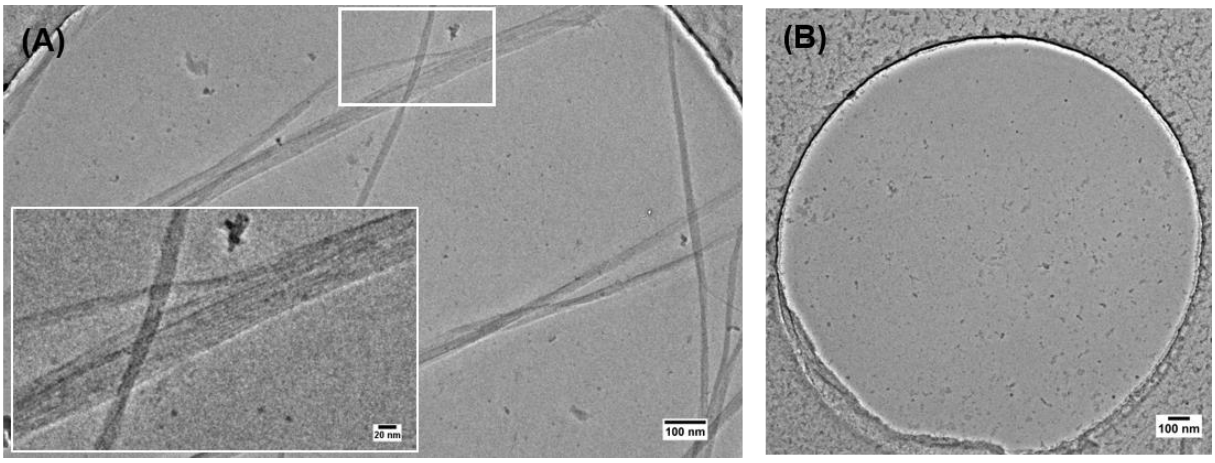

Figure 4.13. Representative cryo-TEM micrographs of RF09. (**A**) RF09 at pH 3.4 (inset: enlarged region); (**B**) RF09 at pH 7.4, 24 h after thermal denaturation experiments.

Molecular organization within the membranes and rods

Taking together, the data collected by spectroscopic and electron microscopy techniques, several observations can be made. The attachment of dye was crucial to form the rods and membranes, presumably with π-stacking between dyes being the driving force for assembly. Protonation of glutamic acid has a major effect in both peptide stability and ability to self-assemble. In addition, under pH 3.4 and pH 11, in the absence of attractive interactions between the side chains of lysine and glutamic, indicates that other type of interactions must compete favourably with the repulsive interactions for RF01 to assemble at pH 3.4.

To date, molecular modelling experiments are still being performed to elucidate the packing of RF01 within the membranes and rods.

A proposed arrangement of RF01 within the rods is represented on **Figure 4.14**. A key aspect for the proposed arrangement is the 5.08 nm spacing that is consistent to the expected length for RF01, and that it can be explained considering RF01 fully extended as depicted in **Figure 4.14**. However, the 4.4 nm spacing between the layers is still open to interpretation.

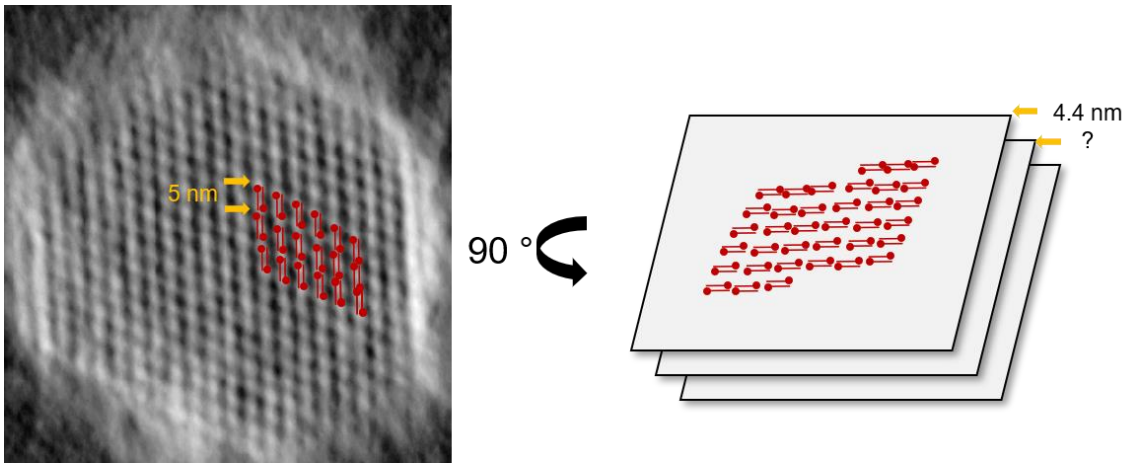

Figure 4.14. Proposed arrangement of RF01 within the rods. Left: top view, right: lateral view.

Despite of the lack of structure elucidation, it can be argued that the key player for the formation of rods is the hydrophobic effect. This is supported by the dependence of the strength of hydrophobic interactions on temperature. That is, high temperature values result in a wider distance between the peptide chains and therefore to a greater exposure of hydrophobic residues to the solvent.[85] Upon cooling, the rearrangement of the hydrophobic residues - mainly through stacking of the aromatic groups of cy5 - directs the tight packing and alignment of the peptides within the rods. In addition, salt bridges are stabilized by high temperatures, contributing to protein stability.[218] Hence, rod stability and assembly is further modulated by salt bridges between charged lysine and glutamic acid residues as well as intramolecular interactions such as backbone H-bonds. However, it cannot be discarded that formation of the rods might also occur without a thermal input but in a very slow fashion. It may be the case that the initially formed amorphous aggregates are not more stable than the rods, but that their formation is kinetically driven, i.e., their formation occurs faster.[219,220]

It is more difficult to interpret the data on the formation of the membranes. Extremes of pH should minimize aggregation because of repulsive intermolecular interactions. However, formation of membrane-like structures at pH 3.4 indicates that these repulsive interactions must be outnumbered by strongly favourable ones, namely cation-π interactions between the Cy5 electron rich aromatic system and the positively charged lysine side-chains, residual salt-bridges between lysine and

glutamic acid. In addition, the absence of unfavourable interactions from neutral glutamic acid might also factor for membranes formation.

In this project, a 29-mer peptide consisting of a regular distribution only four different residues conjugated to a large dye moiety was shown to undergo pH-sensitive ordered self-assembly. This simple peptide-dye scaffold revealed robust in that the different pH conditions did not result in significant conformation or thermal destabilization. Despite the lack of a complete elucidation of the arrangement of the peptides within the structures, it can be argued that the arrangement of the dyes in combination to favourable interactions with the peptide scaffold dictated the final morphology of the aggregates. This peptide has the potential to be used as model for fundamental protein research and applied for the fabrication of peptide hybrids by the introduction of functional organic and inorganic moieties.

4.2. Influence of the *N*-terminal on the stability and assembly

The unexpected results described in the previous section, led to further investigation on the impact of the dye. The goal of this project was to investigate whether the replacement of Cy5 with more readily accessible residues would result in similar high-order constructs. To this end, a series of *de novo* RF01 derivatives were designed and characterized. RF01's primary sequence was kept unaltered and only the Cy5 was substituted (**Table 4.1** and **Figure 4.15**). Since the sequence was unchanged, differences in peptide stability and assembly can be directly attributed to the residue covalently attached to the *N*-terminus.

Table 4.1. Residues attached to the *N*-terminus.

Peptide[a]	Moiety attached to the *N*-terminal
RF04	tryptophan
RF05	*N*-Fmoc-protected tryptophan
RF06	*N*-acetylated tryptophan
RF08	*N*-Fmoc

[a]Peptide sequence: **X**LKSELKELKSELEKLKSELKELKSELKEL, with **X** as the only variable.

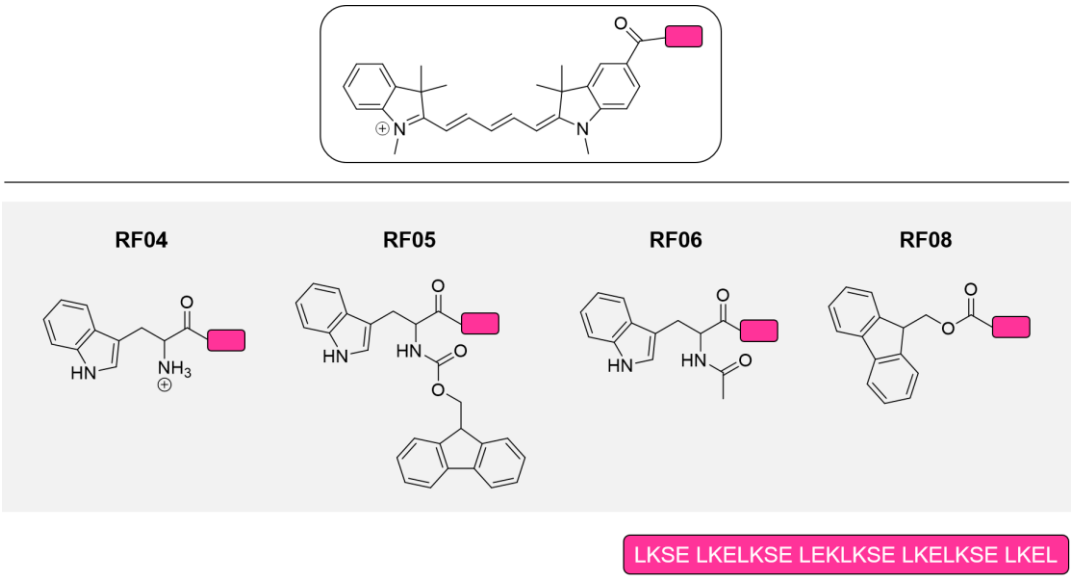

Figure 4.15. Chemical structures of residues attached to the *N*-terminus. Top: chemical structure of Cy5; bottom: chemical structures of free W (RF04), Fmoc-protected W (RF05), acetylated W (RF06) and Fmoc (RF08) attached to the *N*-terminus.

From the 20 proteinogenic amino acids, tryptophan (Trp or W) matches the closest with the nitrogen bearing heteroaromatic ring of cy5 dye. This natural occurring amino acid is commercially available and is widely used in peptide science, in particular in the field of antimicrobial peptides.[221] An important feature of tryptophan is the π-electron rich system on the indole side chain that gives a quadrupole moment.[221,222] In addition, the large planar aromatic moiety is capable of π-π stacking interactions and the indole NH moiety available to H-bonding.[221–224] Furthermore, the electron rich aromatic system can participate in cation-π interactions that, in a protein context, can exist between the aromatic system of phenylalanine, tryptophan or tyrosine and a cationic moiety from the side-chain of arginine or lysine. As demonstrated by Gallivan *et al.*, from the canonical aromatic amino acids, Trp mediated cation-π interactions are the more energetically favourable and about 26 % of all Trp are involved in such type of interactions.[225] Therefore, Trp adds hydrophobic bulkiness and stereo constrains at the *N*-terminal and the possibility of hydrogen bonding, cation–π contacts and π-π stacking interactions. In addition, due to its positive α-helical propensity,[226] tryptophan incorporation should not disturb the α-helical conformation to a greater extent. To study the charge and hydrophobicity, three Trp peptides variants were synthesized: RF04 where the amine is free, RF05 where the amine is *N*-Fmoc protected, and RF06 where the amine is acetylated (**Figure 4.15**).

Furthermore, inspired by the works of the group of Ulijn on the use of Fmoc-dipeptides as scaffolds for self-assembly,[227] RF08 was synthesized where the terminal amine was kept protected with the commonly used Fmoc protecting group.

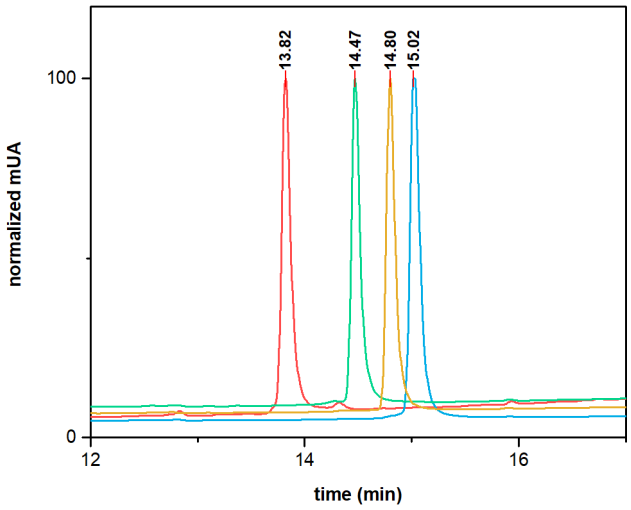

Figure 4.16. Hydrophobic character of the tryptophan and Fmoc-protected variants as a measure of retention time by reverse-phase HPLC. Truncated normalized HPLC data depicting the retention time for RF04 (red trace), RF05 (blue trace), RF06 (green trace) and RF08 (yellow trace). Conditions: 5 to 100 % acetonitrile (with 0.1 % TFA) in 20 min at 1 mL min^{-1}.

As accordingly to our design, peptide hydrophobicity increases with the introduction of bulkier Fmoc residues (**Figure 4.16**).

The secondary conformation was studied immediately after solution preparation and after the thermal denaturation experiments (**Figure 4.17**). RF04 and RF06 were readily dissolved in the respective buffer conditions; in contrast RF05 and RF08 exhibited low solubility in both pH conditions, and the formation of a white precipitate was macroscopically evident for RF05. As judging by the CD spectra, all peptides fold into a predominantly α-helical conformation as observed by the presence of double minima around 208 and 222 nm.

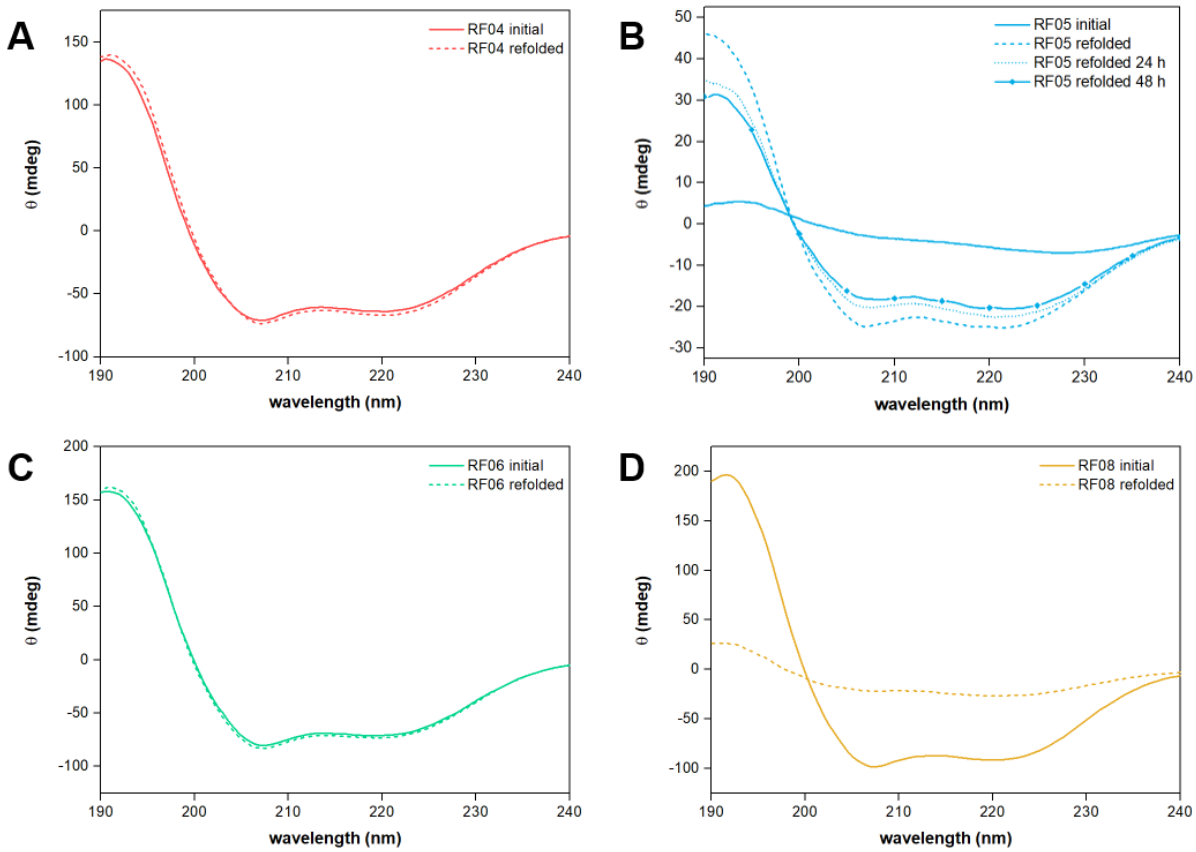

Figure 4.17. CD spectra under benign conditions for RF04-RF06 and RF08. (**A**) RF04; (**B**) RF05; (**C**) RF06; (**D**) RF08. Conditions: peptide concentration 0.1 mM in 50 mM phosphate buffer, pH 7.4, 20 °C. CD after solution preparation (solid trace) and after the thermal denaturation experiment (dashed trace).

Figure 4.18 A shows the variation of ellipticity at 222 nm as a function of temperature from 20 to 95 °C (at 3 °C min^{-1}). With exception of RF05, all peptides show loss of secondary structure with increasing temperature. In all cases, retention of residual ellipticity (~ 20 mdeg) at temperatures up to 95 °C was observed. The apparent melting temperature was determined as the mid-point of the denaturation curve (inset). RF04 and RF06 shows similar denaturation curves, that translates into similar melting temperatures (57.8 °C for RF04 and 59.0 °C for RF06). This indicates that, under neutral conditions, the charge state at *N*-terminus of the tryptophan moiety has little influence over the peptide stability. In contrast, RF05 exhibits a linear spectrum with little to no response to temperature, and no melting temperature could be determined.

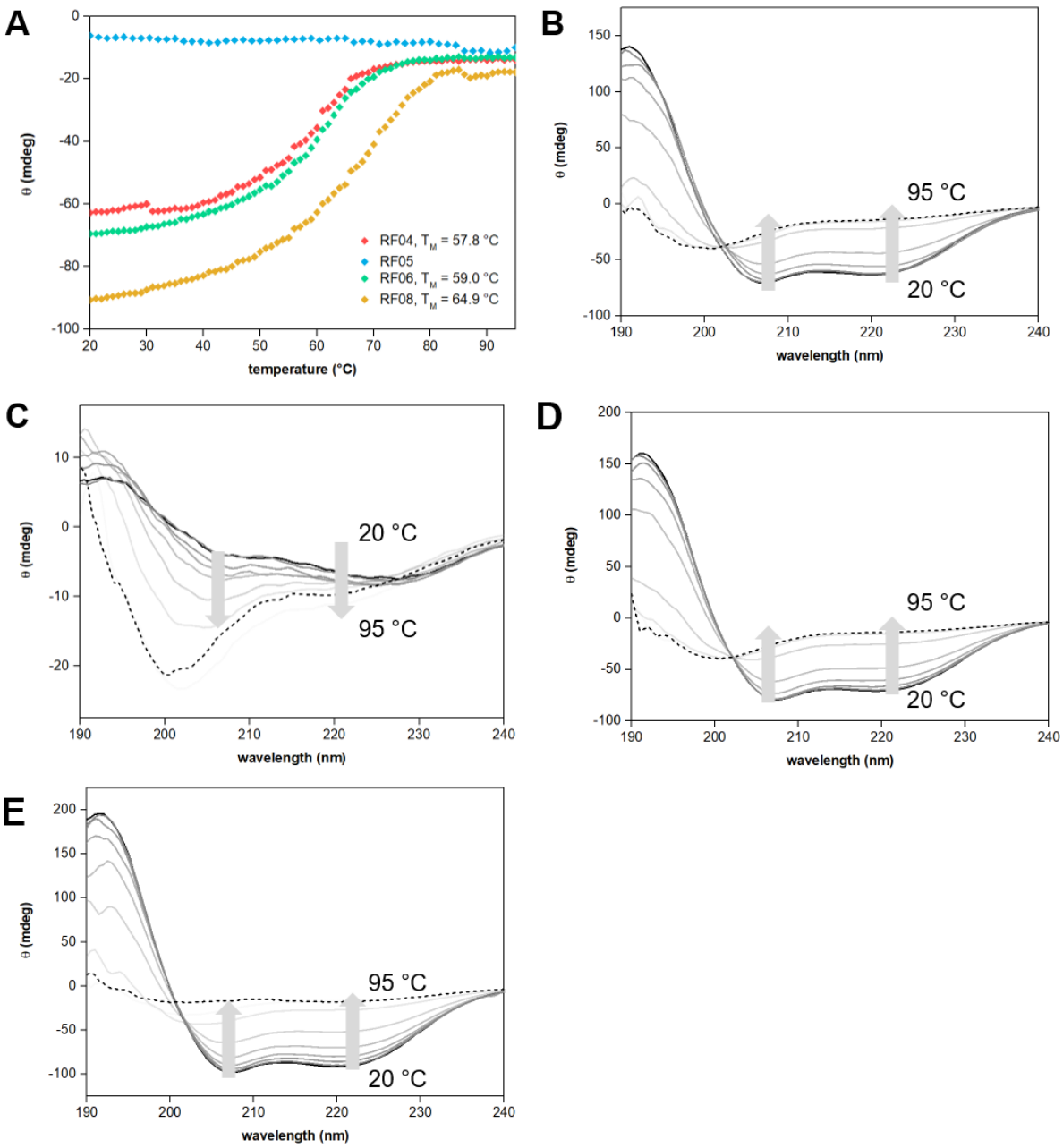

Figure 4.18. Temperature-dependent CD spectra for RF04-RF06 and RF08 under neutral conditions. (**A**) Variation of ellipticity at 222 nm with increasing temperature with the apparent T_M on the inset, for RF04 (red trace), RF05 (blue trace), RF06 (green trace) and RF08 (yellow trace). Peptide concentration: 0.1 mM. **B-E.** Full spectra analysis recorded at 5 °C intervals with increasing temperature for (**B**) RF04, (**C**) RF05, (**D**) RF06 and (**E**) RF08.

To obtain more information about the peptide's behaviour against temperature, the full spectra were recorded at 5 °C intervals while increasing the temperature from 20 to 95°C (at 3 °C min^{-1}) (**Figure 4.18 B-E**). Peptides RF04, RF06 and RF08 show a progressive loss in secondary structure with increasing temperature, as indicative by the single minimum at 200 nm at 95 °C. In addition, the presence of an isodichroic point ~ 203 nm indicates a two-state transition between helical and random-coil.[228,229] RF05 shows a more complex behaviour, with a slight increase on the ellipticity at 222 nm with temperature. Presence of a double minimum at 200 and 222 nm suggests that a combination of helical and random coil might still exist at 95 °C.

Upon thermal annealing, the peptides refold into an α-helical conformation. Interestingly, both RF05 and RF08 show a very significant variation on the degree of helicity, with an increase for the case of RF05 and a decrease for RF08. For both cases, development of a precipitate was evident after peptide annealing, suggesting the occurrence of aggregation. Inspection of the solutions by negative staining TEM show formation of a mesh of thin fibrils for RF05 (**Figure 4.19**). No defined structures were observed for the remaining peptides.

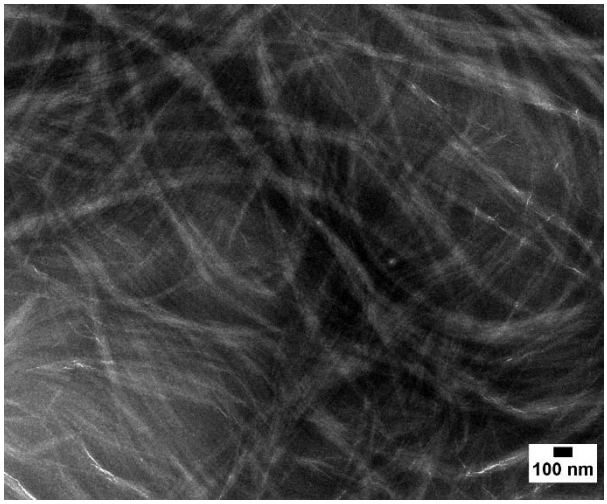

Figure 4.19. Representative negative-staining TEM of RF05 under neutral pH. Conditions: 0.1 mM, 50 mM phosphate buffer, pH 7.4.

The following step was to study the peptide behaviour against acidic pH. **Figure 4.20** shows the CD spectra for the peptides at pH 3.4. Both RF04 and RF06 were readily soluble under this condition, while for the remaining RF05 and RF08 there was evidence of a white precipitate. All peptides exhibit maintenance of the □-helical folding motif, with double minima at around 208 and 222 nm. However, reflecting their low solubility, both RF05 and RF08 show low CD intensity.

By monitoring the changes in ellipticity at 222 nm with temperature, only RF04 and RF08 gave a sigmoidal thermal denaturation curve, consistent with thermal unfolding from helical to unordered conformation. For these two peptides the apparent melting temperatures of 66.1 °C for RF04 and 88.3 °C for RF08 show that the peptides are more stable at pH 3.4 than at pH 7.4. Interestingly, an incomplete transition occurred for RF06 suggesting that this peptide is highly stable to temperatures up to 95 °C. In a similar behaviour as for pH 7.4, RF05 show little response to temperature (**Figure 4.21 A**).

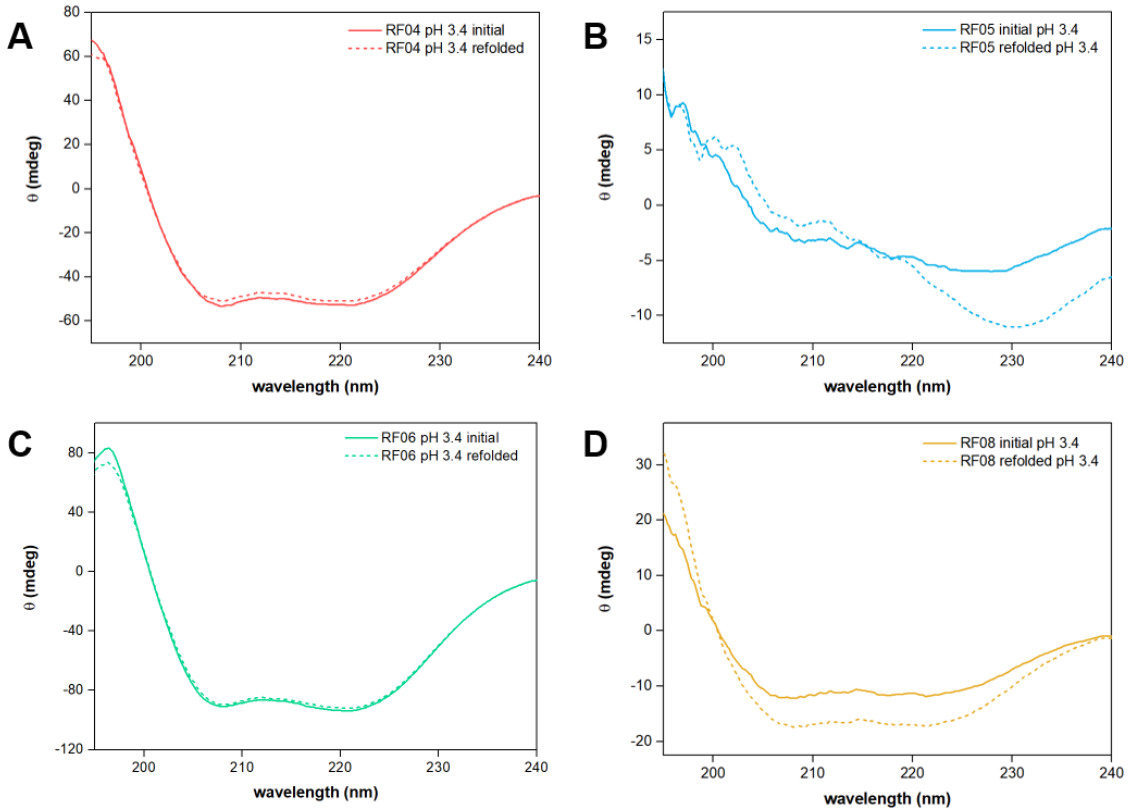

Figure 4.20. CD spectra at 25 °C under pH 3.4 for RF04-RF06 and RF08. (**A**) RF04, (**B**) RF05, (**C**) RF06 and (**D**) RF08. Conditions: peptide concentration 0.1 mM in 50 mM citrate buffer, pH 3.4, 25 °C. CD after solution preparation (solid trace) and after the thermal denaturation experiment (dashed trace).

Recording the changes on the full spectra at 5 °C intervals revealed a similar behaviour as for pH 7.4. That is, peptides RF04, RF06 and RF08 exhibit a decrease on the CD signal intensity and the development of a minimum at around 203 nm, indicative of a transition from helical conformation to random coil. RF05 showed a slight increase of ellipticity and the development of a minimum around 200 nm, suggesting a combination of helical and random conformation under this temperature occurs also under acidic pH.

Upon thermal annealing, both RF04 and RF06 refold into an α-helical conformation with no significant changes in the ellipticity, demonstrating a high conformational stability. RF05 exhibits an increase on the CD signal with red-shifting of the spectra, with a strong minimum at 229.8 nm. This result suggests the formation of high-order aggregates in solution.[60] RF08 shows a slight increase of helicity. For both cases, development of a precipitate was evident after peptide annealing, suggesting the occurrence of aggregation.

Inspection of the solutions by negative staining TEM showed the spontaneous formation of defined structures for RF04, RF05 and RF08. RF04 assembles into long and thin fibrils that underwent further lateral assembly, twisting and entanglement (**Figure 4.22 A**). In addition, dense networks of fibrils were observed (**Figure 4.22 B**). RF05 assembles into unbranched fibrils with several hundred nanometres long and an average width of 2.65 nm (± 0.46 nm in 10 measurements) (**Figure 4.22 C, D**). Most surprisingly, RF08 shows the formation of large sheet-like aggregates with several hundred nanometres in length and width (**Figure 4.22 E**). Mimicking the first generation RF01, a regular striation pattern was present throughout the entire length of these microsheet structures. It should be emphasized that the structures on **Figure 4.22 E** and **F** are in a frozen-hydrated state, without the influence of any staining solution, thus closely represent the native state of the peptides. The fast-Fourier-transform (FFT) analysis revealed a 4.4 nm separation between the striations.

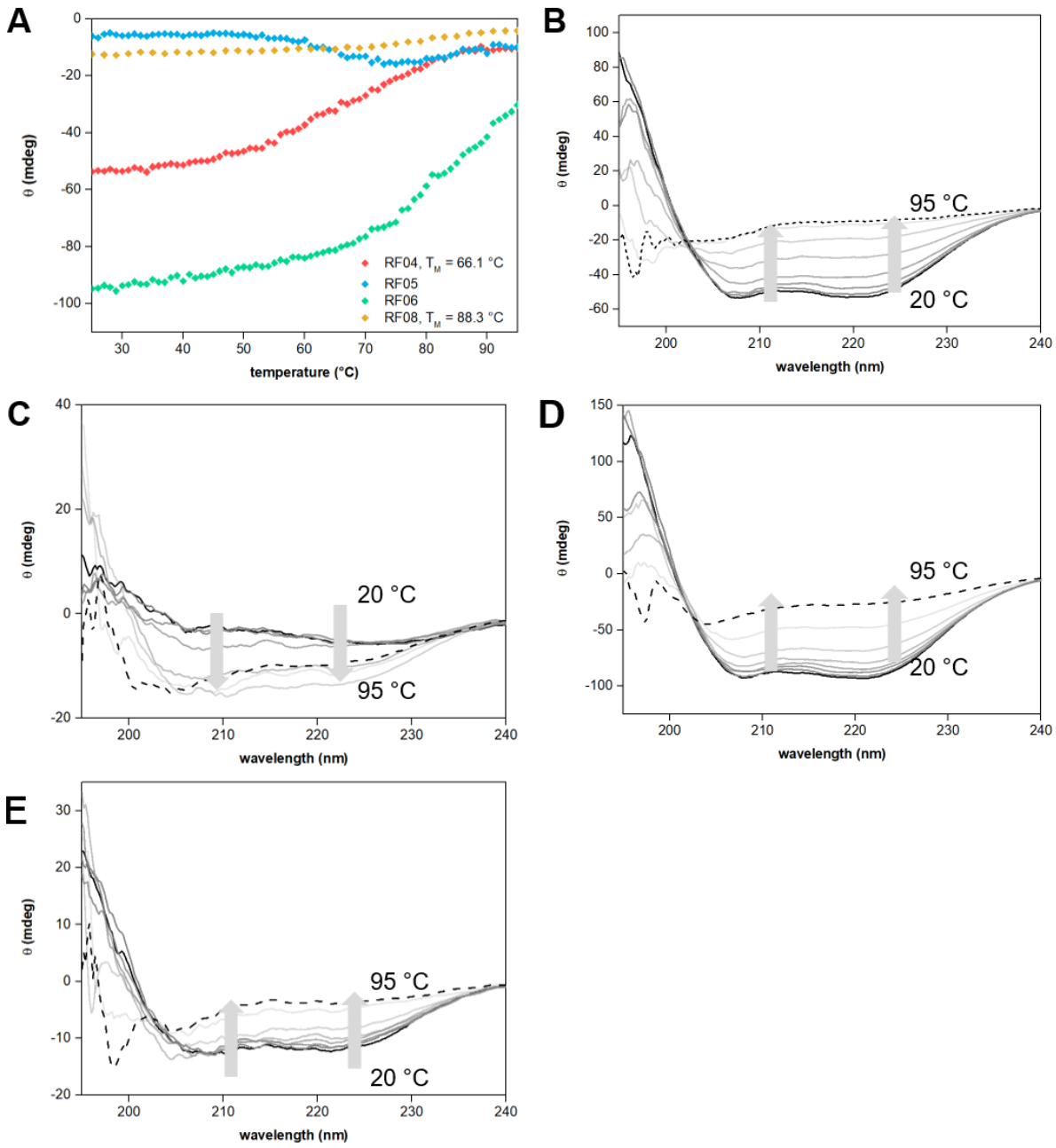

Figure 4.21. Temperature-dependent CD spectra for RF04-RF06 and RF08, under acidic conditions. (**A**) Variation of ellipticity at 222 nm with increasing temperature with the apparent T_M on the inset, for RF04 (red trace), RF05 (blue trace), RF06 (green trace) and RF08 (yellow trace). Peptide concentration: 0.1 mM. **B-E.** Full spectra analysis recorded at 5 °C intervals with increasing temperature for (**B**) RF04, (**C**) RF05, (**D**) RF06 and (**E**) RF08.

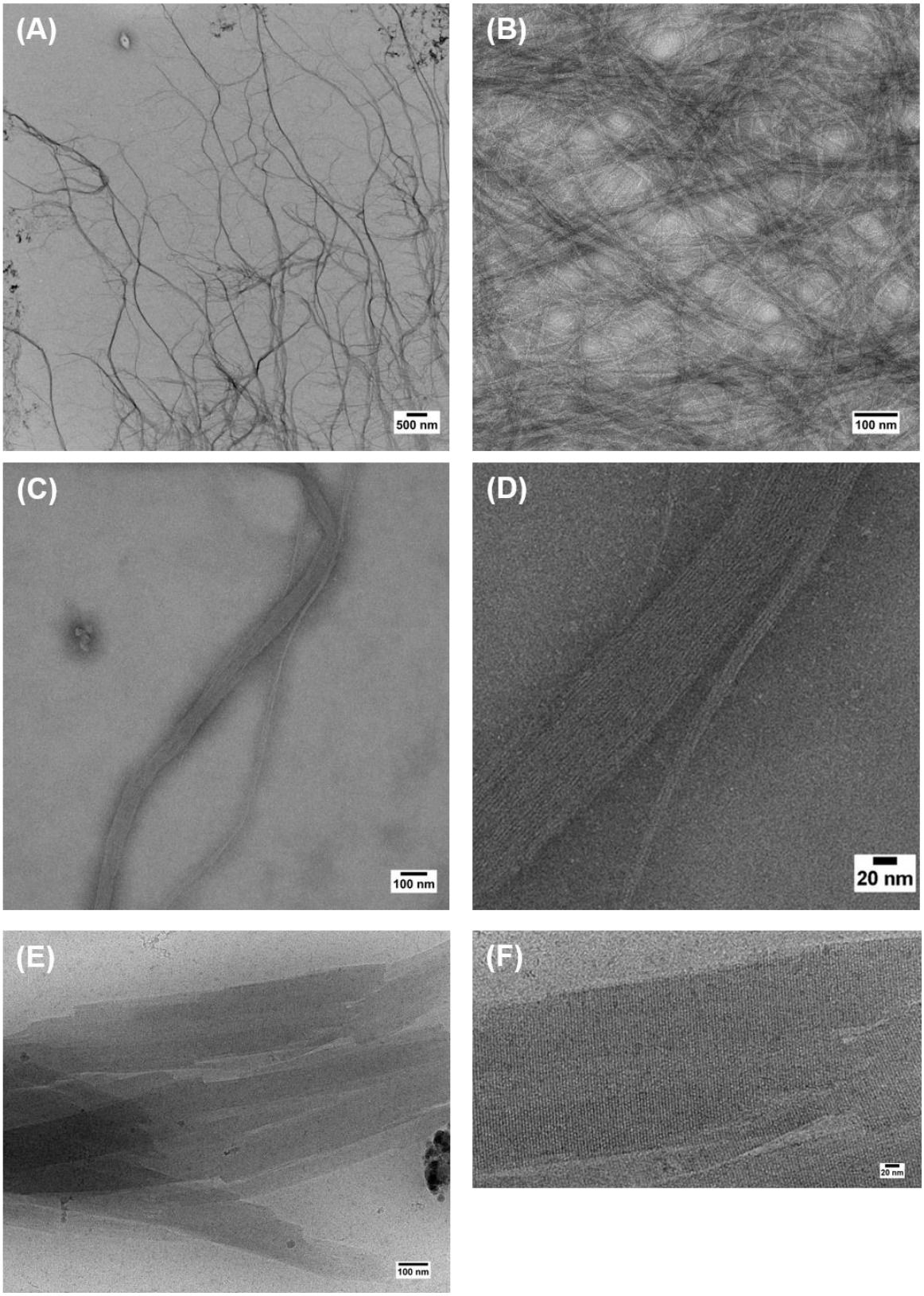

Figure 4.22. Representative TEM micrographs of RF04, RF05 and RF08 at pH 3.4. (**A, B**) RF04; (**C, D**) RF05; (**E, F**) RF08. Peptide concentration: 0.1 mM. (**A-D**) negative staining TEM, (**E-F**) cryo-TEM.

In order to design new supramolecular structures with desired morphology and function, it is essential to understand how these assemblies are formed and how the morphology can be controlled.[79] Redesigning RF01 by a single-residue mutation at the *N*-terminus, both stability and the supramolecular arrangement were dramatically changed. Specifically, under neutral conditions all peptides showed less thermal stability, while under acidic conditions only RF06 shows identical stability as RF01.

Because of the design features, these peptides are disposed to aggregate by a combination of several noncovalent interactions, with π–π stacking between the aromatic moieties of either tryptophan or Fmoc as major driving force. However, a balance between hydrophobicity and electrostatic interactions was critical for peptide stability and molecular organization within the assemblies. From the data collected in this and in the previous project, it seems evident that protonation of glutamic acid favours peptide assembly. Under acidic conditions, unfavourable interactions between the negatively charged glutamic acid and the electron π-system of either tryptophan or Fmoc are absent, and stabilization and aggregation might be a combination of several effects. Namely, absence of unfavourable same charge interactions from unionized glutamic acid, presence of conventional hydrogen bonding between the indolic NH and the carbonyl of glutamic acid, and presence of favourable cation-π between the charged side-chain groups of lysine and the π-systems. RF05's ability to assemble independently on the pH of the solution is likely a consequence of the large double aromatic system provided by the incorporation of both tryptophan and fluorenyl moieties. Here, the strong π–π stacking overcome any unfavourable interaction. For the case of RF04 the situation is inversed, as the presence of a charged amine group at *N*-terminus results in repulsive interactions with the neighbouring charged residues and leads to a thermal destabilization and formation of amorphous aggregates. The fact that RF06 and RF08 only exhibited self-assembly under acidic environments have potential for the development of smart biomaterials. For example, these peptides can be potentially used for drug delivery to tumours, as cancerous tissues are known to exhibit an extra- and intracellular acidic environment,[230] or be used in the cosmetic field, since the skin pH is slightly acidic (pH approximately of 5)[231].

4.3. Hydrophobic effect on the conformation, stability and extension of assembly

Numerous weak noncovalent interactions drive self-assembly. In particular, the hydrophobic effect is a powerful tool to promote high-order organization. In an aqueous environment, the amphipathic nature of coiled-coils guides the folding in order to maximize hydrophobic contacts and to bury them from the solvent. In the coiled-coil motif, it is generally accepted that hydrophobic interactions between residues placed in positions *a* and *d* play a major role in peptide overall stability and the three-dimensional arrangement.[232] Several other important factors, such as electrostatic interactions, α-helical propensity, and amino acid content also contribute to peptide stability. In this project, RF01 was redesigned in an attempt to increase peptide stability while preserving peptide's ability to assembly into higher-order constructs.

Analysis of natural leucine zipper sequences have demonstrated that positions ***d*** are less tolerable to substitution than positions ***a***.[233,234] As such, two new RF01 variants were designed were only leucine residues in positions ***a*** were substituted (**Figure 4.23** and **Table 4.2**). To amplify their effect, multiple substitutions were made simultaneously. The RF011 and RF012 peptides described in this project follow the same design principles as previously explained. Briefly, position ***d*** is occupied exclusively with leucine residues, the flanking positions ***e*** and ***b*** and ***g*** and ***c*** were occupied with lysine and glutamate, respectively. The remaining position, ***f***, was occupied with serine. In addition, the same Cy5-derived chromophore was coupled to the *N*-terminus and the *C*-terminus was kept unprotected.

Table 4.2. Peptide sequences used in this project.

Peptide[a]	*defg*	*abcdefg*	*abcdefg*	*abcdefg*	*abcd*
RF011	LKSE	**F$_3$V**KELKSE	**F$_3$V**EKLKSE	**F$_3$V**KELKSE	LKEL
RF012	LKSE	**I**KELKSE	**I**EKLKSE	**I**KELKSE	**I**KEL

[a]In both cases the *N*-terminus is cy5-protected, and the *C*-terminus is free.

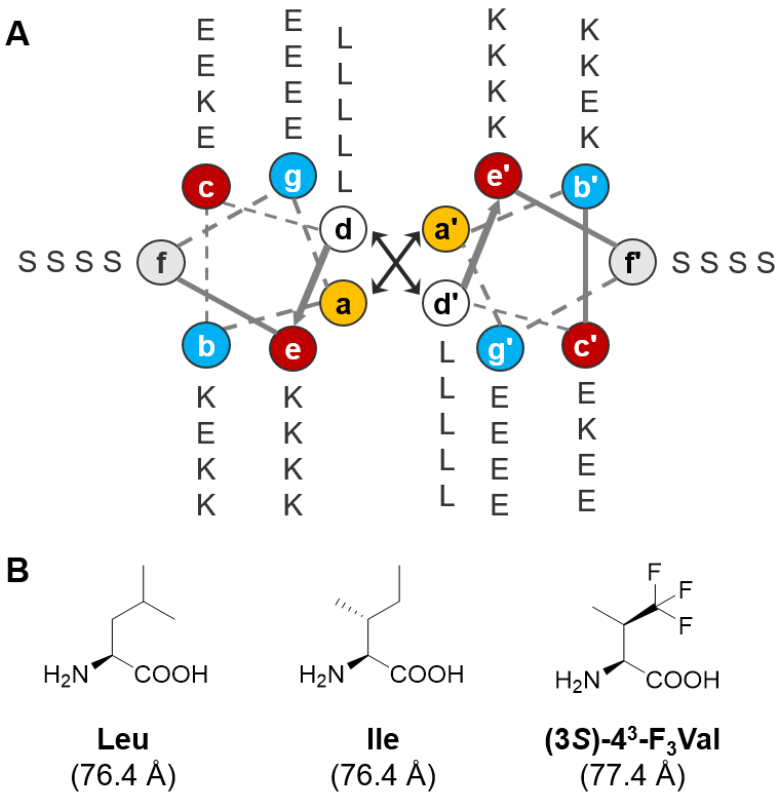

Figure 4.23. **Helical wheel and chemical structures of the incorporated amino acids.** (**A**) Helical wheel representation of the coiled-coil motif where only positions ***a*** within the hydrophobic core (yellow) were substituted and the remaining were preserved from the original RF01 scaffold RF01. (**B**) Chemical structures of the residues incorporated at ***a*** positions with the respective van der Waals volume calculated according to Zhao *et al*.[235]

Peptide RF011 and RF012 differ as follows. On peptide RF011, three leucine residues in positions ***a*** were substituted with trifluorovaline (4^3-F_3V). Incorporation of fluorine in biological relevant molecules has become a promising strategy for modulating their properties. The success of fluorine is a direct consequence of its unique characteristics, namely small size, low polarizability and the highest electronegativity among all elements. Although replacement of hydrogen with fluorine is considered to be "sterically quite conservative"[141], its incorporation has a profound impact on the physicochemical properties of molecules, such as hydrophobicity, pK_a and chemical reactivity.[120,142] However, and as previously discussed (**Section 2.3.3** and **2.3.4**), the effect of fluorine incorporation within the helical core cannot be generalized, and depends on the fluorine content as well as

on the surrounding environment. In addition, the impact of fluorination of the hydrophobic core of a fiber forming coiled-coil was seldom studied.[174]

On peptide RF012, four leucine residues were substituted with isoleucine. This amino acid was chosen as its side chain is very similar as 4^3-F_3V side chain, thus allowing to better differentiate between a specific effect from fluorine and the increase in side-chain volume.[236] In addition, studies of known coiled-coils have shown that β-branches amino acids have a strong contribution to coiled-coil stability with minimal disturbance of the helical conformation.[234]

When buffered at pH 7.4, both peptides show an initial low solubility and the presence of macroscopically particulates was evident. However, when heating the solution to 95 °C and cooling it down to room temperature, disruption of the larger particulates and formation of a disperse and fine precipitate was evident. This behaviour mimics the one observed for the first-generation peptide RF01. Consistently, inspection of the samples 24 h after the thermal denaturation experiments confirmed that both peptides form long, striated rods with dimensions from several micrometre in length and over hundred nanometre in width (**Figure 4.24**). The same apparent internal order was observed, as evidenced by the striation pattern perpendicularly to the long axis. The fast-Fourier transform analysis of the distance between striations gave a value of 4.6 ± 0.04 nm for RF011 and 4.2 ± 0.07 nm for RF012, a 0.2 nm increase or decrease, respectively, in comparison to RF01 (4.4 nm).

As such, the introduction of the fluorinated amino acids or isoleucine has minimal impact the packing of the peptides within the rods. For the case of RF011, the increase on the separation distance between striations might be a consequence of the slightly larger van der Waals radius for trifluorovaline. In contrast, the decrease for RF012 indicates that isoleucine was better accommodated within the helical core and the helices are more tightly packed together.

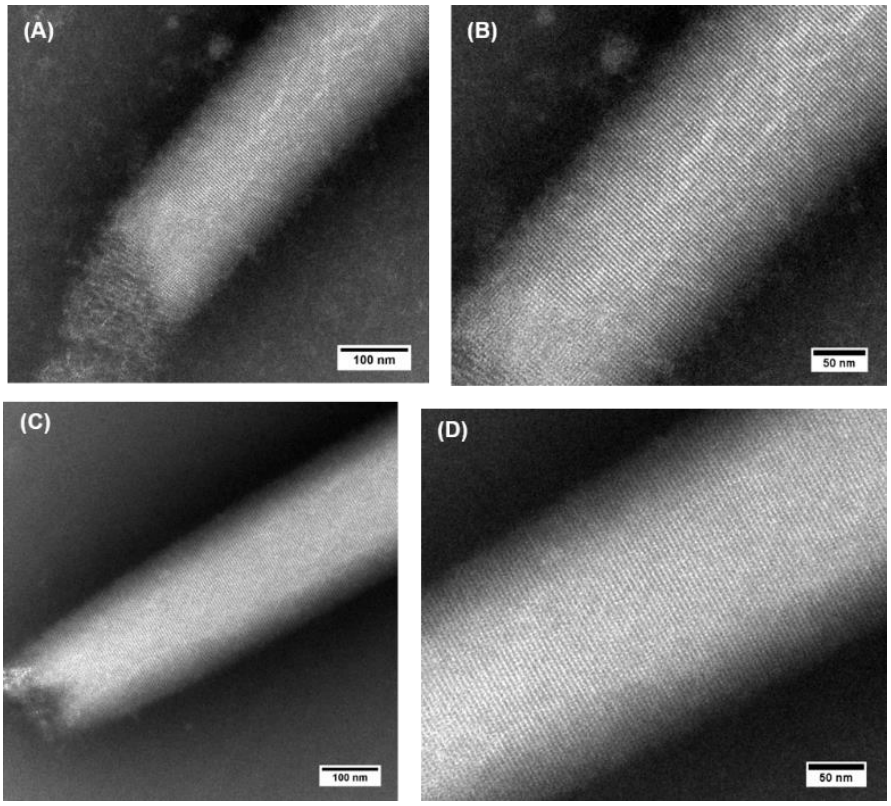

Figure 4.24. Representative negative-staining TEM micrographs at pH 7.4. (**A**, **B**) RF011 and (**C**, **D**) RF012. Peptide concentration: 0.1 mM. Micrographs obtained 24 h maturation after thermal denaturation.

These structures were further analysed by infrared nano-spectroscopy. **Figure 4.25** shows a representative topographical image and the local infrared absorption spectrum of RF011. Here, a clear disruption of the compact rod morphology can be observed. This might be a consequence of sample preparation or peptide degradation. Nevertheless, the infrared absorption spectrum at different positions within the structure revealed two strong peaks, one at 1550 cm^{-1} referring to the amide II bond and at 1660 cm^{-1} that correlates with the amide I bond frequency. This indicates that the peptide is in an α–helical conformation.

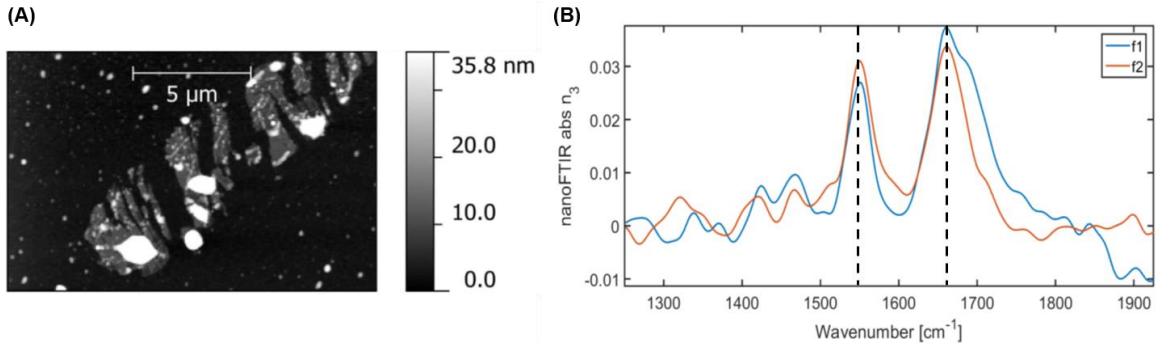

Figure 4.25. Infrared nano-spectroscopy of RF011 at pH 7.1. Representative AFM image(**A**), nano-FTIR spectrum taken in two different positions (**B**). Peptide concentration: 0.1 mM in 50 mM phosphate buffer.

Figure 4.26 shows representative topographical images and the local infrared absorption spectrum of RF012 under benign pH conditions. In this case, AFM confirms the morphology previously observed by negative-staining TEM with the presence of long, unbranched rods with and apparent thickness below 100 nm. The infrared absorption spectrum at different positions within the structures revealed a band at 1549 cm^{-1} and 1660 cm^{-1} referring to the amide II and amide I bond frequency, respectively. Thus, the rod structures are formed by peptides predominantly in an α-helical conformation.

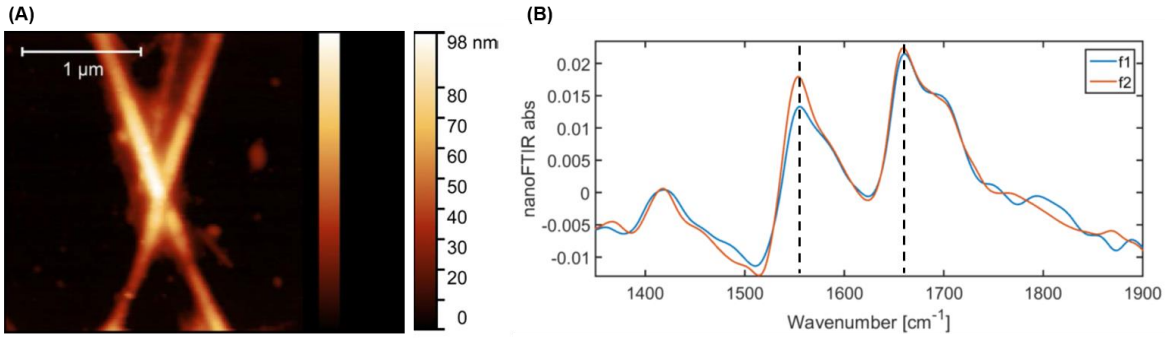

Figure 4.26. Infrared nano-spectroscopy of RF012 at pH 7.4. Representative AFM images (**A**), representative AFM images and nano-FTIR spectrum taken in two different positions (**B**). Peptide concentration: 0.1 mM in 50 mM phosphate buffer.

Analysis by CD confirmed the predominance of helical conformation for RF011 and RF012. In either case, the CD profile shows two major negative bands around 208 and 222 nm and a maximum around 195 nm. However, because of formation of

large aggregates, the CD spectra was distorted regarding to the typical spectrum for α-helical conformations. That is, the attenuation of the band around 208 nm and slight red shift towards higher wavelength. As such, the value for the helical content was not possible to accurately determine. Nevertheless, in a qualitative analysis, the non-fluorinated variant is more helical than its fluorinated analogue. This decrease of ellipticity mirrors the unfavourable helix propensity of fluorinated amino acids regarding to their non-fluorinated analogues. However, although the zero helical propensity of 4^3-F_3V,[149] the incorporation of three fluorinated residues is not significant to completely disrupt the α-helical motif. The same effect has been reported by the Koksch group[170,173] and by others[157], and suggests a lower influence of the helical propensity in the context of large and complex peptide assemblies.

In addition, in a similar behaviour as previously reported (**Section 4.1**), the initial low CD intensity is significantly increased upon thermal denaturation and refolding of the peptide solutions.

To compare the behaviour against temperature, both peptide solutions were heated from 25 to 95 °C at a rate of 3 °C min^{-1} while monitoring the CD signal at 222 nm (**Figure 4.28**). The experiment was first performed after solution preparation and then 24 h after the first thermal denaturation. In the 24 h period, both solutions were allowed to mature at room temperature. For both peptides, the thermal denaturation process is reversible, allowing both peptides to anneal.

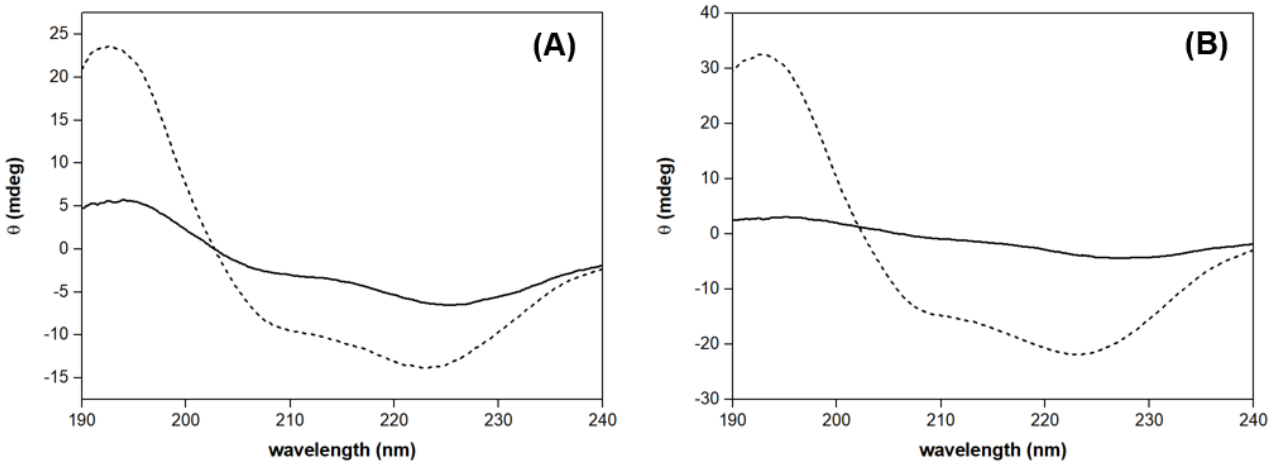

Figure 4.27. CD spectra for at pH 7.4 at 25 °C. (**A**) RF011 and (**B**) RF012. Conditions: 0.1 mM in 50 mM phosphate buffer pH 7.4. CD after solution preparation (solid trace) and after the thermal denaturation experiment (dashed trace).

RF011 exhibits broad sigmoidal curves and an apparent melting temperature of 63 and 70 °C for the first and second denaturation experiment, respectively. Surprisingly, this fluorinated variant is slightly less stable when compared to the canonical RF01 (73 °C). In contrast, when compared with the only reported fluorinated coiled-coil fibers,[174] RF011 is approx. 30 °C more stable. However, it should be noted that the lower melting temperature reported might be a consequence on the use of a racemic mixture of fluorinated amino acids.[174] A better understanding of the specific influence of fluorine in this peptide construct is impaired by the absence of more detailed structural data. However, the differences here observed might be argued by the same principles guiding peptide stability, namely the packing of the side chains and entropic effects. That is, introduction of the slightly larger fluorine results in a less efficient packing of the side-chains within the hydrophobic core, and the loss of conformational entropy through steric clashes between the fluorinated side-chain and the helix backbone.[156,237]

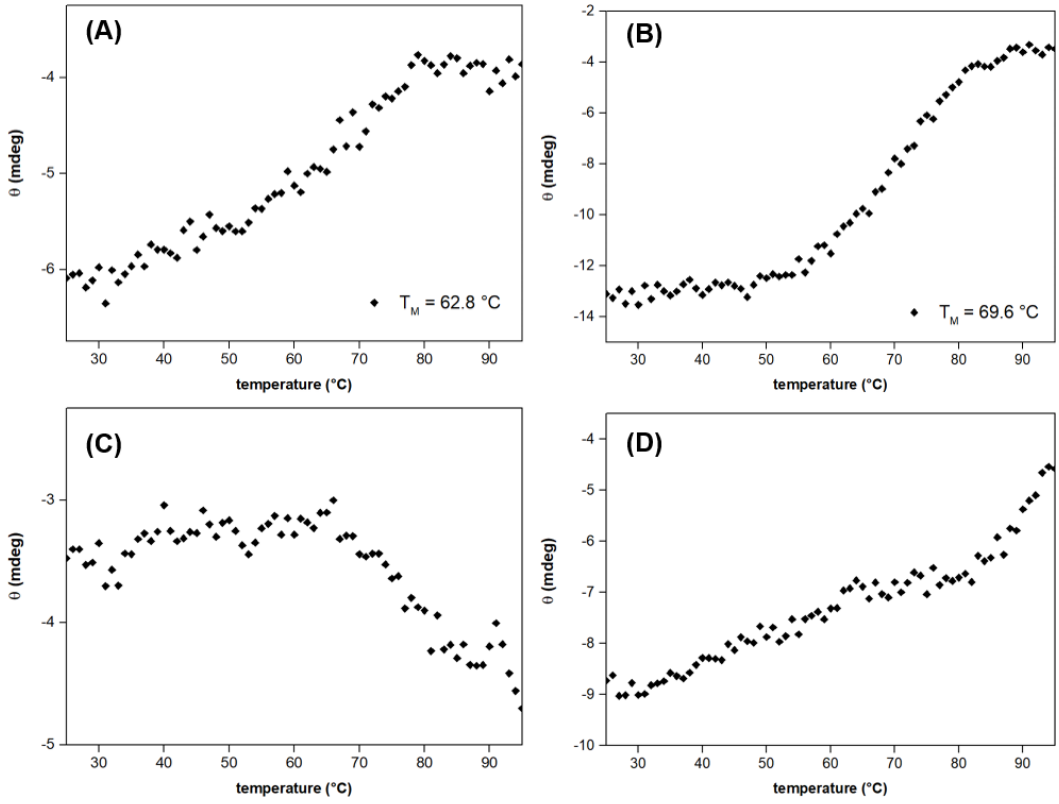

Figure 4.28. Thermal denaturation curves at pH 7.4. (**A**) RF011 first denaturation curve, (**B**) RF011 second denaturation curve, (**C**) RF012 first denaturation curve and (**D**) RF012 second denaturation curve. Conditions: 0.1 mM peptide in 50 mM phosphate buffer pH 7.4. From 25 to 95 °C at 3 °C min^{-1}.

In contrast, on a first denaturation experiment, RF012 shows little response to temperature while on a second experiment, a progressive weakening of the CD signal at 222 nm indicates the loss of helical conformation with temperature. However, no plateau was reached to temperatures up to 95 °C, indicating high stability of RF012. In comparison to RF01, introduction of four isoleucine residues within the hydrophobic core results in a remarkable increase of thermal stability (73 °C *vs* > 95 °C).

The decoration of the hydrophobic core with fluorinated amino acids has the potential to disrupt self-assembly at low pH. To probe the effect of acidic conditions on the assembly propensity, solutions buffered at pH 3.4 were analysed by negative-staining TEM (**Figure 4.29**). No membrane-like structures were observed in either peptide. Instead, RF011 exhibited amorphous and floccular assemblies (**Figure 4.29 A, B**) and nanoscale structures that are likely peptide monomers or small oligomers (**Figure 4.29 C**). Interestingly, RF012 showed a mixture of morphologies, with spherical and floccular assemblies, and also unstructured nanoscale structures (**Figure 4.29 D-F**).

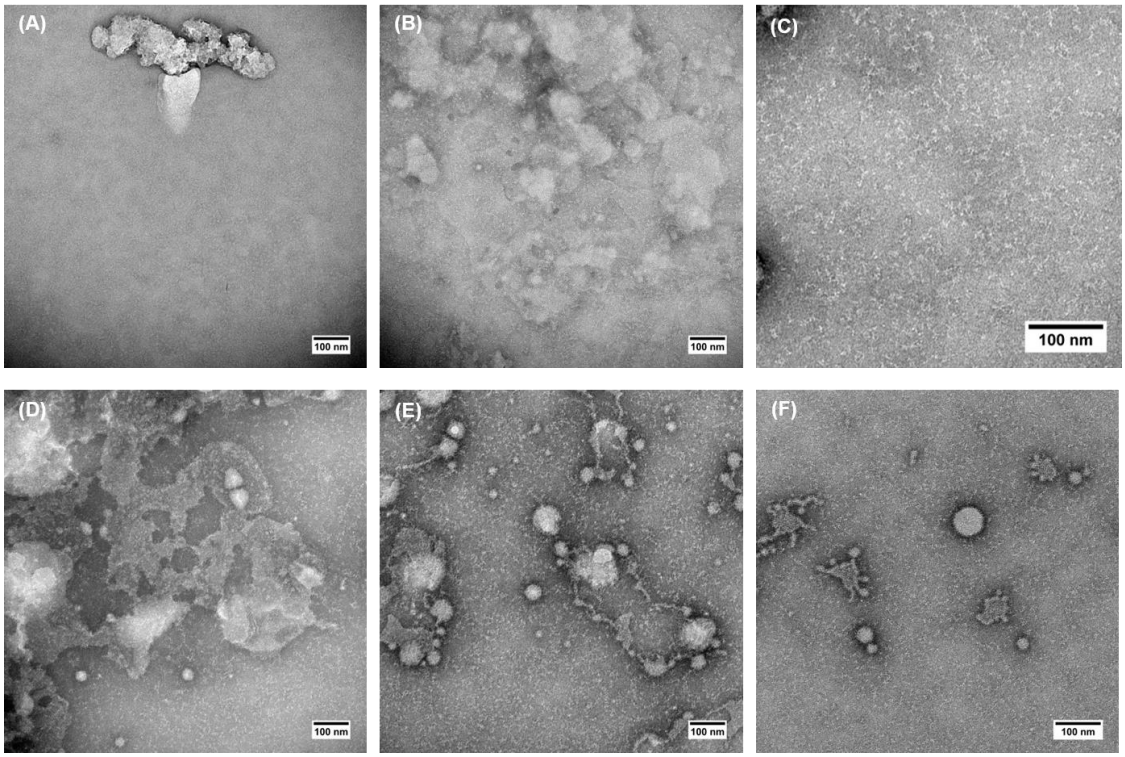

Figure 4.29. Representative negative-staining TEM micrographs at pH 3.4. (**A-C**) RF011 and (**D-F**) RF012. Peptide concentration: 0.1 mM. Micrographs obtained 24 h maturation after thermal denaturation

Further analysis by infrared nano-spectroscopy for RF011 confirms the observation by negative-staining TEM, with formation amorphous structures with a high height, likely clusters of monomeric peptides (**Figure 4.30 A**). The infrared absorption spectrum at different positions within the structures revealed a band at 1559 cm^{-1} and 1657 cm^{-1} referring to the amide II and amide I bond frequency, respectively. A great contribution of the citrate buffer was observed by the strong absorption band at 1725 cm^{-1} (**Figure 4.30 B**).

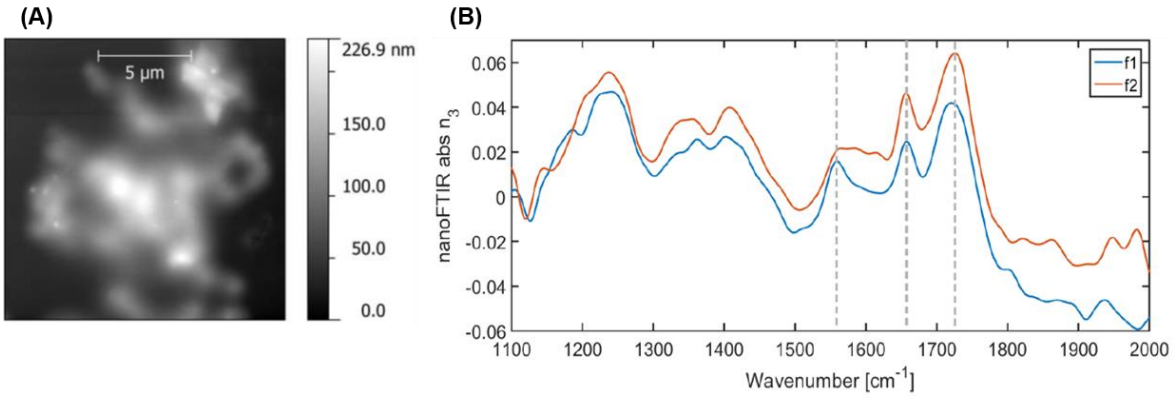

Figure 4.30. Infrared nano-spectroscopy of RF011 at pH 3.4. (**A**) Representative AFM image, and (**B**) nano-FTIR spectrum taken in two different positions within the structure. Peptide concentration: 0.1 mM.

For RF012, a seemingly different morphology was observed by infrared nano-spectroscopy (**Figure 4.31**). However, it should be noted here that sample preparation for either technique might account morphology disparity, as by TEM it might be a consequence of the staining solution, and by infrared nano-spectroscopy analysis a consequence of spin coating of the sample in the gold substrates. More data is needed to elucidate the differences observed. Nevertheless, when probing the structures formed by RF012, both low and higher height areas were observed. FTIR and infrared near-field phase images at different frequencies revealed that the higher height areas likely correspond to citrate buffer trapped underneath the structure (**Figure 4.31**).

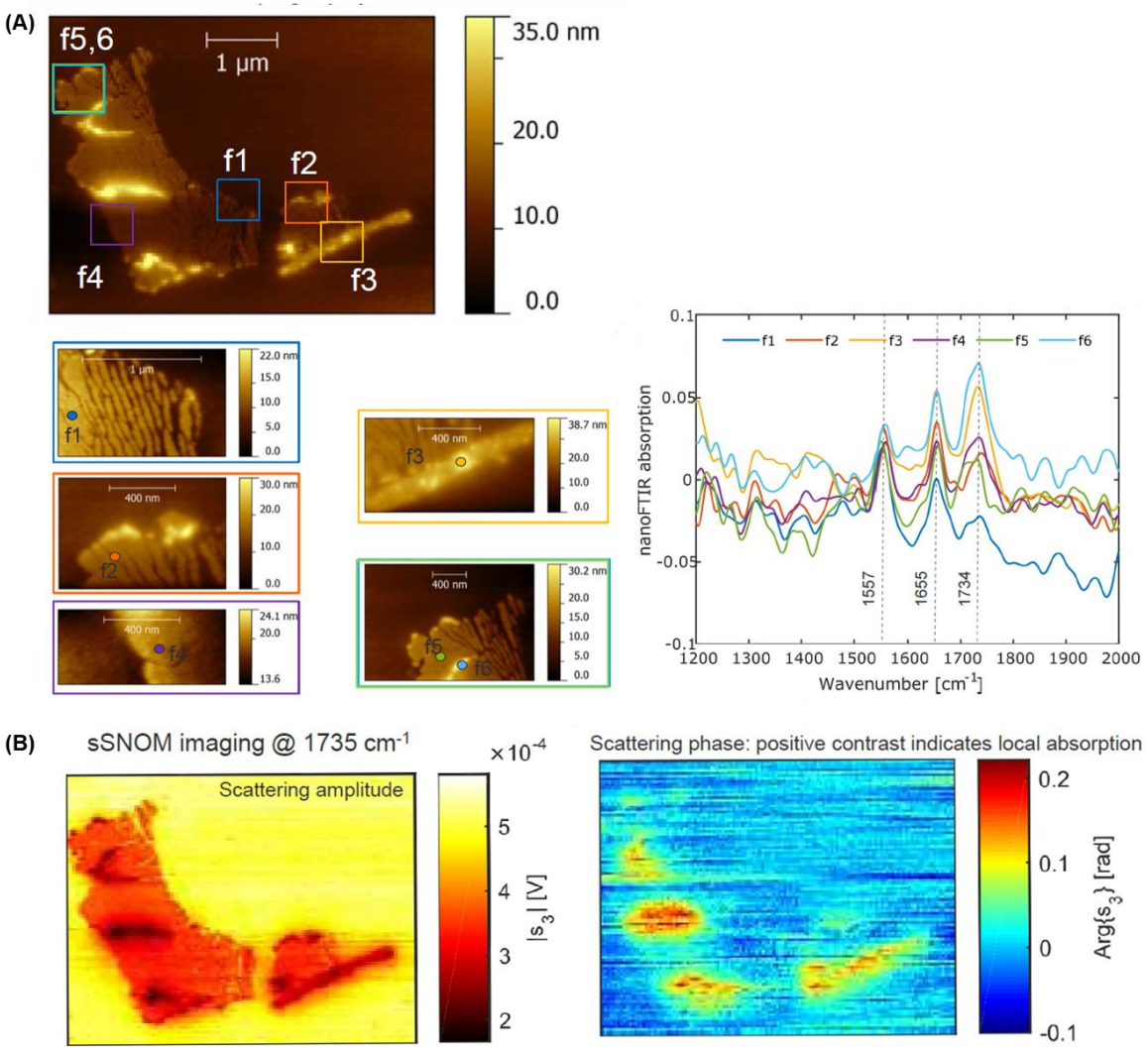

Figure 4.31. Infrared nano-spectroscopy of RF012 at pH 3.4. (**A**) Representative AFM image; (**B**) nano-FTIR spectrum taken in different positions within the structure; (**C**) sSNOM imaging of the surface at 1735 cm^{-1} and scattering phase. Peptide concentration: 0.1 mM.

CD spectroscopy of RF011 and RF012 solutions buffered at pH 3.4 confirms that both peptides fold into predominantly an α-helical conformation, as observed by the double negative minima at around 208 and 222 nm and a positive maximum at around 195 nm (**Figure 4.32 A, B**).

The thermal denaturation at pH 3.4 was studied by heating the peptide solutions from 25 to 95 °C at a rate of 3 °C min^{-1} while monitoring the CD signal at 222 nm (**Figure 4.32 C, D**). RF011 exhibits a broad sigmoidal curve and an apparent melting temperature of approx. 73 °C. This result suggests that formation of the supramolecular structures observed for pH 7.4 do not stabilize the peptide. In fact, a 3 °C increase in stability was observed when no high-order architecture was formed. The same argument can be made for RF012, where no thermal transition was observed and residual ellipticity still occurred to temperatures up to 95 °C.

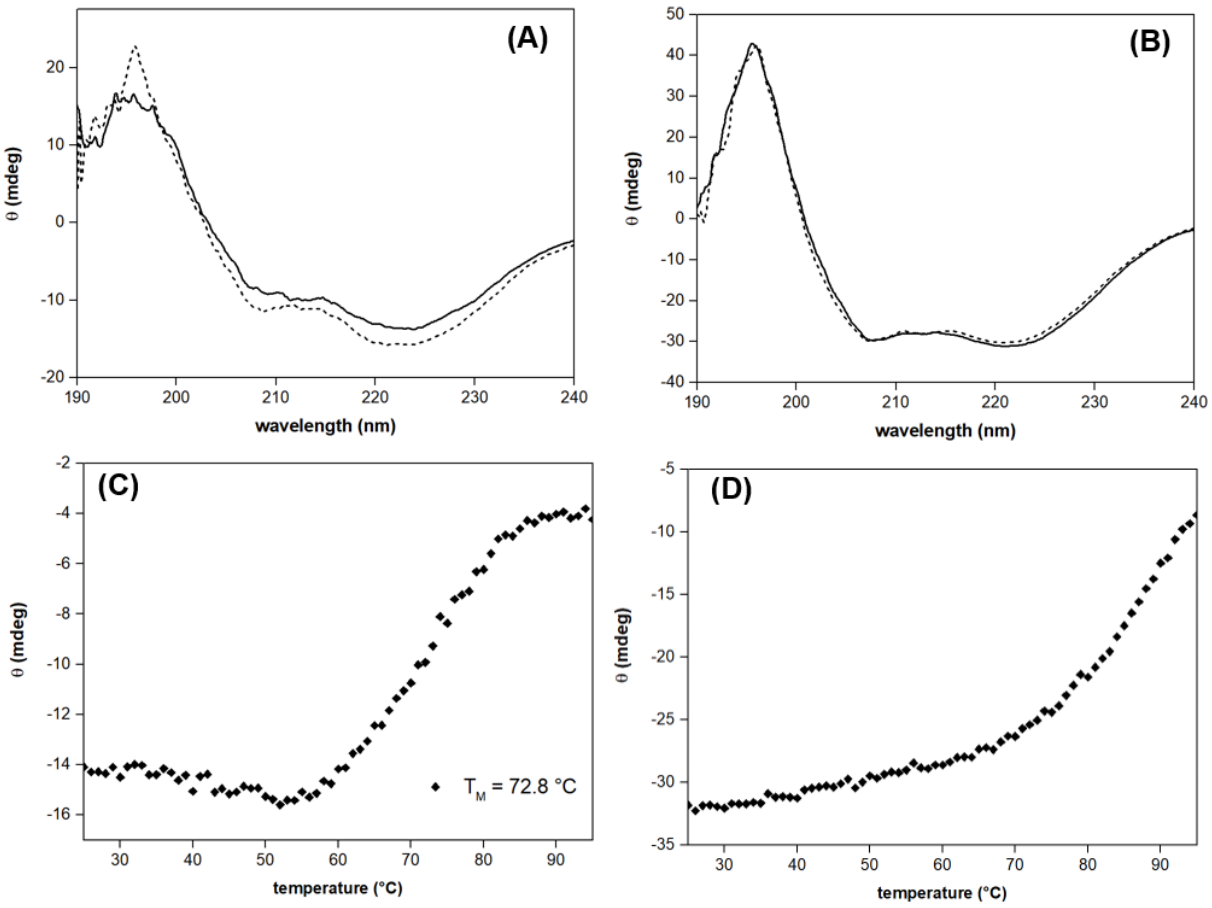

Figure 4.32. CD studies under acidic conditions. CD spectra for at 25 °C for (**A**) RF011 and (**B**) RF012 at pH 3.4. Thermal denaturation curves at pH 3.4 for (**C**) RF011 (**C**) and (**D**) RF012. Conditions: 0.1 mM peptide in 50 mM sodium citrate buffer pH 3.4. Denaturation from 25 to 95 °C at 3 °C min^{-1}. CD after solution preparation (solid trace) and after the thermal denaturation experiment (dashed trace).

In this project, the influence of hydrophobicity and packing within the hydrophobic core of a self-assembly coiled-coil peptide was studied by microscopic and spectroscopic techniques. To this end, the new peptides variants RF011, with three trifluorinated amino acids per helix, and RF012, with four isoleucine residues per helix, were synthesized. CD spectroscopy and infrared spectroscopy provided good evidence that an α-helical folding conformation is conserved independently on the pH conditions. Mimicking the first-generation analogue, under physiological conditions, both peptides assembled into striated rods. Here, fluorination and differences in the packing of the mutated residues within the helical core did not have a significant impact in the assembly. Thus, it seems evident that propensity of the peptide to assemble into large aspect ratio structures dependent on aromatic stacking between adjacent Cy5 moieties.

When buffered under acidic conditions no membrane structures were observed for either RF011 or RF012. In the case of RF011, the disruption of aggregation upon fluorination of the hydrophobic core was likely a consequence of fluorine in the pK_a of the surrounding acidic and basic functionalities, as it decreases the basicity of adjacent amino groups and the acidity of adjacent carboxy moieties.[133,238] In particular, the possible favourable cation-π interactions between the lysine side chains and the aromatic Cy5 can be greatly affected by decreasing the basic behaviour of the amino functionality. In contrast, the self-assembly behaviour of RF012 is not clear and more data is needed to elucidate the differences observed by TEM and AFM. Under acidic conditions RF01 and RF012 showed a very similar behaviour with the predominance of α-helical conformation and the apparent high melting thermal transition. In either case, both leucine and isoleucine residues are not expected to have an influence in the acid-basic behaviour of adjacent atoms. The major anticipated consequence of leucine to isoleucine mutations resides in the accommodation of the side chains, since the only difference is the position of the branching (leucine is γ-branched whereas isoleucine is β-branched). Thus, it is conceivable that a less optimal packing of the isoleucine side-chains within the peptide helix might have fundamental effect on the supramolecular morphology and stability.

4.4. Influence of solvent exposed positions

As discussed on **Section 2.2.1**, positions ***b***, ***c*** and ***f*** – the most solvent exposed positions on the coiled-coil folding motif – are considered to have less influence over peptide stability and folding. They are more permissive to substitutions and, for example, to the incorporation of epitopes or different chemical moieties.[239]

On a fourth design reiteration, the influence of the solvent exposed positions of the coiled-coil motif on the secondary structure and thermal stability were investigated (**Figure 4.33**).

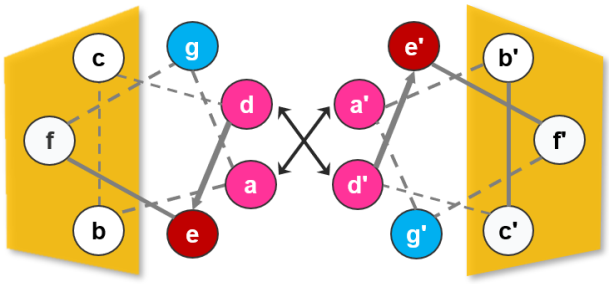

Figure 4.33. Helical wheel representation of the coiled-coil motif where positions *a*, *d*, *e* and *g* were preserved from the original scaffold design (RF01) and only positions *b*, *c* and *f* were modified.

Six new peptides were synthesized following the previously described design rules for the formation of α-helical bundles. The amino acids in positions ***a***, ***d***, ***e*** and ***g*** were preserved from the original peptide (RF01), and only the most solvent exposed positions were substituted (**Table 4.3**). For the new peptide library, the uncharged and apolar Ala was introduced on peptides RF013-RF015 and RF018 primarily with the goal to alter the overall net charge of the peptides. However, Ala can further promote weak interhelical hydrophobic interactions,[80] and increase the overall helical propensity[240,241]. On peptides RF016 and RF017, the charged residues placed at position ***f*** were the same charge to those at positions ***e*** or ***g***, respectively, to interrupt the distribution of positively and negatively charged amino acids. For all peptides, a chromophore (Abz) was coupled to the *N*-terminus and the *C*-terminus was kept unprotected. This new peptide library can be divided in two groups: peptides RF013-RF015, where positions ***b*** and/ or ***c*** were substituted, and peptides

RF016-RF018, where only positions ***f*** were substituted. **Figure 4.34** shows the electrostatic surface map of each coiled-coil peptide. These surfaces were determined using a simple Coulomb's law approach and only intended for qualitative interpretation. **Table 4.3** summarizes the sequences of the six peptides used in this study.

Table 4.3. Sequences of the fourth-generation peptides.

Peptide[a]	*defg*	*abcdefg*	*abcdefg*	*abcdefg*	*abcd*	Charge[b]	pI[c]
RF013	LKSE	LKELKSE	L**AA**LKSE	L**AA**LKSE	L**AA**L	0	6.31
RF014	LKSE	LK**A**LKSE	L**A**KLKSE	LK**A**LKSE	LK**A**L	+4	10.3
RF015	LKSE	L**A**ELKSE	LE**A**LKSE	L**A**ELKSE	L**A**EL	-4	4.22
RF016	LK**K**E	LKELK**K**E	LEKLK**K**E	LKELK**K**E	LKEL	+4	10.0
RF017	LK**E**E	LKELK**E**E	LEKLK**E**E	LKELK**E**E	LKEL	-4	4.51
RF018	LK**A**E	LKELK**A**E	LEKLK**A**E	LKELK**A**E	LKEL	0	6.41

[a]For all peptides, the *N*-terminal is Abz-protected. [b]Overall net charge at pH 7.4. [c]Theoretical isoelectric point calculated with a iterative Grimsley according to Audain *et al*.[198]

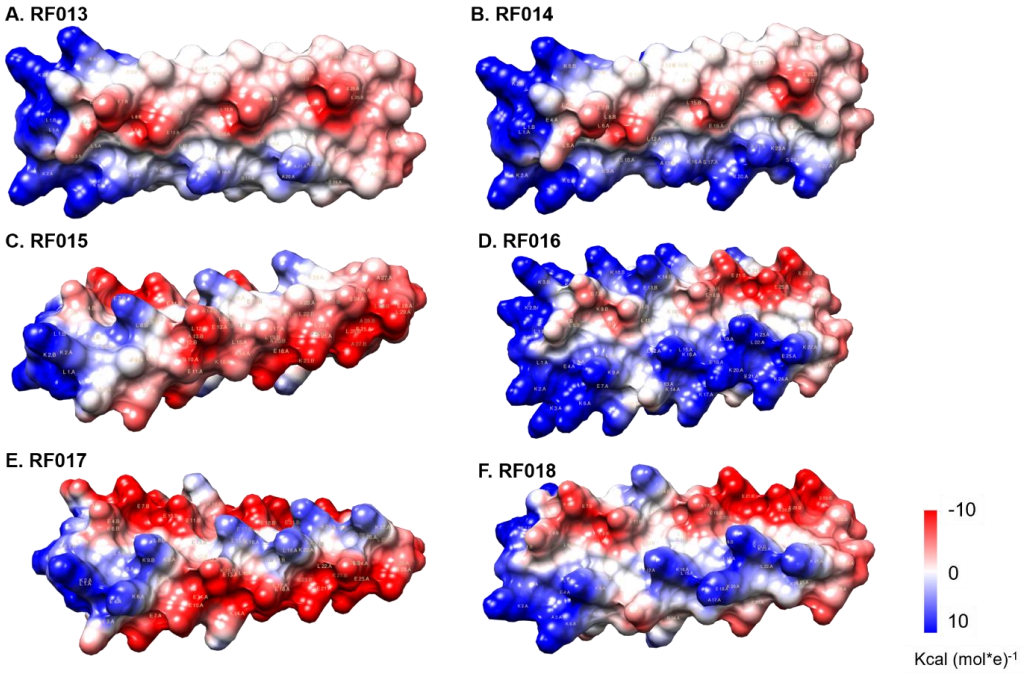

Figure 4.34. Electrostatic surface of peptides RF013-RF018 under neutral pH. (**A**) RF013, (**B**) RF014, (**C**) RF015, (**D**) RF016, (**E**) RF017, and (**F**) RF018. Coiled-coils represented from right to left as *N*- to *C*-terminus. Positive (blue), neutral (white) and negative (red). Coiled-coils build with CCBuilder 2.0.[242] Coulombic map and rendering performed with UCSF Chimera.[41]

The secondary structure of the peptides under neutral pH was analysed by CD. As previously, peptide conformation was studied after solution preparation and then again after thermal refolding. **Figure 4.35** shows the CD profile for each peptide before and after refolding and **Table 4.4** summarizes the CD data. Under the initial conditions, all peptides show predominance of α-helical conformation, as observed by the two minima around 208 and 222 nm. The higher intensity at 222 nm reveals that the neutral peptides RF013 and RF018 have a higher helical content. With the exception of RF018, all peptides regain an α-helical conformation after thermal denaturation experiments with increase on the helical content. RF018 shows a broad minimum at 213.5 nm and a maximum at 192 nm, which deviates from the typical signature for α-helical and closely matches the expected for β-sheet conformation. Thus, for this peptide, a mixture between α-helical and β-sheet conformation or a blue-shifted β-sheet motif might exist. RF016 has a very similar behaviour as the first-generation RF01 peptide, with a low helical content under initial conditions that significantly increases after thermal denaturation experiments, and the pronounced minimum at 222 nm that points to the formation of higher-order helical aggregates.[60] However, in this case no precipitate was observed.

The conformational stability of the peptides was determined by monitoring the ellipticity at 222 nm from 20 to 95 °C and from 95 to 20 °C (at a rate of 3 °C min^{-1}). The denaturation and renaturation curves are shown in **Figure 4.36** and the apparent melting temperatures (T_M) on **Table 4.4**. From this peptide library, only RF013-RF015 and RF017 show an apparent transition from helical to unordered conformation with increasing temperature. The contribution for thermal stabilization is dependent on the amino acid composition and overall net charge. That is, a higher content of negative charged amino acids (RF015 and RF017) results in a greater destabilization of the peptides. This result corroborates the previous observations that glutamate contributes unfavourably for peptide stability. As demonstrated by RF013 and RF014, increasing the hydrophobic character at the *C*-terminus, by substitution of either lysine or glutamic acid with alanine, results in higher stabilization of the peptides.

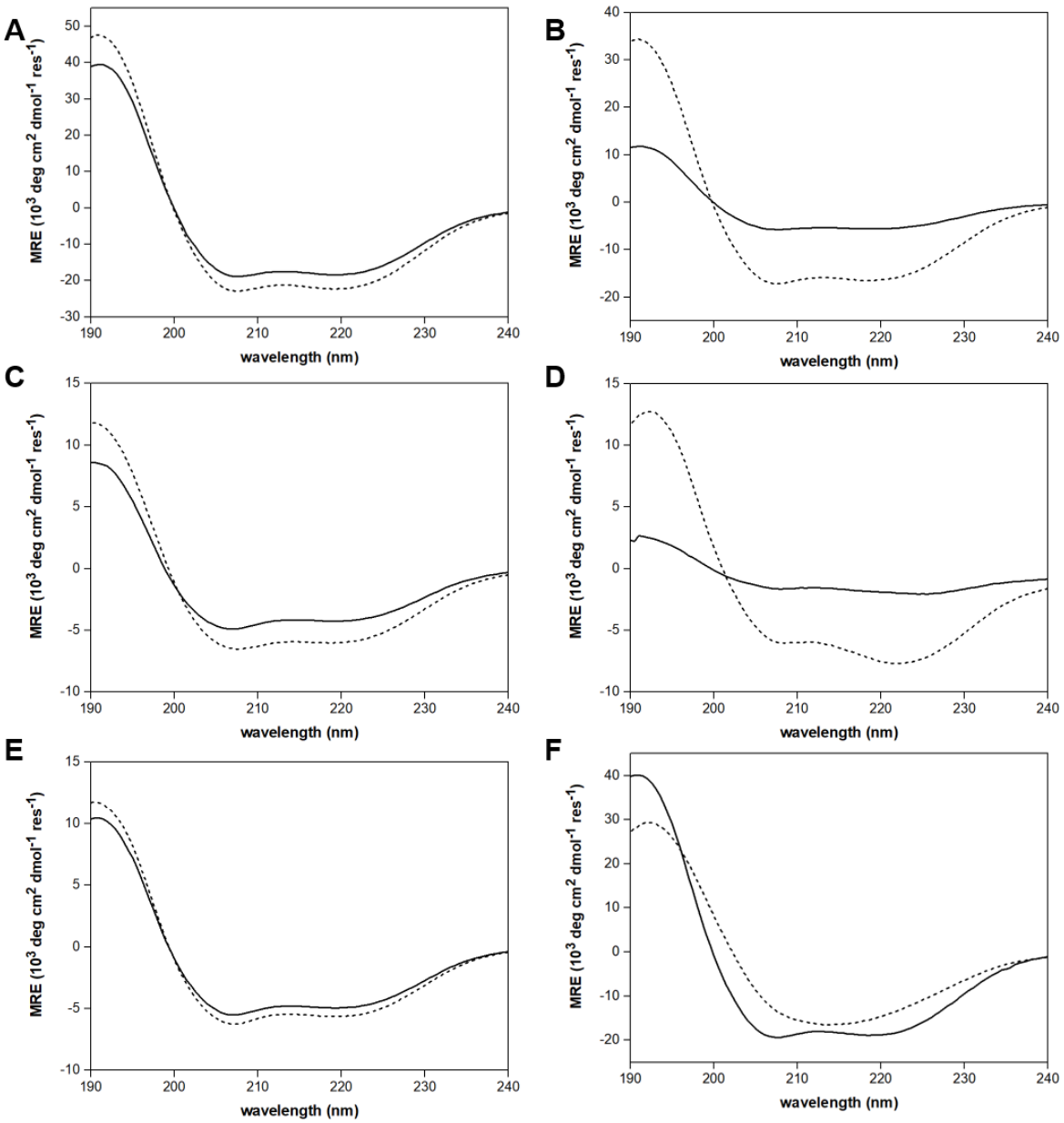

Figure 4.35. CD studies of peptides RF013-RF018 under neutral pH. (**A**) RF013, (**B**) RF014, (**C**) RF015, (**D**) RF016, (**E**) RF017, and (**F**) RF018. Conditions: 0.1 mM peptide in 50 mM phosphate buffer, pH 7.4 at 20 °C. CD after solution preparation (solid trace), CD after refolding (dashed trace).

Analogous to RF01, RF016 exhibited little variation of ellipticity with temperature (**Figure 4.36 D**). Upon annealing, the dynode voltage showed a slight 5 V increase at 70 °C suggesting formation of aggregates might occur upon cooling the solution. However, there was no macroscopic evidence of aggregation. A second melting experiment was performed on RF016, but again only a slight change to

temperatures up to 95 °C was observed (data not shown). This contrasts with RF01, where in a second experiment a clear transition was observed (**Section 4.1**).

RF018 shows a peculiar behaviour: an unexpected increase of ellipticity and dynode voltage for temperatures above 85 °C, and an undisturbed refolding curve. Thus, as supported by the CD spectra in **Figure 4.35 F**, it is conceivable that a temperature inducted β-sheet conformation occurs for this peptide.

Inspired by the work of Banwell *et al*. (**Section 2.2.3**),[80] the ability to form self-supporting gels was inspected by preparing 1 %wt solutions in phosphate buffer at pH 7.4. To test hydrogelation, solutions of thermally annealed peptides and without any thermal treatment were allowed to incubate for 30 min at 25 °C; after this period of time, the vials were inverted and further incubated for an extra 30 min at 25 °C. However, no evidence of self-supporting networks was observed by either peptide.

Table 4.4. Summary of the CD data for RF013-RF018.

	MRE_{222nm} [a]		Helicity (%)[b]		MRE_{222nm} / MRE_{208nm}		
Peptide	**initial**	**refolded**	**initial**	**refolded**	**initial**	**refolded**	**T_M (°C)[c]**
RF013	-17.907	-21.691	53	64	1.1	0.95	61.0
RF014	-16.282	-15.816	48	47	0.95	0.92	69.0
RF015	-12.379	-5.8224	37	17	0.86	0.90	42.4
RF016	-1.9765	-7.6820	6.0	23	1.2	1.3	n.d.
RF017	-14.437	-16.482	43	49	0.88	0.89	55.1
RF018	-18.243	---	54	---	0.94	---	n.d.

[a]In 10^3 deg cm^2 $dmol^{-1}$ res^{-1}. [b]The fraction of helicity was calculated as the ratio between the MRE at 222 nm and the predicted molar ellipticity for a 30-residue long peptide (29 amino acids plus chromophore) according to the equation on **Section 6.3.3**. The predicted MRE value was -33.866 10^3 deg cm^2 $dmol^{-1}$ res^{-1}. [c]The melting temperature was obtained as the maximum value of the first derivative of the melting curve.

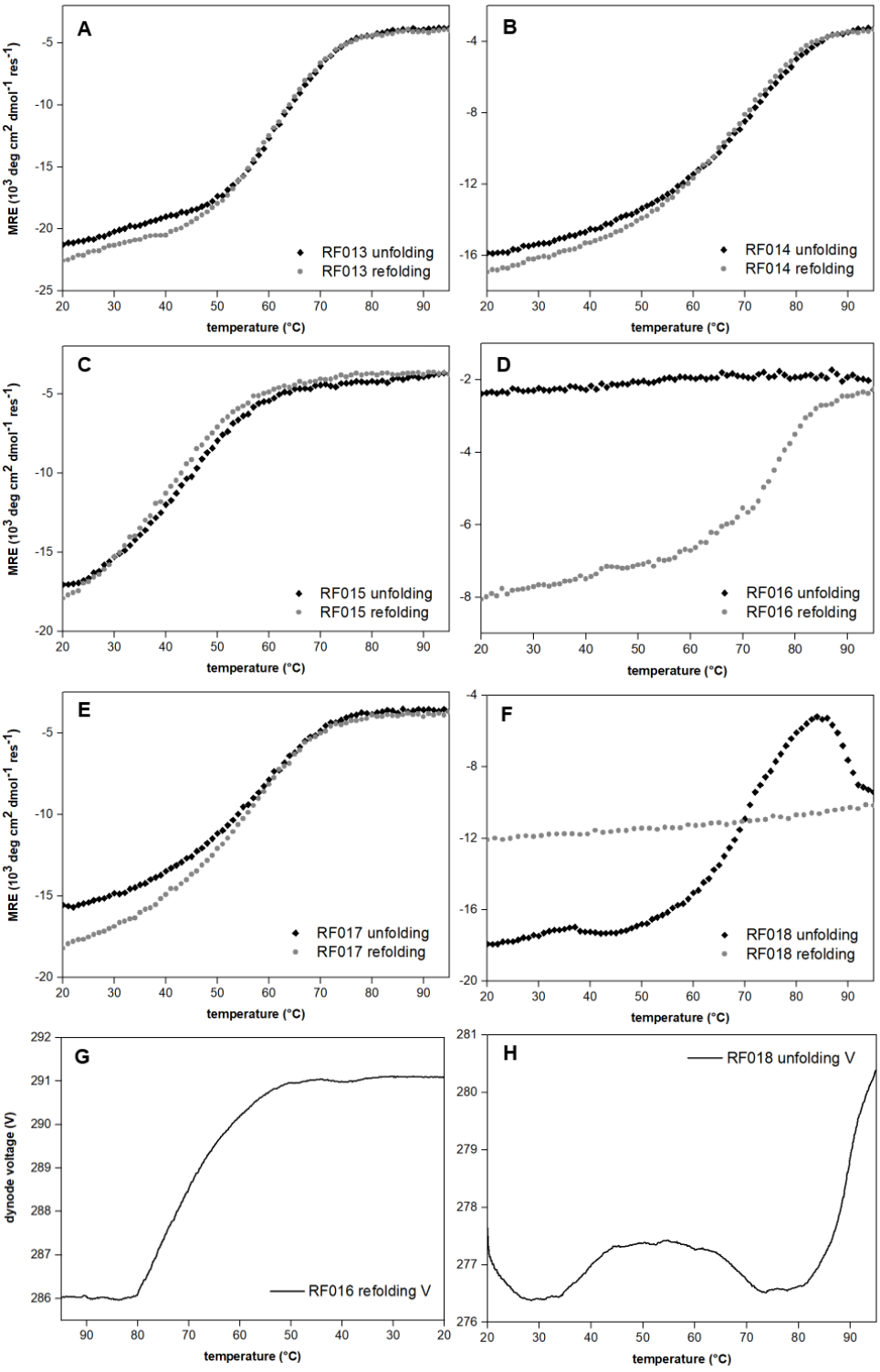

Figure 4.36. Thermal unfolding and refolding spectra for RF013-RF018 under neutral conditions. **A.** RF013. **B.** RF014. **C.** RF015. **D.** RF016. **E.** RF017. **F.** RF018. **G.** Dynode voltage as a function of temperature for the refolding of RF016. **H.** Dynode voltage as a function of temperature for the unfolding of RF018. Conditions: 0.1 mM peptide in 50 mM phosphate buffer, pH 7.4. Unfolding from 20 to 95 °C followed by refolding from 95 to 20 °C (at a rate of 3 °C min^{-1}). Unfolding (black squares), refolding (grey circles).

In this project, the first-generation peptide was redesigned to probe the influence of electrostatic interactions on positions ***b***, ***c*** and ***f***. The CD spectra in **Figure 4.35** indicates that reduction on the content of either acidic or basic amino acids does not have significant influence over the secondary conformation, however a higher helical content is favoured when the peptide exhibits a more neutral overall net charge. In agreement with previous projects in this thesis, the high glutamic acid content leads to thermal destabilization. The denaturation curves in **Figure 4.36** show that expanding of the hydrophobic interface in the *C*-terminus resulted in gain on thermal stability. From the library, RF016 shows a very similar behaviour as for the first generation RF01 peptide with an increase on the helical content after thermal denaturation experiments, and a CD spectrum that points to the formation of aggregation. In the future, it should be interesting to investigates this peptide with microscopic techniques and to conjugate with the same Cy5 derived dye used for RF01 and to study the aggregation behaviour.

4.5. Applications

4.5.1. Fluorinated scaffold for ^{19}F MRI

Multiple sclerosis (MS) is a demyelinating immune disease affecting the human central nervous system (CNS),[243] and the most common neuro inflammatory disease in young adults with a 10 % occurrence increase between 1990 and 2016.[244] Despite its underlying mechanisms are still unclear, it's generally accepted that MS onset involves the recruitment of autoimmune cells to the brain and spinal cord with progressive demyelination, culminating in axonal damage and neurological problems.[243–247] Therefore, tracking of immune cells into the CNS can provide valuable insights on disease onset and progression. In this context, Waiczies *et al*. described the use of fluorescent tagged ^{19}F nanoparticles for the *in vivo* tracking of immune cells to the CNS during neuroinflammation in experimental autoimmune encephalomyelitis (EAE).[185]

Herein, the fluorinated peptide RF011 described in **Section 4.3** was used as candidate system for tracking activated myelin oligodendrocyte glycoprotein (MOG)-specific T cells by ^{19}F MRI. MOGs are highly conserved glycoproteins expressed in the CNS of mammals and are known to induce a demyelinating immune response in EAE.[248–250] Experiments were performed using one sample containing the supramolecular striated rods (thermal treated) and a sample that was not subjected to high temperatures, i.e., only ill-defined structures were formed. However, these experiments were made early in the time of this thesis and little information was available about peptide and dye behaviour in different conditions.

The initial experiments involved the identification of the ^{19}F NMR peak using single voxel **P**oint-**RES**olved **S**pectroscopy (PRESS) (**Figure 4.37 A**). It was found that the peptides immediate environment influences the ^{19}F NMR signal. That is, only a ^{19}F signal was observed for the unheated solution whereas no signal was observed for solution containing the supramolecular structures.

(A)

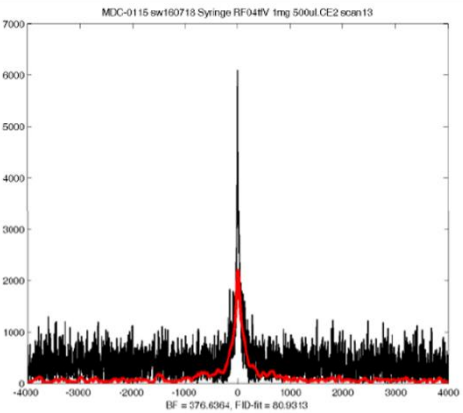

(B)

	T1 (ms)	T2 (ms)
Day 2	2121	294
Day 3	2453	285

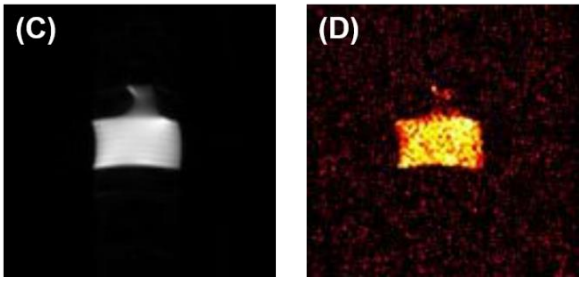

Figure 4.37. ^{19}F measurements. (**A**) Identification of ^{19}F peak using PRESS; (**B**) measured T1 and T2 relaxation times 2 and 3 days after sample preparation; (**C**) proton imaging (^{1}H TurboRARE), TR = 2500 ms, TE = 6.6536 ms, TA = 25 s; (**C**) fluorine imaging (^{19}F TurboRARE), TR = 2500 ms, TE = 6.6536 ms, TA = 1 h 23 min 20 s. TR: repetition time, TE: echo time and TA: acquisition time.

T1 and T2 values were measured over a period of two and three days after solution preparation only for the unheated solution (**Figure 4.37 B**). The obtained T1 values were considerable long. For comparison, using PRESS technique, Ethofer *et al*. obtained a T1 of 1470 ± 80 ms using a 3 T coil when imaging brain's grey matter.[251] Therefore, the results here obtained are an indicator of potential long and difficult *in vivo* spectral and imaging experiments.

Despite the long relaxation times, RF011s ability to penetrate cells was studied by incubating thermally treated and untreated solutions with activated MOG-specific T cells derived from mouse. Upon incubation, the cells were fixed in glutaraldehyde for electron microscopy and ^{19}F MR. Unfortunately, the absence of ^{19}F peak within the expected frequency and the lack of evidence of cellular uptake indicated that neither heated nor non-heated peptide were able to penetrate the cells.

In conclusion, despite measurable relaxation times were achieved using the untreated solution, they were found to be considerably long. However, since relaxation times can change when measured *in vivo*, the peptide presented here provides a good starting point for the development of new peptide-based fluorinated scaffolds. To this end, a first approach is to redesign RF011 in order to increase its solubility. This can be achieved either by the substitution of the Cy5 with a different

fluorescent dye, or by increasing the content of basic residues (lysine or arginine) by the substitution of either glutamate or serine.

4.5.2. Probing the catalytic activity of the supramolecular aggregates

Designing artificial constructs that mimic the defined structural environment of enzymes still remains a considerable challenge. Among different approaches, peptides are promising scaffolds to create such artificial catalytically active systems.[252,253] The main reason is based on the similarities between enzymes and proteins: in both cases, noncovalent interactions govern the folding and self-assembly into well-defined three-dimensional structures that are crucial for their ability to perform their functions.

As mentioned on **Section 2.2.3**, Mikolajczak *et al.* have recently developed peptide-gold nanoparticle conjugates as efficient esterase mimics using general acid/base catalysis enabled by a histidine moiety.[105] This system shares some features with the rods formed by RF01 as both are solid supports with high peptide density. Therefore, to test if catalytic activity could be introduced into the herein reported rods, RF01 was redesigned to feature a histidine in its sequence (RF01H17) in order to generate general acid/base mechanisms. To this end, position number 17 of the original sequence was chosen for the substitution because it is placed in a solvent exposed and central region of the α-helix, with at least one and a half heptad repeat distance from either termini, hence minimizing any possible effect from these regions (**Figure 4.38**). In addition, by introducing the histidine residue in this position, favourable *i, i + 4* and *i + 8* interactions to the carboxyl groups of glutamate (essential for charge relay) can occur. The impact of this substitution on RF01H17 conformation and the catalysis of *p*-nitrophenyl acetate (*p*NPA) was analysed by means of CD and UV-vis absorbance.

Prior to the kinetic measurements, the secondary conformation and thermal stability under pH 7.4 were analysed by CD. As expected, this new variant showed a very similar behaviour as RF01. That is, upon thermal denaturation a significant increase in CD intensity and the formation of a fine precipitate was evident. Furthermore, the peptide retained its α-helical conformation as observed with characteristic double minima around 208 and 222 nm (**Figure 4.38**, dashed trace). Following the same protocol, the thermal stability of the peptides was determined by monitoring the ellipticity at 222 nm from 20 to 95 °C and from 95 to 20 °C (at a rate of 3 °C min^{-1}). Conversely to RF01, no significant variation of ellipticity was observed for either a first or a second thermal denaturation experiment, indicating a high thermal stability of RF01H17.

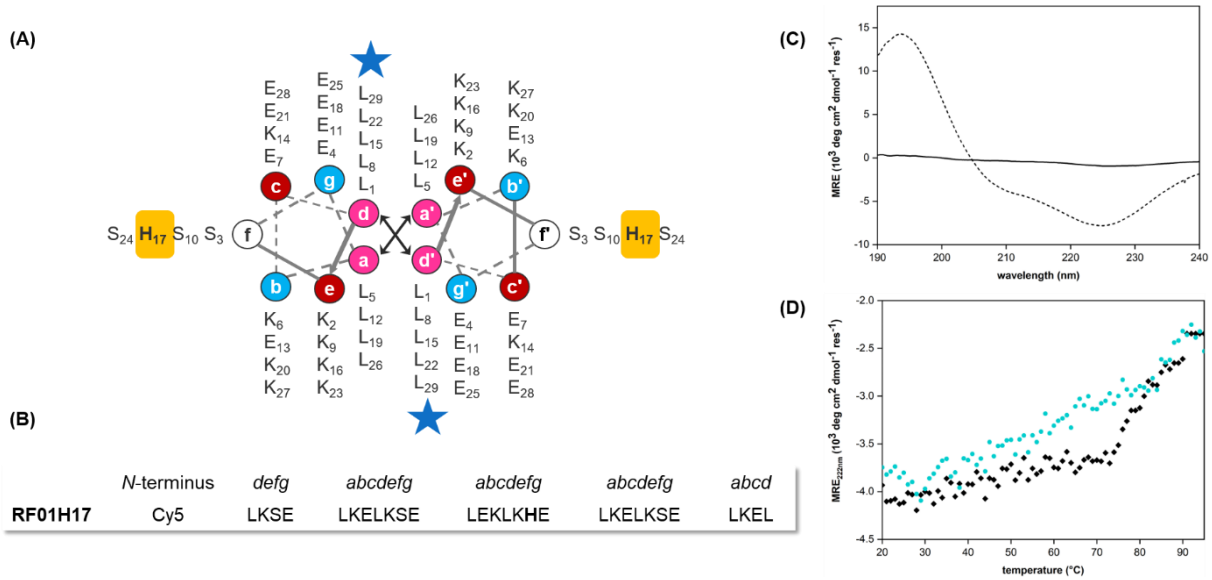

	N-terminus	*defg*	*abcdefg*	*abcdefg*	*abcdefg*	*abcd*
RF01H17	Cy5	LKSE	LKELKSE	LEKLK**H**E	LKELKSE	LKEL

Figure 4.38. Design and sequence of RF01H17 and CD analysis. (**A**) Helical wheel representation of RF01H17 with the histidine residue highlighted in bold and yellow. The blue star represents Cy5-derivative. (**B**) Linear sequence of RF01H17. The *C*-terminus is free. (**C**) CD analysis at pH 7.4 after solution preparation (solid trace) and after the thermal denaturation experiment (dashed trace). (**D**) First (black squares) and second (blue circles) thermal denaturation curves from 20 to 95 °C. Conditions: 0.1 mM peptide in 50 mM phosphate buffer pH 7.4.

The effect of RF01H17-mediated hydrolysis of *p*NPA was studied by recording the absorbance at 405 nm. No differences were observed when carrying the reaction in the presence of absence of RF01H17, i.e., no catalysis. While discouraging, the results were not unexpected. That is, although the arrangement of the peptides in the rods is not resolved, it can be assumed that RF01H17 strands are tightly packed throughout the structures, with the hydrophobic surfaces buried away from the aqueous solvent. Therefore, it is likely that the helical arrangement does not allow for favourable interactions between the histidine and the carboxylic acid from glutamate residues (**Figure 4.39**). Thus, in accordance with Mikolajczak *et al.*,[105] requirements for general acid/base catalysis needed for the *p*NPA hydrolysis are not fulfilled.

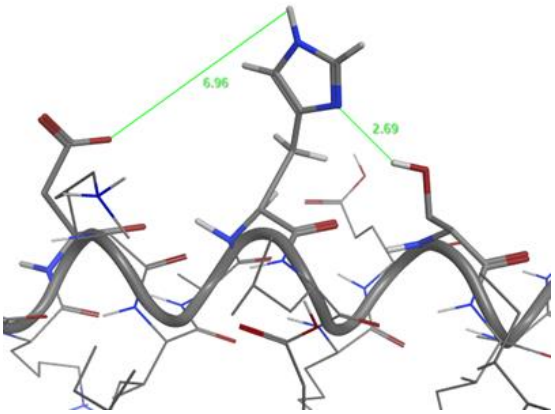

Figure 4.39. Example of inadequate charge-relay between aspartate, histidine and serine in a *i, i + 4* and *i + 8* in a α-helix conformation, proposed by Heier.[254]

5. Summary and Outlook

The growing number of different peptide-based structures has been a concerted effort of several research teams all over the world. However, a deeper understanding of the underlying driving forces and assembly mechanisms is still needed in order to design and to precisely regulate such structures. In this context, the goal of this thesis was to develop supramolecular assemblies based on coiled-coil peptidic scaffolds and to understand their properties.

A simple peptide-dye scaffold (RF01) that exhibited pH-triggered aggregation was first successfully developed. Key design features included the high content of pH responsive amino acids and the conjugation of a Cy5 dye to the *N*-terminus. Under acidic conditions, RF01 self-assembled on standing, with the formation of high aspect ratio membranes. Under neutral conditions and after subjected to thermal annealing, RF01 formed long, unbranched and striated rods. Such defined structures were absent in RF01 solutions buffered under basic pH or in the absence of Cy5. Independent on the formation of either membranes or rods, spectroscopic studies demonstrated that the Cy5 residues were face-to-face stacked within the structures. With this observation, it was proposed that in both cases, assembly was dictated by strong π–π stacking interactions between adjacent Cy5 moieties. In addition, interactions between Cy5 and the different ionizable residues, as well as hydrophobic interactions, salt-bridges and hydrogen bonding further determines the final morphology under the different conditions. However, peptide-dye arrangement within either structure was proved difficult to solve through computational models. Further efforts are currently in progress in order to provide a more detailed understanding of the peptide arrangement and driving forces for aggregation.

With these findings, three questions immediately emerged. First, was the formation of the structures dependent of the dye, or the same results could be obtained using different aromatic moieties. Second, was the peptide scaffold robust to withstand multiple mutations within the hydrophobic core without significant disturbance of conformation or the propensity to aggregate. Third, what was the role of solvent exposed positions of the coiled-coil motif, usually considered as less crucial for peptide folding and stability.

To tackle these questions a series of peptide redesigns were performed. In Part 2, the role of the residue attached to the *N*-terminus was examined by substituting the Cy5 moiety with different *N*-protected tryptophan residues or with the commonly used Fmoc-protection group. The results demonstrated that the presence of Cy5 was in fact crucial for the self-assembly into membranes and rods. The new peptides showed self-assembly, but the results suggest that only a compromise between charge, size and hydrophobicity leads to the formation of well-defined structures. Namely, a free and charged *N*-terminus was found to be destabilizing and unfavourable for peptide aggregation. Sensitivity towards acidic pH was shown to decrease in the presence of a more hydrophobic and steric constrained *N*-terminus, i.e., the more hydrophobic peptide was able to self-assemble independently under acidic or neutral pH.

Aiming to increase peptide stability without disturbance of the self-assembly, Part 3 reports on the substitution of multiple leucine residues in ***a*** positions within the helical core with trifluorovaline (4^3-F_3V) and isoleucine. The collected data showed that the secondary conformation was not disturbed by the multiple substitutions, but the stability and propensity to assemble was dependent of the nature of the mutated residues. Under neutral conditions, both variants assembled into striated rods, whereas under acidic conditions no membranes were observed for either peptides. In addition, the isoleucine bearing peptide was more stable than the fluorinated and the original leucine variants. The effect of these substitutions is still not solved, and more structural data is needed. However, the disruption of aggregation for the fluorinated peptide is likely a direct consequence of fluorine in the pK_a of the surrounding acidic and basic functionalities. In contrast, the differences in aggregation of RF01 and the isoleucine variant might be a consequence of a less optimal packing of the isoleucine side-chains within the peptide helices.

On a final design reiteration, the influence of the most solvent exposed positions of the coiled-coil motif was analysed by the systematic substitution with alanine, small and uncharged canonical amino acid. In Part 4, a library of peptides exceeding in positive or negative charge under neutral pH conditions allowed for the comparison to RF01. It was demonstrated that the secondary structure was independent on the content of either acidic or positively amino acids. The results obtained with the melting experiments are in good agreement with the previous observations that

higher thermal stability is achieved by introducing residues that are positively charged under neutral conditions. Future efforts should be made to incorporate the larger aromatic moieties, such as tryptophan, and study its effects on the self-assembly.

Preliminary efforts were made to utilize selected scaffolds for applications. The fluorinated peptide was used as candidate system for tracking activated MOG-specific T cells by ^{19}F MRI. The considerable long relaxation times observed were an indicator of the unfeasibility of this system for further *in vivo* applications. Future work should focus on both the increase of fluorine content and solubility of the peptide scaffold. On a different strategy, RF01 was slightly modified in order to include one histidine for the ester hydrolysis catalysis using the striated rods. Despite no perturbation of the secondary conformation, no catalytical activity was observed. It was proposed that the peptide arrangement within the rods was inadequate for charge-relay interactions between the histidine and the glutamate residues.

Taking together, the peptides presented throughout this thesis expand our knowledge on how natural and *de novo* designed high ordered constructs form, and how they can possible be used in biotechnological applications.

6. Experimental procedures and analytical methods

6.1. Materials and methods

Solvents used for peptide synthesis were obtained 'synthesis grade' Acros Organics (Thermo Fisher Scientific, Geel, Belgium), Fisher Scientific (Schwerte, Germany), Merck (Merck Chemicals GmbH, Darmstadt, Germany) or VWR (VWR International GmbH, Darmstadt, Germany). Water used for HPLC and to prepare buffers was obtained using a Milli-Q® Advantage A10 Ultrapure Water Purification System (Merck KGaA, Darmstadt, Germany). Resins for peptide synthesis were purchased from Novabiochem® (Merck KGaA, Darmstadt, Germany). Fmoc- and orthogonal side chain protected amino acids were obtained from ORPEGEN Peptide Chemicals GmbH (Heidelberg, Germany). Coupling reagents were purchased from Novabiochem® (Merck KGaA, Darmstadt, Germany), Carbolution (Carbolution Chemicals GmbH, St. Ingbert, Germany) or Sigma-Aldrich® (Merck KGaA, Darmstadt, Germany). Other chemicals and solvents were purchased from abcr GmbH (Karlsruhe, Germany), Acros Organics (Thermo Fisher Scientific, Geel, Belgium), Alfa Aesar (Thermo Fisher (Kandel) GmbH, Karlsruhe, Germany), chemPUR (Karlsruhe., Germany), Fluorochem (Hadfield, United Kingdom), Merck (Darmstadt, Germany), Novabiochem® (Merck KGaA, Darmstadt, Germany), Sigma-Aldrich® (Merck KGaA, Darmstadt, Germany), Roth (Carl Roth GmbH + Co. KG, Karlsruhe, Germany), and VWR (Darmstadt, Germany). All reagents and solvents were used without further purification except for acetic anhydride (Grüssing GmbH Analytika, Filsum, Germany) that was freshly distilled prior to use.

6.2. Peptide synthesis and characterization

6.2.1. Solid Phase Peptide Synthesis

All peptides were synthesized by standard solid phase peptide synthesis (SPPS) methods developed by Merrifield (**Figure 6.1**).[255] In SPPS, an amino acid sequence is anchored to an insoluble solid support (resin) by coupling the unprotected *C*-terminal to the resin. Both the *N*-terminus and side chain functionalities are protected while coupling proceeds. The reaction occurs from *C*- to *N*-terminal and involves repetitive deprotection and coupling reactions, with in-between washing

steps. Coupling reaction are performed upon formation of active esters of the incoming amino acid. Since the entire synthesis occurs with the immobilization of the peptide in the resin, removal of solvent and secondary by-products is easily performed by filtration. Upon completion, the peptide is cleaved from the solid supporting under acidic conditions.

A key feature of SPPS is the use of orthogonal protecting groups that can be removed under different conditions. The most commonly used orthogonal strategy – and the strategy used throughout this thesis – uses Fmoc/ t-Bu as protecting groups. In this case, the α-amino group is temporary protected with 9-fluorenylmethoxycarbonyl (Fmoc), which can be easily removed using mild basic conditions. The side chains of trifunctional amino acids are protected with semipermanent tert-butyl groups, which are easily removed using mild acidic conditions.

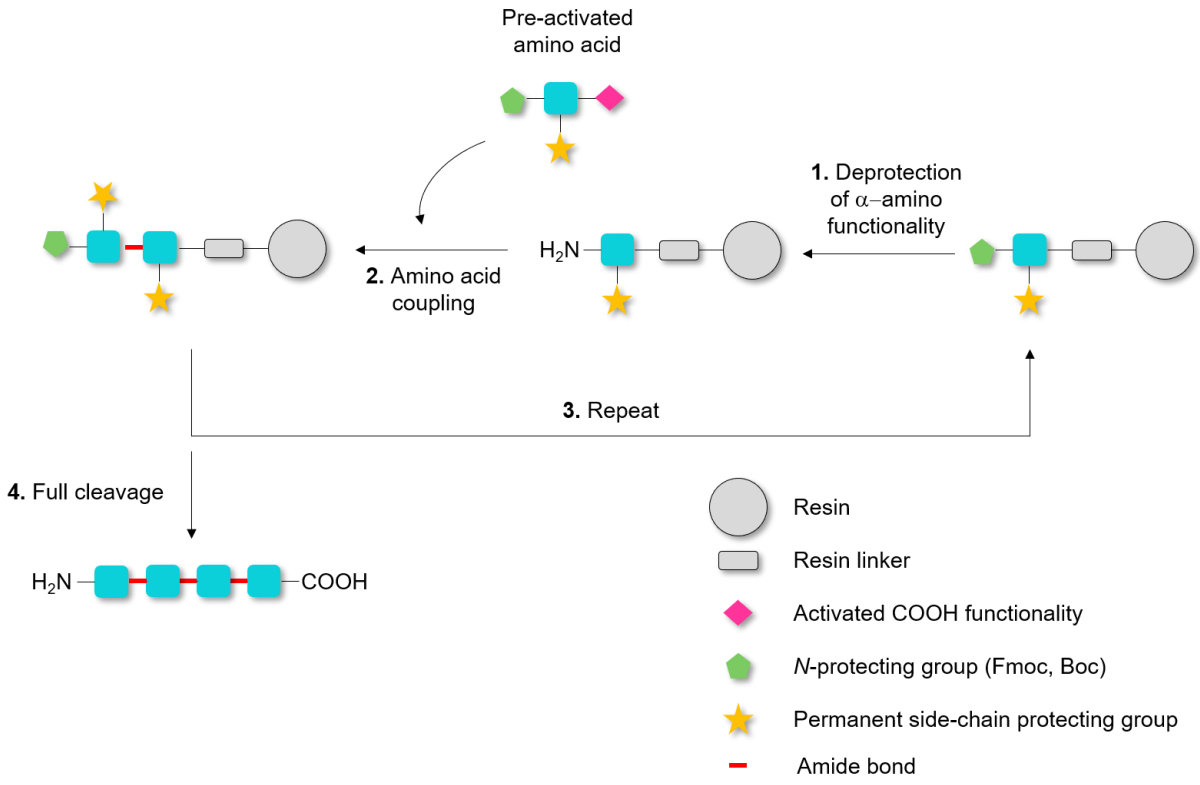

Figure 6.1. Solid phase peptide synthesis procedure scheme.

6.2.2. Fmoc SPPS protocol

Throughout the thesis, peptide synthesis was carried out either manually or automated using a SyroXP (Multi-SynTec GmbH). Both processes were performed using similar protocol. In a polypropylene reaction syringe vessel equipped with a PTFE frit, preloaded resin was allowed to swell in DMF for 20 minutes. Before proceeding, the solvent was pushed out of the syringe. Fmoc was then removed using a 20 % piperidine in DMF solution for 5 min (4x). After thoroughly washing the resin with DMF, amino acid coupling was performed. Different coupling cocktails were used as shown below:

1. Manual synthesis: Fmoc-amino acid (5 eq.) and HOBt (5 eq.) were dissolved in approximately 3 mL DMF. Upon addition of DIC (5 eq.), a 10 min pre-activation step was carried before adding to the resin. The syringe was then agitated for 60 minutes.
2. Automated synthesis: Fmoc-amino acid (5 eq.), HOBt (5 eq.) and TBTU (5 eq.) were dissolved in approximately 3 mL DMF. DIPEA (10 eq.) was then added the solution added to the reactor vessel. The reaction proceeded for 60 minutes.

All amino acids were coupled twice. This process was repeated until the last amino acid of the desire sequence was added. The synthesis protocol is summarized in **Table 6.1**.

Table 6.1. Fmoc-deprotection and coupling protocol using manual and automated synthesis.

Process	Reagents		Time
	Manual	Automated	
1. Swelling of resin	3 mL DMF		20 min
2. Fmoc-deprotection	2 mL 20 % piperidine in DMF		4 x 5 min
3. Washing	2.5 mL DMF		6 x 1 min
4. Amino acid coupling	Fmoc-aa (5 eq.) and HOBt (5 eq.) in DMF; DIC (5 eq.) in NMP with 10 min pre-activation	Fmoc-aa (5 eq.) and HOBt (5 eq.) in DMF; TBTU (5 eq.) in DMF; DIPEA (10 eq.) in NMP	60 min
5. Washing	2.5 mL DMF		1 x 1 min
6. Amino acid coupling	Fmoc-aa (5 eq.) and HOBt (5 eq.) in DMF; DIC (5 eq.) in NMP with 10 min pre-activation	Fmoc-aa (5 eq.) and HOBt (5 eq.) in DMF; TBTU (5 eq.) in DMF; DIPEA (10 eq.) in NMP	60 min
7. Washing	2.5 mL DMF		6 x 1 min

Additional remarks about peptide synthesis procedure:

1. **Coupling of fluorinated amino acids.** The coupled of fluorinated amino acids were performed manually. The molar excess of fluorinated amino acids and coupling reagents were reduced in comparison to the above described protocol. Fmoc-fluorinated amino acid (1.2 eq.) and HOAt (1.2 eq.) were dissolved in DMF. After the addition of DIC (1.2 eq.), a 10 min pre-activation step was carried before adding to the resin. The first coupling step was performed overnight and the second for 60 min. Completion of the reaction was monitored by HPLC.

2. **Coupling of the cyanine dye derivative.** The coupling of the cyanine derivative (DM-IDCC COOH, mivenion, 602200), with a free carboxylic acid was performed three times using 1.5, 0.75 and 0.75 eq. of dye and the same molar excess of coupling reagents.
3. ***N*-terminal acetylation.** After removal of the last Fmoc-protecting group, the peptide was treated with a 10 % freshly distilled solution of acetic anhydride and 10 % DIPEA three times for 10 min.

6.2.3. Peptide cleavage from resin

After successful peptide synthesis, the resin was thoroughly washed in DCM to remove the less volatile DMF.[254] Full cleavage of the peptide was achieved by treating the resin with a solution cocktail containing 95 % TFA, 3 % TIS and 2 % water (with 1 mL solution per 100 mg resin) for 2 h. The solution was collected in a round-bottom flask and the resin was washed with 1 mL TFA and 2 mL DCM. The solution was concentrated under a gentle stream of nitrogen. Crude peptide was precipitated in ice-cold diethyl ether and collected by centrifugation. The remaining solvent was removed from the precipitate using a rotary evaporator.

6.2.4. Synthesized peptides

The peptide sequences are summarized in **Table 6.2**. The abbreviations for the moieties coupled to the *N*-terminus can be found in the previous sections.

Table 6.2. Summary of the peptide sequences described during in this thesis.

Name	Sequence
RF01	cy5-LKSE LKELKSE LEKLKSE LKELKSE LKEL
RF04	WLKSE LKELKSE LEKLKSE LKELKSE LKEL
RF05	fmoc-WLKSE LKELKSE LEKLKSE LKELKSE LKEL
RF06	ac-WLKSE LKELKSE LEKLKSE LKELKSE LKEL
RF08	fmoc-LKSE LKELKSE LEKLKSE LKELKSE LKEL
RF09	LKSE LKELKSE LEKLKSE LKELKSE LKEL
RF011	cy5-LKSE F_3VKELKSE F_3VEKLKSE F_3VKELKSE LKEL
RF012	cy5-LKSE IKELKSE IEKLKSE IKELKSE IKEL
RF013	abz-LKSE LKELKSE LAALKSE LAALKSE LAAL
RF014	abz-LKSE LKALKSE LAKLKSE LKALKSE LKAL
RF015	abz-LKSE LAELKSE LEALKSE LAELKSE LAEL
RF016	abz-LKKE LKELKKE LEKLKKE LKELKKE LKEL
RF017	abz-LKEE LKELKEE LEKLKEE LKELKEE LKEL
RF018	abz-LKAE LKELKAE LEKLKAE LKELKAE LKEL
RF019	cy5-LKSE LKELKSE LEKLKHE LKELKSE LKEL

6.2.5. Peptide purification and analysis

Peptide purification was performed on a semi-preparative LaPrepΣ HPLC system (VWR International GmbH, Darmstadt, Germany). The system was equipped with a LaPrepΣ LP 1200 preparative solvent pump, a low-pressure gradient, an eluent mixing chamber, a LaPrepΣ LP 3101 1-channel UV-detector, a LaPrepΣ semi-preparative flow cell with 0.5 mm path length, an injection valve with a 10 mL sample loop and a LaPrepΣ LP2016 fractionation valve. The column used was a Kinetex® C18 RP-HPLC (5 µm, 100 Å, 250 × 21.2 mm, Phenomenex®, Torrance, CA, USA) equipped with a SecurityGuard™ Prep Cartridge Holder Kit (21.20 mm ID, Ea, Phenomenex®, Torrance, CA, USA) pre-column. Gradients of MilliQ® water and MeCN (each with 0.1% TFA) were used at a rate of 15 mL min^{-1}.

Table 6.3. Methods and retention time for peptide purification.

Peptide	MeCN gradient [a]	rt (min)
RF01	5 to 70 % in 30 min, 20 mL min^{-1}	23.8
RF04	5 min at 5 % 10 mL min^{-1} then 5 to 70 % in 30 min, 20 mL min^{-1}	24.0
RF05	30 to 100 % in 18 min, 15 mL min^{-1}	10.8
RF06	5 to 70 % in 18 min, 20 mL min^{-1}	15.2
RF08	5 to 70 % in 18 min, 20 mL min^{-1}	15.9
RF09	5 to 70 % in 18 min, 20 mL min^{-1}	13.7
RF011	5 min at 5 % 10 mL min^{-1} then 5 to 70 % in 30 min, 20 mL min^{-1}	24.8
RF012	5 to 70 % in 18 min, 20 mL min^{-1}	15.7
RF013	30 to 80 % in 18 min, 15 mL min^{-1}	12.4
RF014	20 to 80 % in 18 min, 15 mL min^{-1}	13.0
RF015	20 to 80 % in 18 min, 15 mL min^{-1}	14.4
RF016	20 to 80 % in 18 min, 15 mL min^{-1}	12.7
RF017	20 to 80 % in 18 min, 15 mL min^{-1}	13.6
RF018	20 to 80 % in 18 min, 15 mL min^{-1}	13.5
RF019	10 to 80 % in 18 min, 15 mL min^{-1}	15.3

[a] MeCN (with 0.1 % TFA), and MilliQ (with 0.1 % TFA). Detection λ at 220 nm. Column: C18. [b] rt = retention time.

Fractions were collected and analysed on a VWR-Hitachi Chromaster HPLC 600 bar (VWR International GmbH, Darmstadt, Germany). This high-pressure HPLC system which allows for the fast (~ 10 min) verification of the purity of each fraction collected by preparative-HPLC. This system was equipped with a 5160 pump, an autosampler with a 20 µL sample loop, a high pressure semi-micro flow cell detector, and a Purospher® STAR RP-C18 endcapped UHPLC column (2 µM, 120 Å, 50 × 2.1 mm, Merck, Deutschland). For purity control, the UV detector was set to 220 nm for all peptides. Furthermore, the *N*-labelled peptides were also analysed at 650 nm for RF01, RF011 and RF012; 320 nm for RF02 and RF013-RF018; 280 nm for RF04-08 and RF010. Gradients of MilliQ® water and MeCN (each with 0.1% TFA) were used at a rate of 0.6 mL min^{-1}.

The fractions showing the same retention time and high purity were collected for a final quality assessment in a LaChrom Elite-HPLC-System (VWR International GmbH, Darmstadt, Germany) equipped with two L-2130 pumps, diode array detector L-2485, autosampler L-2200 with 100 µL sample loop, solvent degasser L-7612, and a Kinetex® C18 column (5 µm, 100 Å, 250 × 4.6 mm, Phenomenex®, Torrance, CA, USA). For purity control, the UV detector was set to 220 nm for all peptides. Furthermore, the *N*-labelled peptides were also analysed at 650 nm for RF01, RF011 and RF012; 320 nm for RF02 and RF013-RF018; 280 nm for RF04-08 and RF010. Gradients of MilliQ® water and MeCN (each with 0.1% TFA) were used at a rate of 1.0 mL min^{-1}. All HPLC data was analysed using EZChrom Elite software.

Following purification, the peptides were lyophilized using an α 1-2 LD freeze dryer (Christ Gefriertrocknungsanlagen GmbH, Osterode am Harz, Germany) and stored at - 23 °C.

Peptides were identified by electrospray ionization – time of flight mass spectrometer (ESI-ToF MS) using an Agilent 6210 ESI-ToF LC-MS spectrometer (Agilent Technologies Inc., Santa Clara, CA, USA) with manual sample injection via a syringe pump (Harvard Apparatus 11 Plus) at a flow rate of 0.2 mL/min.

6.2.6. Peptide identification by analytical HPLC and mass spectrometry

The analysis data for each peptide are summarized in **Table 6.4**.

Table 6.4. Gradient and retention times obtained by analytical HPLC and monoisotopic mass obtained by ESI-TOF for each peptide described in this thesis .

Peptide	Analytical HPLC		ESI-TOF	
	MeCN gradient[a]	rt (min) [b]	Calculated	Observed
RF01	5–100 in 18 min	14.8	$[M+3H]^{3+}$: 1284.7517	$M+3H]^{3+}$: 1284.7532
RF04	5–100 in 18 min	13.9	$[M+3H]^{3+}$: 1210.0319	$[M+3H]^{3+}$: 1210.0372
RF05	5–100 in 18 min	15.1	$[M+3H]^{3+}$: 1284.0546	$[M+3H]^{3+}$: 1284.0594
RF06	5–100 in 18 min	14.0	$[M+3H]^{3+}$: 1224.0354	$[M+3H]^{3+}$: 1224.0406
RF08	5–100 in 18 min	14.4	$[M+3H]^{3+}$: 1222.0282	$[M+3H]^{3+}$: 1222.0353
RF09	5–100 in 20 min	13.8	$[M+3H]^{3+}$: 1148.0055	$[M+3H]^{3+}$: 1148.0088
RF011	30–100 in 18 min	9.15	$[M+3H]^{3+}$: 1324.7047	$[M+3H]^{3+}$: 1324.6992
RF012	30–100 in 18 min	9.13	$[M+3H]^{3+}$: 1284.7517	$[M+3H]^{3+}$: 1284.7538
RF013	5–100 in 30 min	20.2	$[M+3H]^{3+}$: 1072.9574	$[M+3H]^{3+}$: 1072.9595
RF014	10–80 in 30 min	21.3	$[M+3H]^{3+}$: 1110.6801	$[M+3H]^{3+}$: 1111.0114
RF015	10–80 in 30 min	23.3	$[M+3H]^{3+}$: 1111.9442	$[M+3H]^{3+}$: 1111.9436
RF016	10–80 in 30 min	20.7	$[M+3H]^{3+}$: 1242.7719	$[M+3H]^{3+}$: 1242.9610
RF017	10–80 in 30 min	21.6	$[M+3H]^{3+}$: 1244.0353	$[M+3H]^{3+}$: 1244.2290
RF018	10–80 in 30 min	21.6	$[M+3H]^{3+}$: 1166.6948	$[M+3H]^{3+}$: 1166.9733
RF019	5-100 in 18 min	14.8	$[M+3H]^{3+}$: 1301.4273	$[M+3H]^{3+}$: 1301.4279

[a] MeCN (with 0.1 % TFA), and MilliQ (with 0.1 % TFA). Flow rate of 1 mL min^{-1}. Column: C18. [b] rt = retention time.

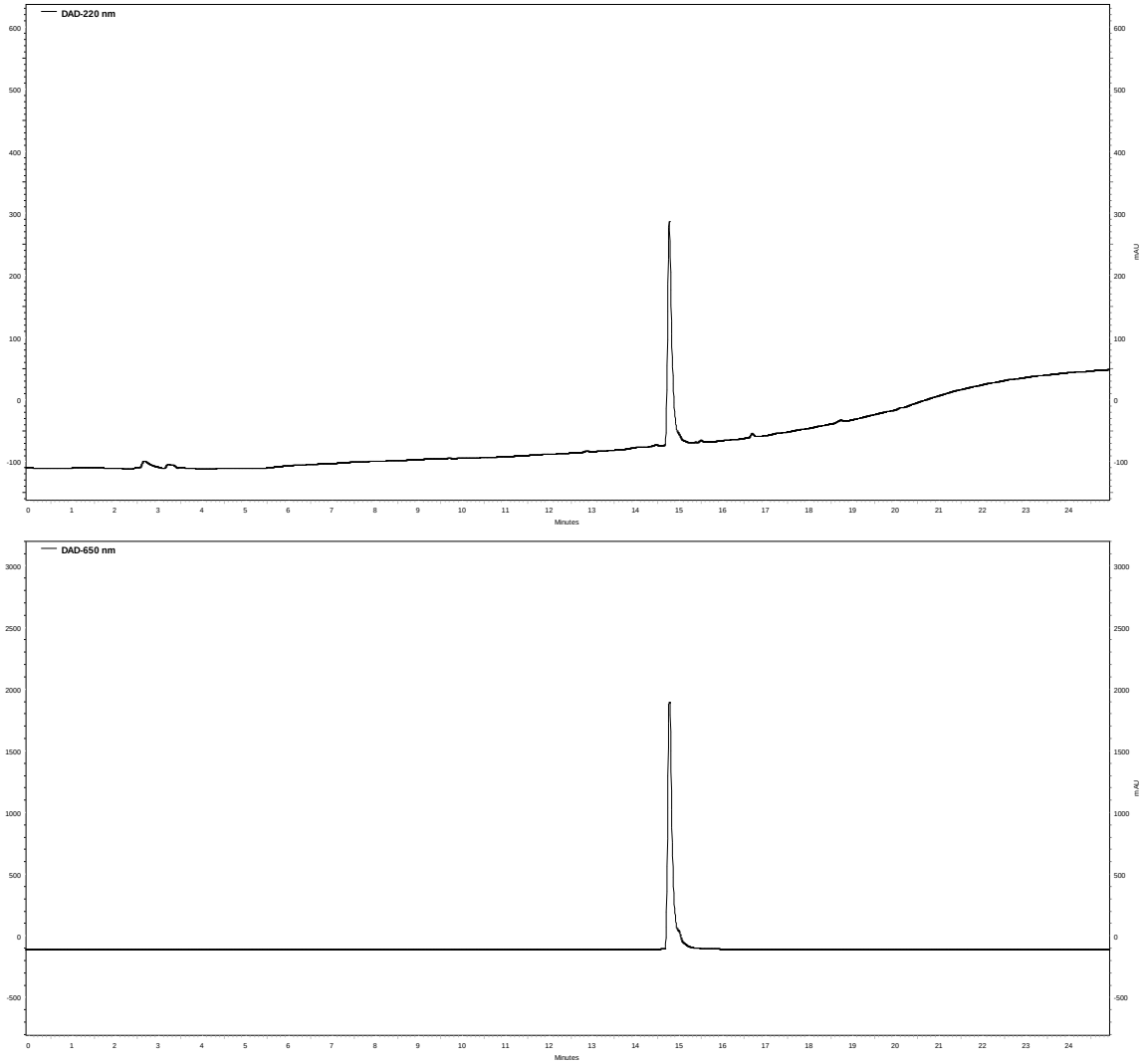

Figure 6.2. HPLC chromatogram of RF01. The upper panel shows chromatogram at 220 nm and bottom panel at 650 nm in 5 – 100 MeCN (with 0.1 % TFA) in 18 min, 1 mL min^{-1}.

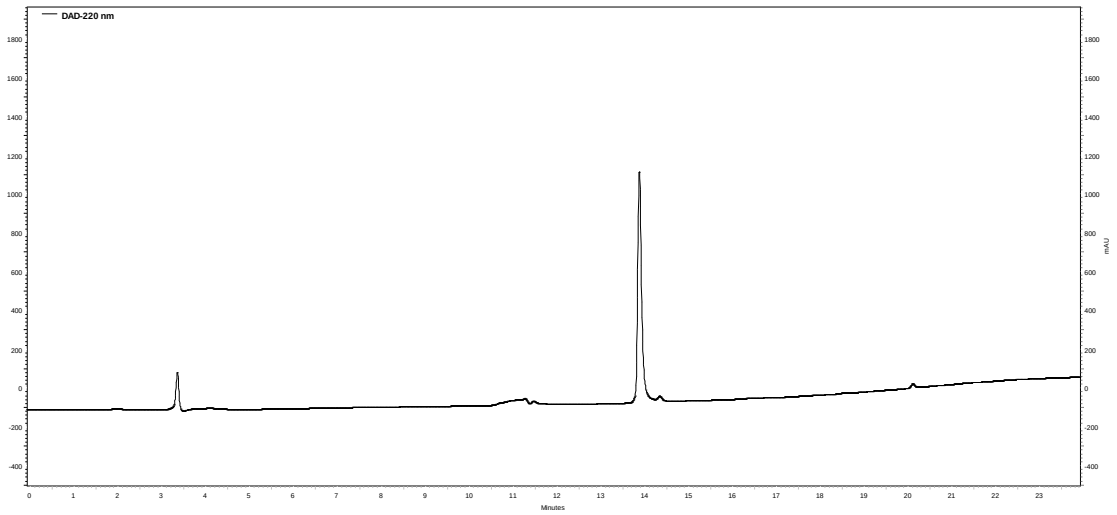

Figure 6.3. HPLC chromatogram of RF04. Chromatogram at 220 nm. Gradient: 5 – 100 MeCN (with 0.1 % TFA) in 18 min, 1 mL min^{-1}.

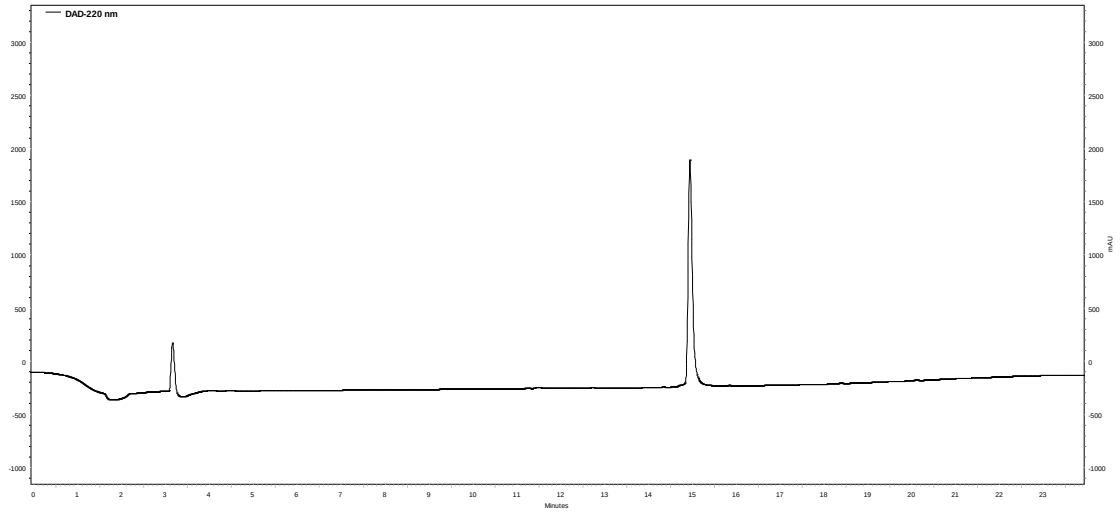

Figure 6.4. HPLC chromatogram of RF05. Chromatogram at 220 nm. Gradient: 5 – 100 MeCN (with 0.1 % TFA) in 18 min, 1 mL min^{-1}.

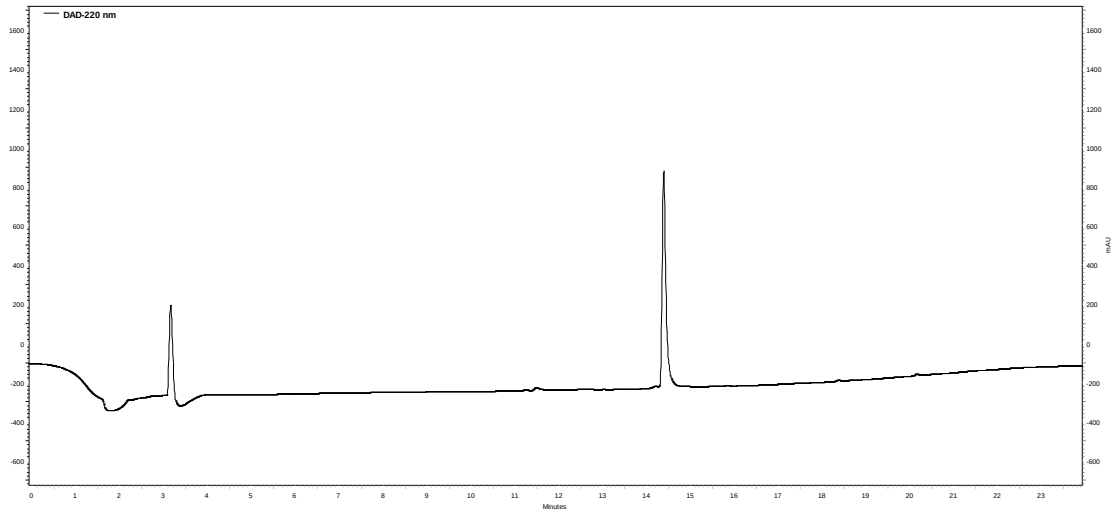

Figure 6.5. HPLC chromatogram of RF06. Chromatogram at 220 nm. Gradient: 5 – 100 MeCN (with 0.1 % TFA) in 18 min, 1 mL min^{-1}.

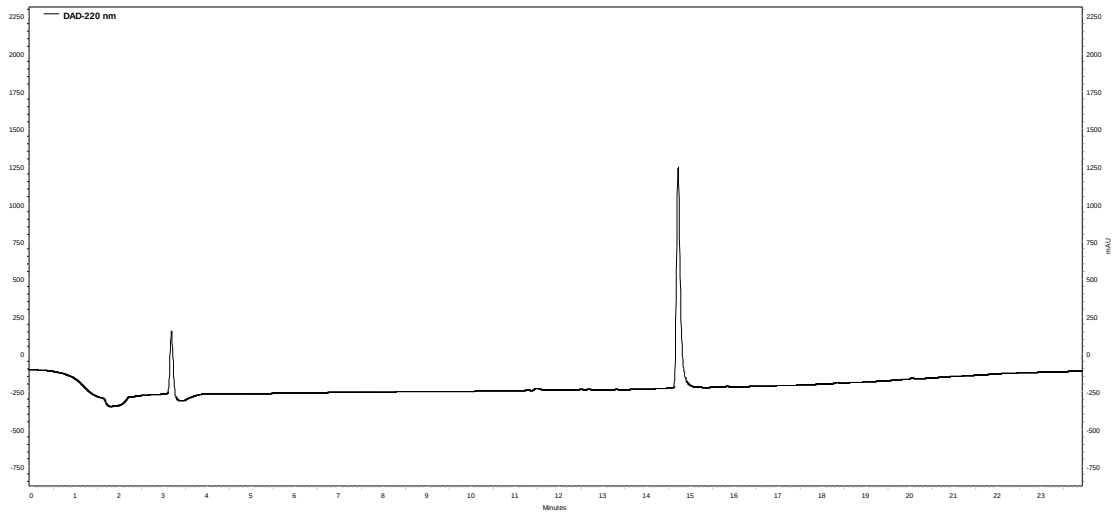

Figure 6.6. HPLC chromatogram of RF08. Chromatogram at 220 nm. Gradient: 5 – 100 MeCN (with 0.1 % TFA) in 18 min, 1 mL min^{-1}.

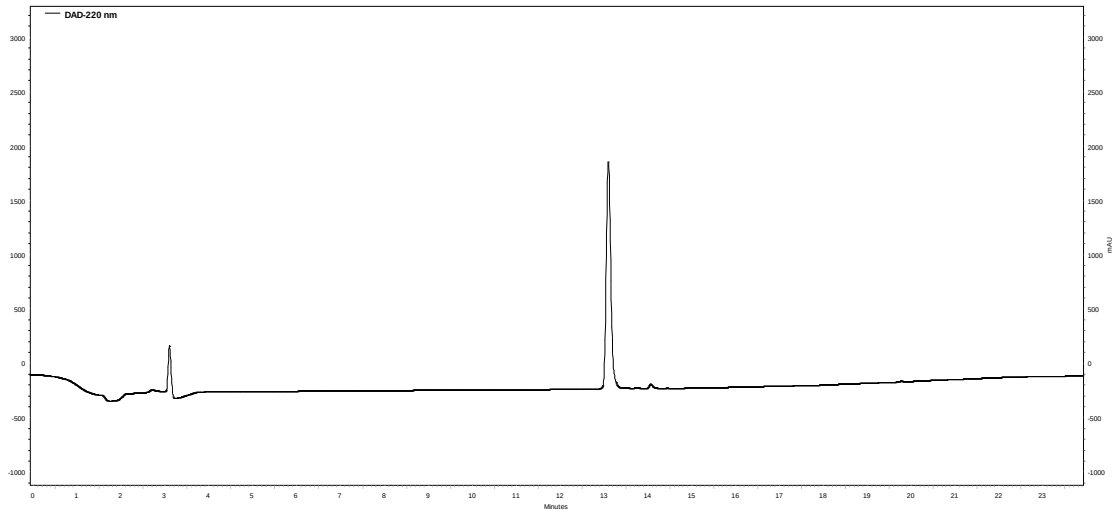

Figure 6.7. HPLC chromatogram of RF09. Chromatogram at 220 nm. Gradient: 5 – 100 MeCN (with 0.1 % TFA) in 18 min, 1 mL min^{-1}.

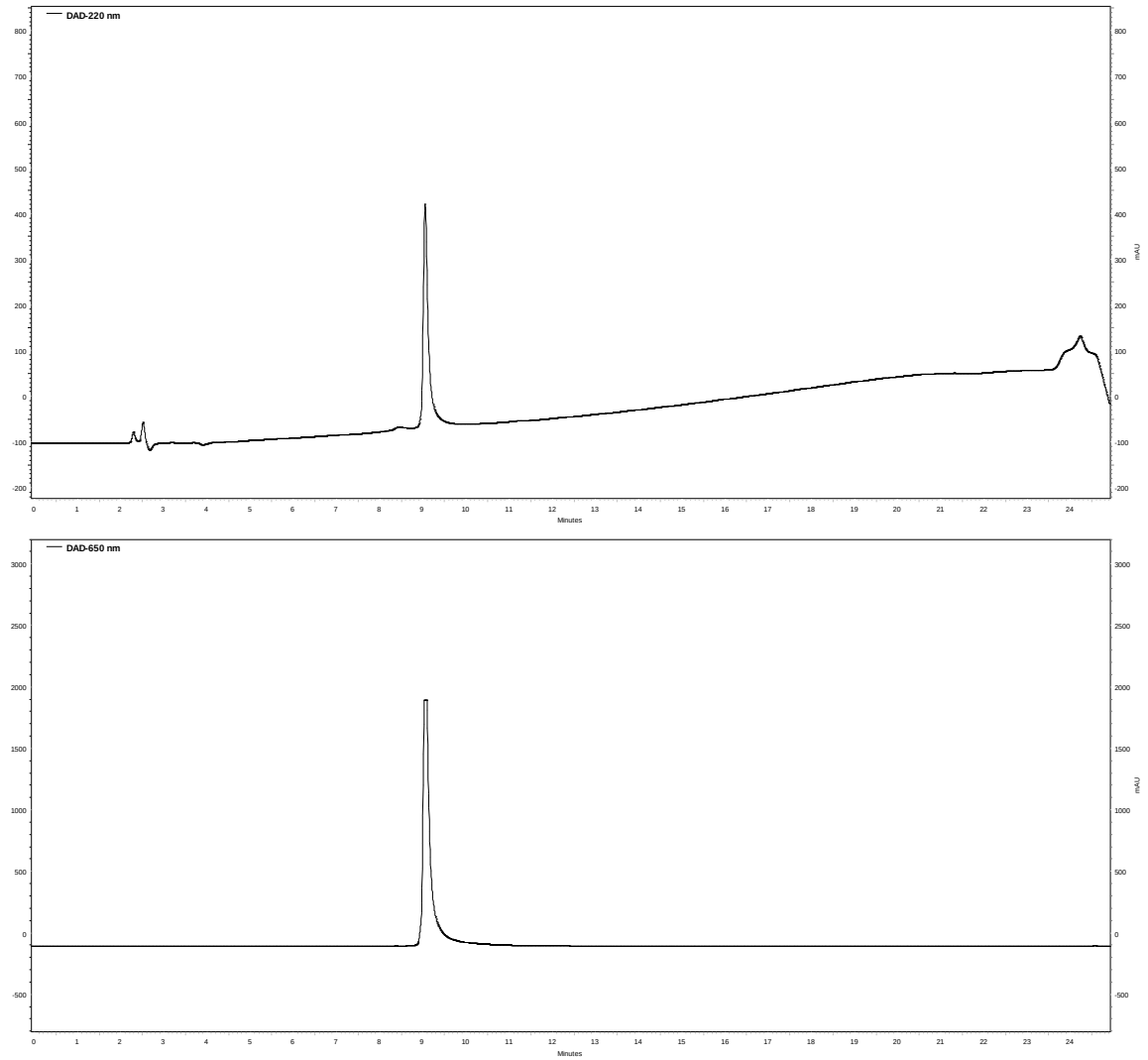

Figure 6.8. HPLC chromatogram of RF011. The upper panel shows chromatogram at 220 nm and bottom panel at 650 nm in 30 – 100 MeCN (with 0.1 % TFA) in 18 min, 1 mL min^{-1}.

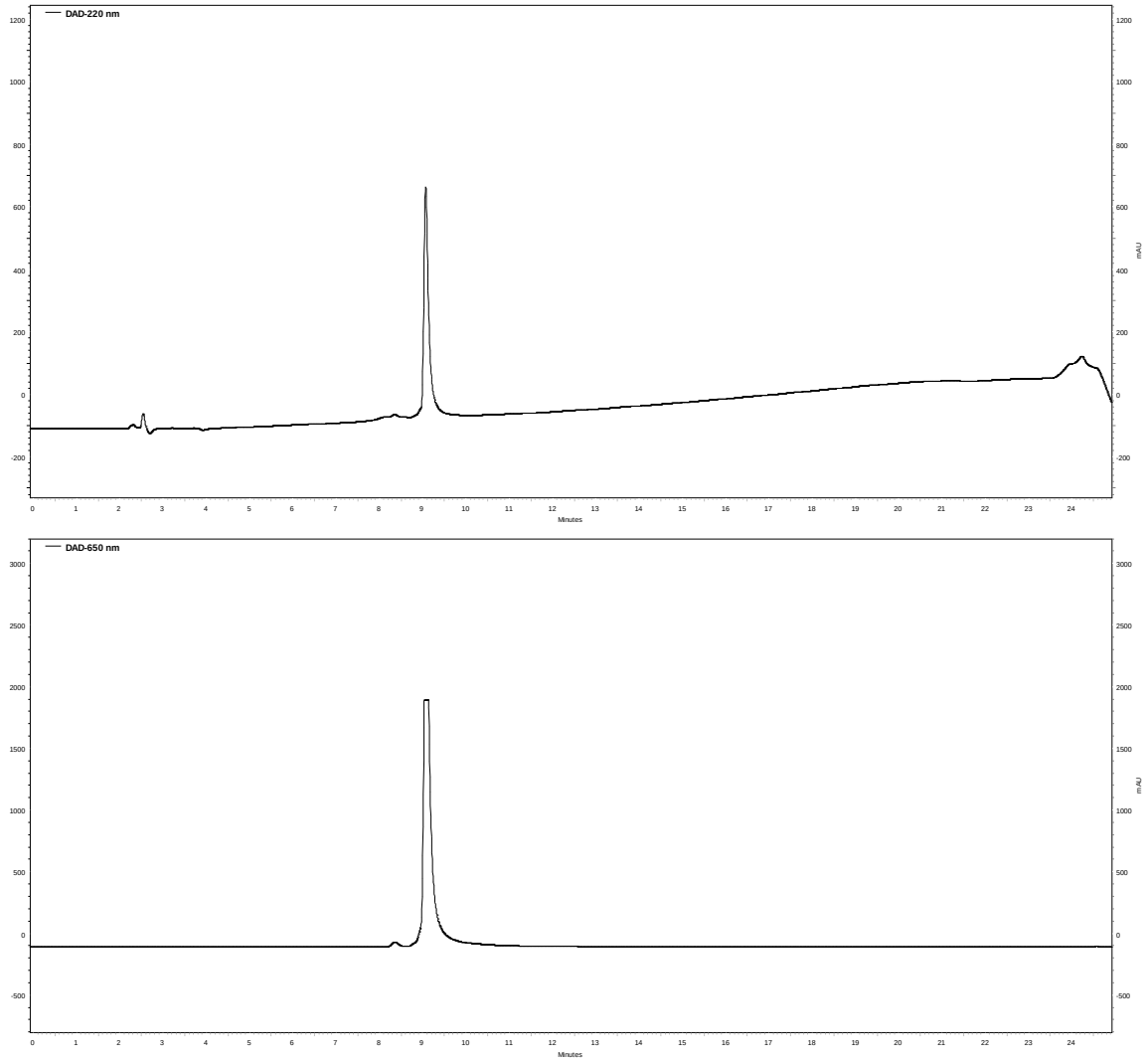

Figure 6.9. HPLC chromatogram of RF012. The upper panel shows chromatogram at 220 nm and bottom panel at 650 nm in 30 – 100 MeCN (with 0.1 % TFA) in 18 min, 1 mL min^{-1}.

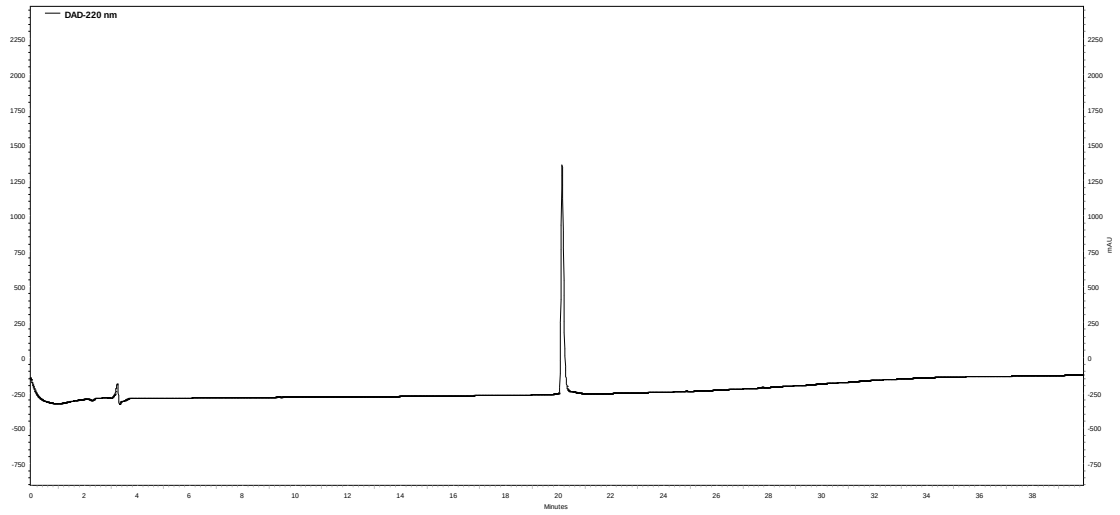

Figure 6.10. HPLC chromatogram of RF013. Chromatogram at 220 nm. Gradient: 5 – 100 MeCN (with 0.1 % TFA) in 30 min, 1 mL min^{-1}.

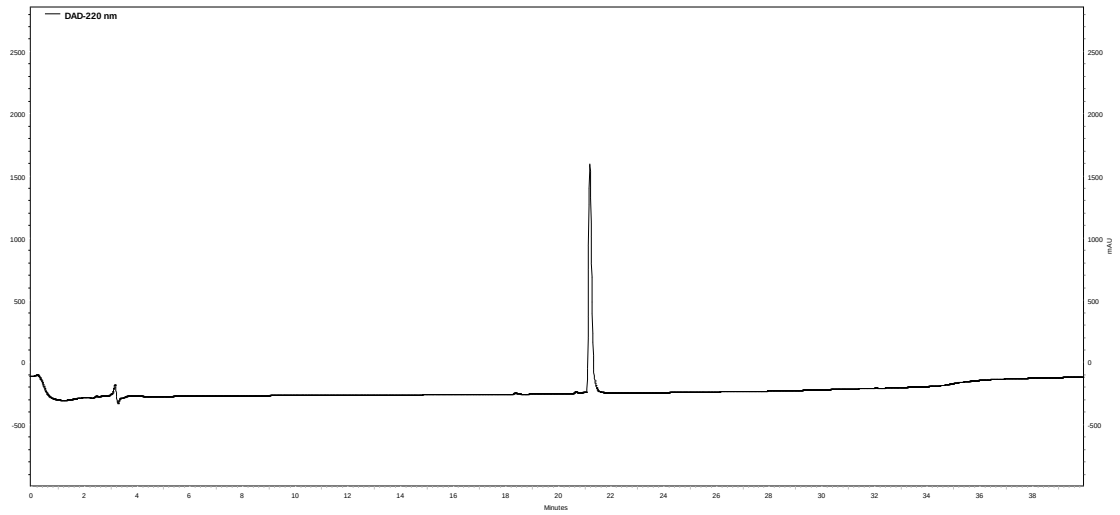

Figure 6.11. HPLC chromatogram of RF014. Chromatogram at 220 nm. Gradient: 10 – 80 MeCN (with 0.1 % TFA) in 30 min, 1 mL min^{-1}.

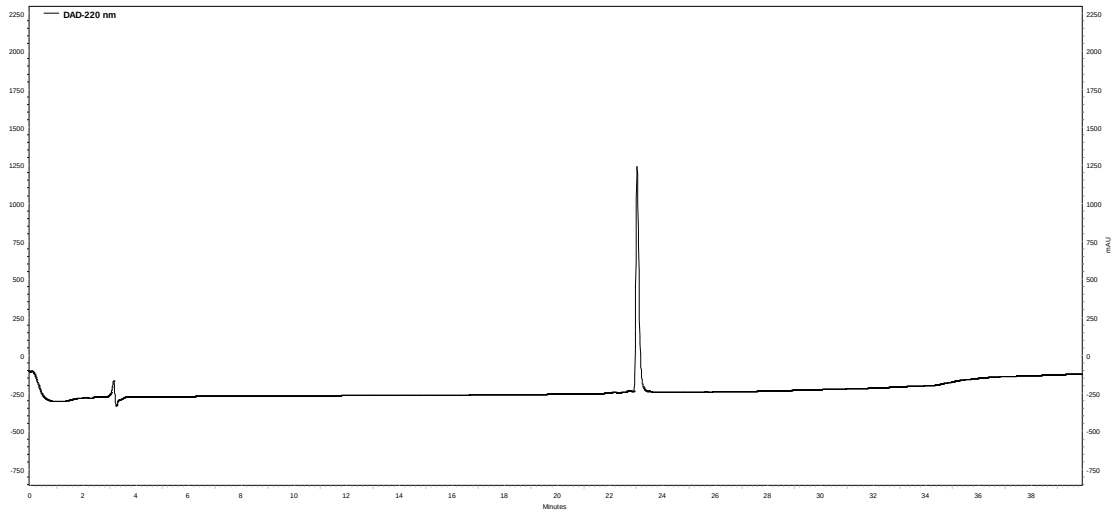

Figure 6.12. HPLC chromatogram of RF015. Chromatogram at 220 nm. Gradient: 10 – 80 MeCN (with 0.1 % TFA) in 30 min, 1 mL min^{-1}.

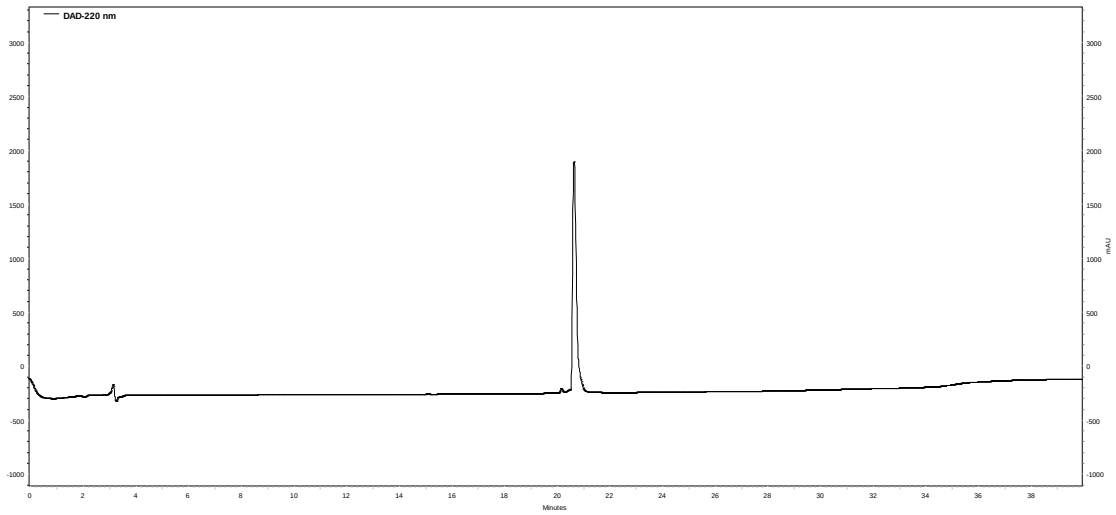

Figure 6.13. HPLC chromatogram of RF016. Chromatogram at 220 nm. Gradient: 10 – 80 MeCN (with 0.1 % TFA) in 30 min, 1 mL min^{-1}.

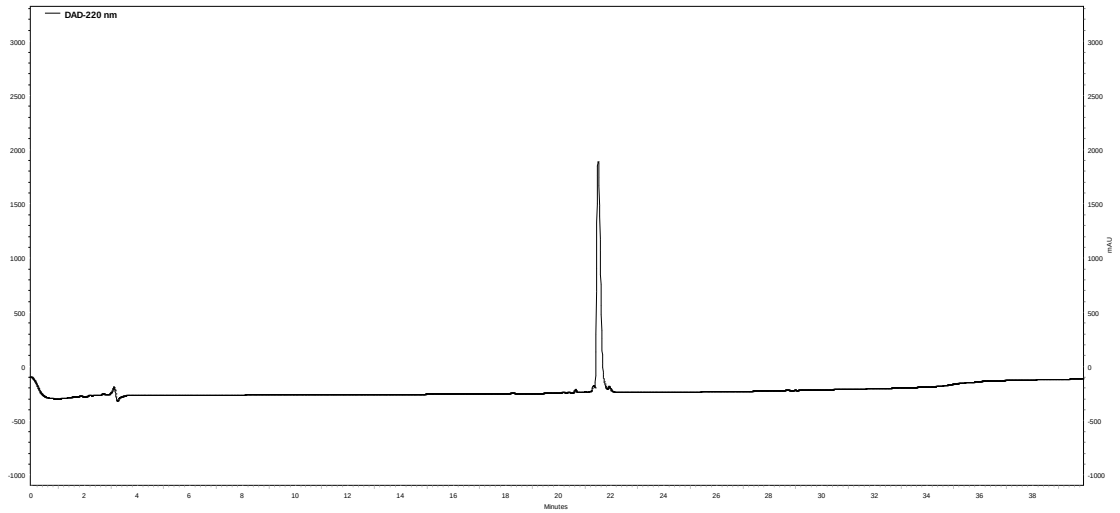

Figure 6.14. HPLC chromatogram of RF017. Chromatogram at 220 nm. Gradient: 10 – 80 MeCN (with 0.1 % TFA) in 30 min, 1 mL min^{-1}.

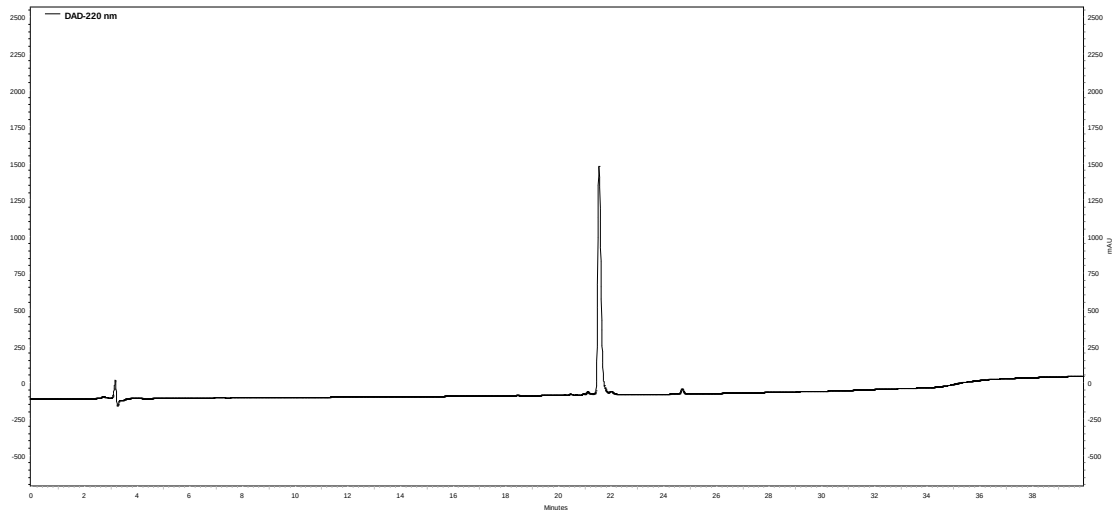

Figure 6.15. HPLC chromatogram of RF018. Chromatogram at 220 nm. Gradient: 10 – 80 MeCN (with 0.1 % TFA) in 30 min, 1 mL min^{-1}.

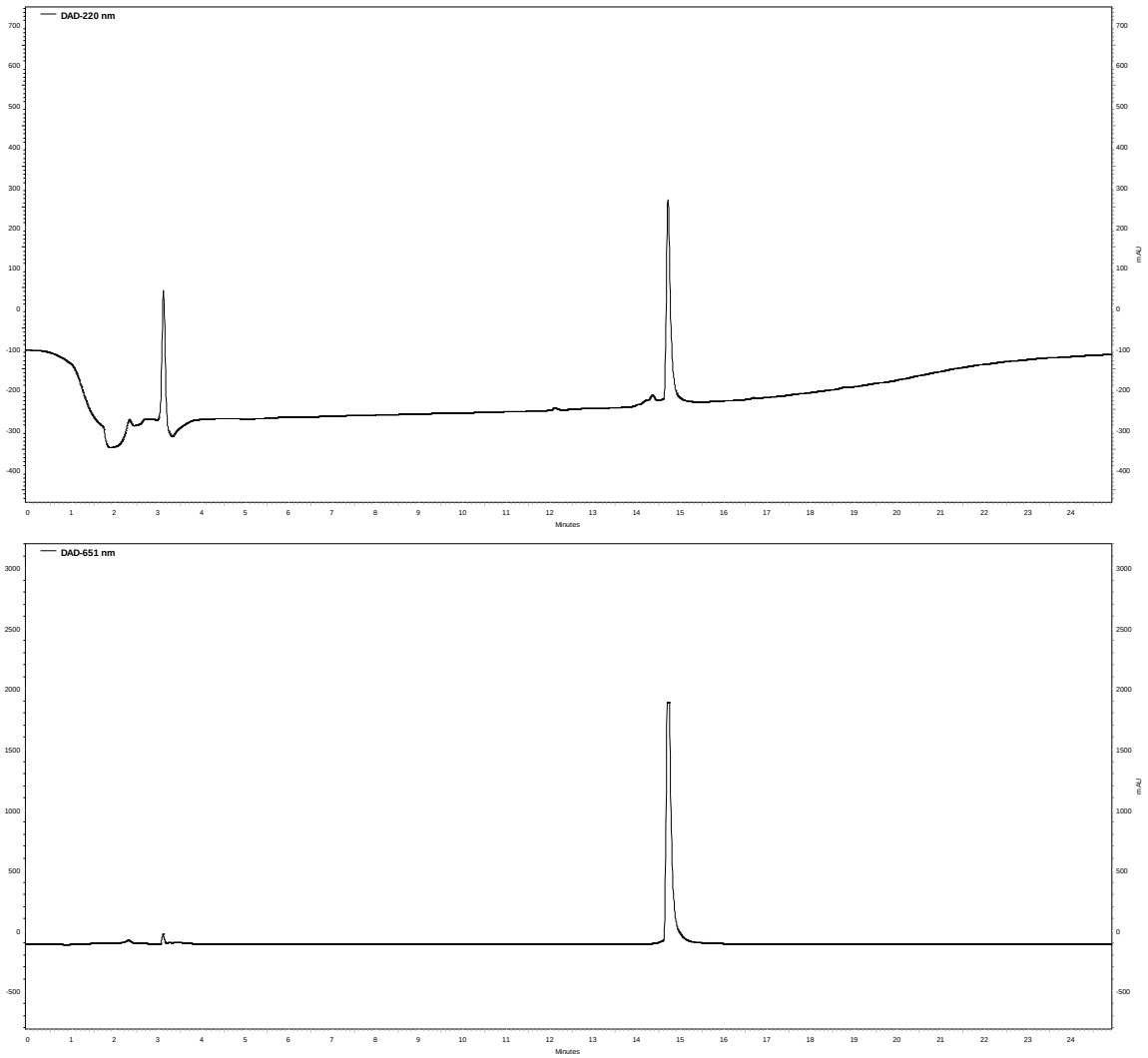

Figure 6.16. HPLC chromatogram of RF019. The upper panel shows chromatogram at 220 nm and bottom panel at 650 nm in 5 – 100 MeCN (with 0.1 % TFA) in 18 min, 1 mL min^{-1}.

6.3. Structural analysis

6.3.1. Circular dichroism spectroscopy

Circular dichroism (CD) spectroscopy is an excellent tool for analysis of the secondary structure of peptides and proteins in solution.[256] Not only can it be used for the fast determination of peptide conformation under a wide range of conditions, but also to monitor conformational transitions, protein interactions, and conformation or stability changes of mutated biomacromolecules.[257] As such, CD was extensively used throughout the studies described in this thesis.

This type of spectroscopy utilizes the differences in the absorbance between left circularly polarized light (lcp) and right circularly polarized light (rcp) by an optical active molecule, in the absence of a magnetic field.[256] The difference in absorbance can be described by taking into account the path length of the beam, *l*, the molar concentration of the solution, *c*, and the molar extinction coefficient, ***ε***, as:

$$\Delta A = A_{lcp} - A_{rcp} = \varepsilon_{lcp} cl - \varepsilon_{rcp} cl = \Delta \varepsilon cl$$

When a plane-polarized light traverses a circular dichroism medium, the difference between the left and right components results in an elliptical beam shape. The shape of the ellipse is described by the position of the electric vectors of the two circular light components. When both electric vectors point in the same direction, the sum of their magnitudes corresponds to the major axis of the ellipse. When each electric vector points in opposite directions, i.e., 180 ° out of phase, the difference between their magnitudes corresponds to the minor axis. CD is a measured of ellipticity, θ, i.e., the angle between the major and minor axis of the ellipse.[256]

Each secondary structural element found in peptides and proteins gives a characteristic CD signal that corresponds to the electron transitions of the amide functionality. α–helical structures are characterized by a double negative band at 222 nm (n→π* transition) and 208 nm (π→π* transition), and a positive band at 193 nm (π→π* transition). The CD spectrum of β-structured peptides gives a characteristic broad negative minimum in the 215 – 220 nm regions (n→π* transition), and a positive band 190 – 200 nm (π_0→π* transition). Unstructured structures (or random coil) exhibit one minimum at around 200 nm (n→π* transition). **Table 6.5** summarizes the CD signals corresponding to backbone amide transitions and used for the determination of peptide secondary structure.

Table 6.5. Summary of the CD signals used for the determination of peptide secondary structure.[256]

Secondary structure	Signal	Electron transition	Wavelength (nm)
α-helix	Negative	n →π*	222
	Negative	π → π *	208
	Positive	π → π *	193
β-sheet	Negative	n → π *	215 – 220
	Positive	$\pi_0 \rightarrow \pi^*$	190 – 200
Unstructured	Negative	n → π *	220

In addition, peptides and proteins can have CD bands in the near UV region (350 to 260 nm) originating from aromatic amino acids and/or prosthetic groups,[258] and in the higher wavelength UV-vis region (400 to 700 nm) originating from fluorescent dye. The bands in these regions are dependent of the tertiary structure of the peptide.[258,259]

6.3.2. Circular dichroism measurements

Circular dichroism (CD) spectra and thermal denaturation spectra were measured using a Jasco J-810 spectropolarimeter fitted with a recirculating chiller (D-76227, Karlsruhe). Data were recorded using 0.1 cm Quartz Suprasil® cuvettes (Hellma) equipped with a stopper. Spectra were recorded at 20 or 25 °C from 190 to 240 nm for secondary structure determination and from 190 to 700 nm for dye studies. The parameters used were as follows: 0.2 nm intervals, 1 nm bandwidth, 1 s response time and a scan speed of 100 nm min^{-1}. Baselines were recorded using the same conditions (buffer, cuvette and parameters) and were subtracted from the data. Buffers used: 50 mM sodium citrate buffer pH 3.4, 50 mM phosphate buffer pH 7.4, and 50 mM CAPS buffer pH 11. Other experimental conditions are stated in the legend of each spectrum. Each reported CD value represents the average of a minimum three measurements.

One of the major factor for poor CD estimates is the inaccurate determination of protein concentration.[258] As stated in the main text, in some cases the low solubility or the evident formation of macroscopic assemblies leads to complication in the concentration determination and to major variation on the CD signal. Therefore, for these cases we present the CD data in *mdeg* and not as the standard molar residual ellipticity (MRE). However, when possible, the ellipticity was normalized mean residue ellipticity (MRE, in 10^3 deg cm^2 $dmol^{-1}$ res^{-1}) according to concentration (*c*, in mol L^{-1}), number of residues (*n*) and the path length (*l*) using the equation (1):

$$MRE = \frac{MRE_{observed}}{10000\, l\, c\, n} \quad (1)$$

The CD data was analysed using ORIGINPRO 2017 and 2019 (Origin Lab).

6.3.3. Determination of helical content

Helical content, or fraction of helicity, is assumed to be directly proportional to the mean residual ellipticity at 222 nm (MRE_{222nm}). The basis to estimate the percentage of helical content was first developed Chen *et al*.[260] This method takes into account the dependence between the number of amino acids (and chromophores) and the intensity of the n→π* transition at 222 nm, according to the following equation:

$$MRE_{222\,nnm} = MRE^{\infty}_{222\,nm}\left(1 - \frac{k}{n}\right) \quad (2)$$

Where $MRE^{\infty}_{222\,nm}$ is the maximum ellipticity of an infinite poly-lysine chain, k is a chain-dependent factor and *n* the number of residues. In this thesis, the helical content was calculated according to equation 3, where $MRE^{\infty}_{222\,nm}$ was assigned as -40 000 (deg cm^2 $dmol^{-1}$ res^{-1}) and *k* as 4.6.[261]

$$helical\ content\ (\%) = \frac{MRE_{222\,nnm}}{-40000\,(\frac{4.6}{n})} \quad (3)$$

6.3.4. Concentration determination

For the preparation of the cy5-labeleld peptides, lyophilized peptide was carefully weight in a microscale to the desired mass. To the peptides were added the desired volume of freshly prepared buffer. Five microliters of the solution were added to 950

microliters of pure MeOH and the absorbance at 650 nm was measured via standard UV-spectroscopy. The concentration of the stock solution (M) was calculated according to the following equation:

$$c\ (M) = \frac{(Abs_{650\ nm} \cdot\ DL)}{150\ 000} \qquad (4)$$

Where DL is the dilution factor and 150 000 M^{-1} cm^{-1} the extinction coefficient of the Cy5 dye in MeOH.[239]

For the remaining peptides lyophilized peptide was carefully weight in a microscale to the desired mass and the desired volume of freshly prepared buffer was added. Ten microliters of the solution were added to 990 microliters of MilliQ® and the absorbance at 205 nm was measured via standard UV-spectroscopy. The concentration was determined according to Anthis *et al*.[262]

6.3.5. Thermal denaturation studies

The thermal transition from a folded state to an unfolded state can be studied by monitoring the dependence of the CD signal at a fixed wavelength and/ or by recording the full peptide spectra at fixed temperature intervals. In the projects described in this thesis, denaturation curves were recorded while monitoring the ellipticity at 222 nm and the full spectra were recorded at 5 °C intervals by heating from 20 or 25 to 95 °C at a rate of 3 °C min^{-1}. The reversibility of the unfolding can be further assessed by monitoring the ellipticity at 222 nm from 95 to 25 or 20 °C at a rate of 3 °C min^{-1} or by repeating the thermal denaturation experiment after the solution cool down. During the realization of this thesis, it was detected that some peptides do not refold reversibly. That is, the unfolding and refolding curves were not superimposed. This was special for the cases were formation of the supramolecular assemblies was evident. As such, the melting temperature (T_M) presented in this thesis should be regarded as apparent. For the project 1 and 3 (where a complex temperature dependence behaviour was observed) the thermal denaturation experiments were performed as follows: a first denaturation was performed immediately after sample preparation; the sample was then allowed to maturate at room temperature for 24 h; after this period of time a second denaturation was performed.

All unfolding and refolding curves were first subjected to a non-linear fit with a Boltzman function using a Levenberg Marquardt iteration algorithm. This fit was automatically performed until a convergent value with a Chi-sqr tolerance value of $1E^{-9}$ was reached. When possible, the apparent melting temperature (T_M) was obtained by the maximum of the first derivative of the nonlinear fitted melting curve as function of temperature. **Figure 6.17-6.20** show the unfolding curves and the respective fitting.

All thermal denaturation data was analysed using ORIGINPRO 2017 and 2019 (Origin Lab).

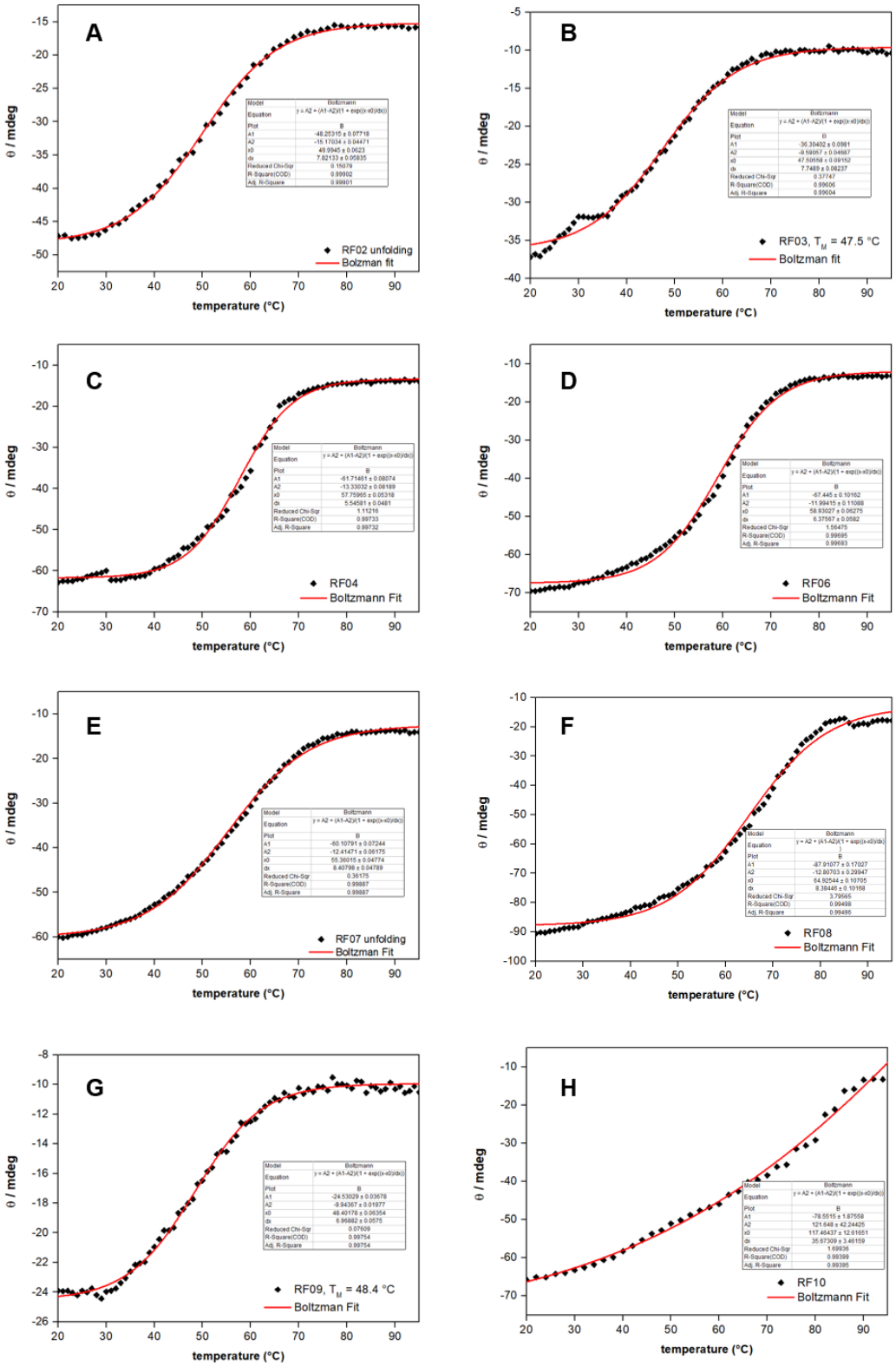

Figure 6.17. Thermal denaturation curves and Boltzmann fit for RF02 (**A**), RF03 (**B**), RF04 (**C**), RF06 (**D**), RF07 (**E**), RF08 (**F**), RF09 (**G**) and RF010 (**G**). The conditions are the same as presented in (**Section 4.2.**). The denaturation curve for RF05 could not be fitted.

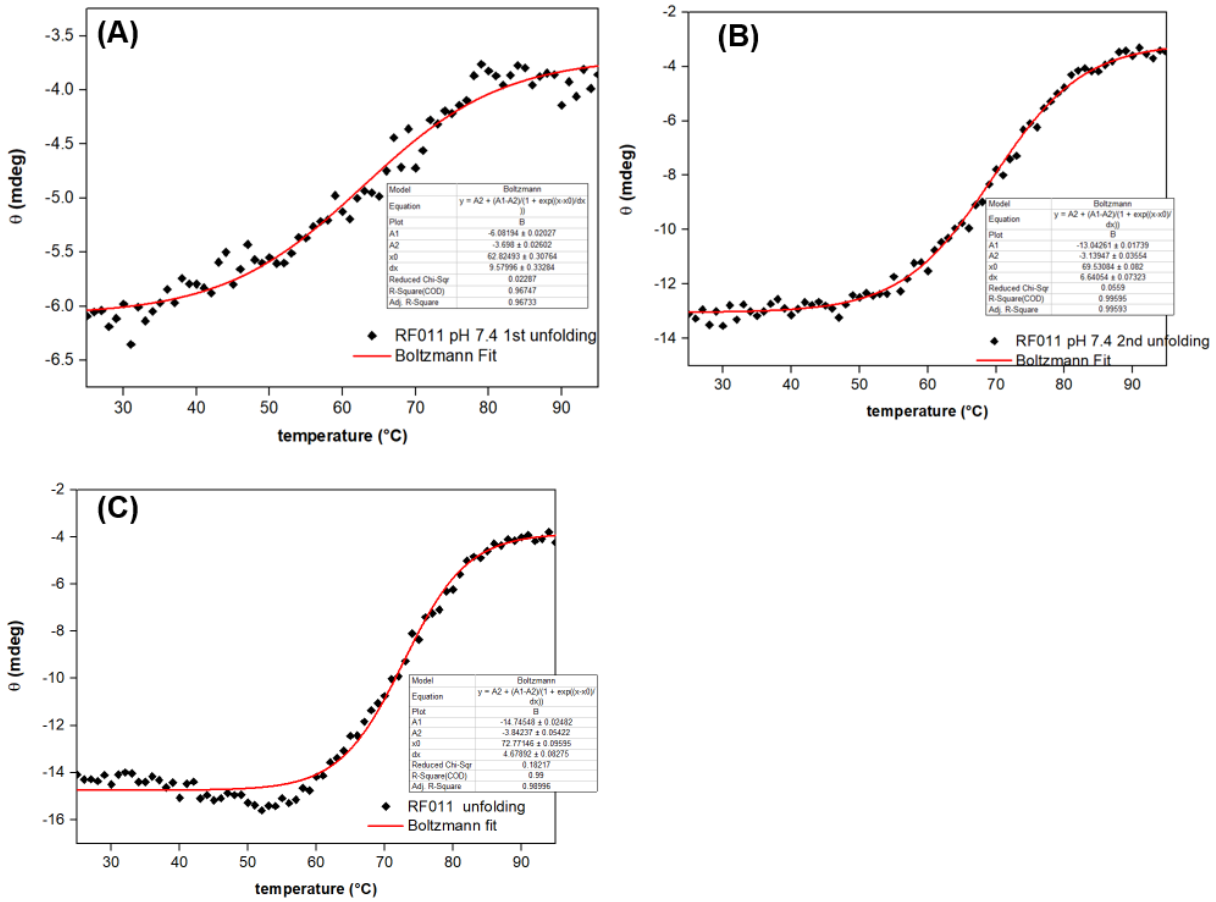

Figure 6.18. Thermal denaturation curves and Boltzmann fit for RF011. (**A**) first denaturation at pH 7.4, second denaturation at pH 7.4 (**B**), and first denaturation at pH 3.4 (**C**). The conditions are the same as presented in (**Section 4.3**). The denaturation curve for RF012 could not be fitted.

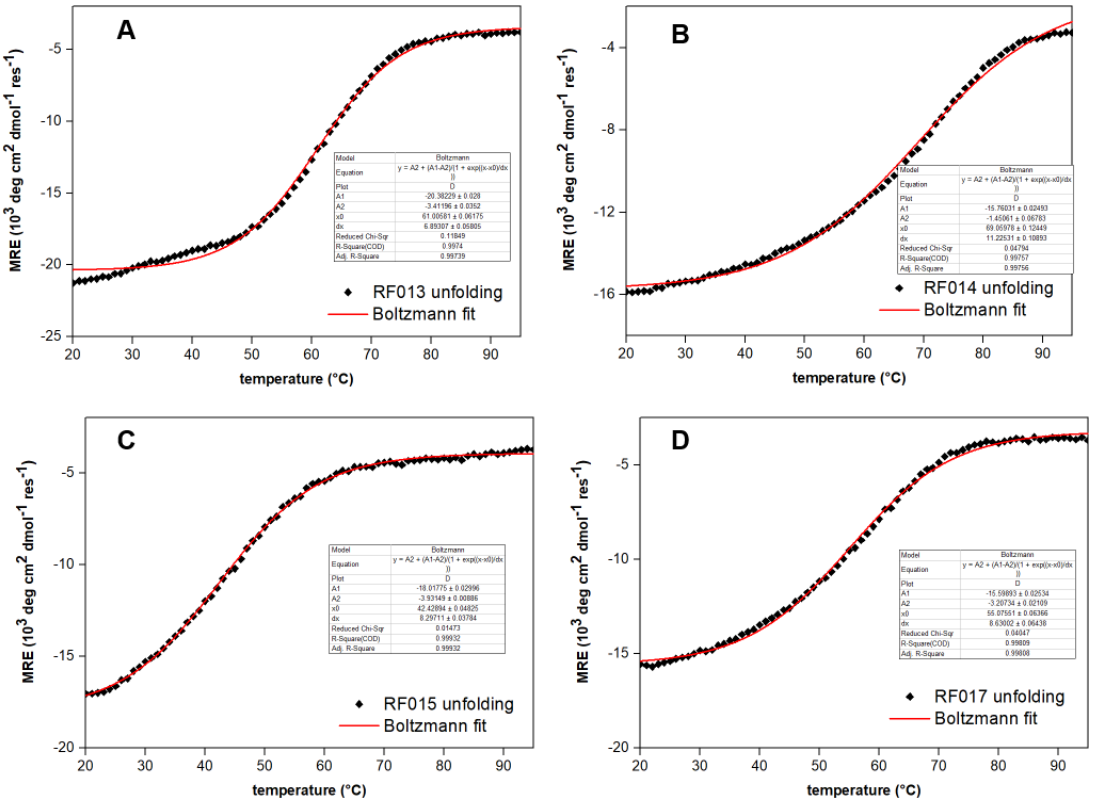

Figure 6.19. Thermal denaturation curves and Boltzmann fit for RF013 (**A**), RF014 (**B**), RF015 (**C**), RF017 (**D**). The conditions are the same as presented in (**Section 4.4**). The denaturation curve for RF016 and RF018 could not be fitted.

6.4. Transmission electron microscopy (TEM) and cryo-TEM[1]

Electron microscopy takes advantage of the dualistic particle-wave properties of electrons to give structural information at high resolution. Such high resolutions can be achieved by accelerating electrons through a range of voltages: higher voltages produce lower wavelengths and high resolutions as 0.1 nm (for comparison, light microscopy is limited to 100 nm in resolution).[263] Two main categories of electron microscopy exist: scanning electron microscopy (SEM) and transmission electron microscopy (TEM). Both cases involve the generation of a beam of electrons that traverse a sample placed inside a vacuum chamber. SEM is usually chosen to study of the morphology of large surfaces. In contrast, the higher resolution of TEM makes

[1] Performed in collaboration with Priv.-Doz. Dr. Christoph Böttcher from the Institut für Chemie und Biochemie Forschungszentrum Elektronenmikroskopie, Fabeckstr. 36a, 14195 Berlin, and in collaboration with Dorian Mikolajczak from the Koksch group of the Institut für Chemie und Biochemie, Takustr. 3, 14195 Berlin.

it the technique of choice to study finer details of nanostructures. Throughout this thesis TEM and cryo-TEM were extensively used to observe and study the supramolecular constructs.

To acquire an image using TEM, a high-voltage electron beam (typically between 200 and 300 keV)[263] is transmitted on a defined area of a sample. The information transmitted is then focused by electrostatic lenses and collected by a detection system, where is translated into a pixel micrograph. When a beam is passing through a specimen, electrons can interact with the sample and scatter (with changing in trajectory and in energy) or unscatter (without change in trajectory or energy loss). In a bright-field imaging mode, scattered electrons are blocked by an objective aperture and only unscattered electrons are used to form an image. Therefore, regions that interact with the electron beam (increased scattering) results in darker contrast. Specially in the case of biological samples, sample scattering can be increased by staining the background with an electron-dense staining solution, usually uranyl salts, ammonium molybdate or phosphotungstic acid.[264] In this so-called negative-staining technique, only the background is stained and the sample is unaffected. In contrary, in a positive-staining technique only the sample is stained. Throughout this thesis, only negative-staining TEM was used. Nevertheless, during the staining process samples can be deformed or interact with the solution, and formation of artefacts can occur. For these reasons, transmission electron cryo microscopy (cryo-TEM) is also extensively used in combination with negative staining TEM.

cryo-TEM is a powerful technique that allows the visualization of biological samples in a frozen near native state. In this technique, an aqueous solution is placed in a solid support (grid) and rapidly vitrified, forming a thin film. The grid is then transferred to the electron microscope vacuum chamber, where is cooled down with liquid nitrogen to -180 °C to avoid melting and evaporation.[265] The main disadvantages of cryo-TEM are the intrinsic low image contrast from the biological materials and the formation of water crystals.

6.4.1. Negative staining TEM and cryo-TEM protocol

Samples for negative staining TEM were prepared by absorbing 5 µL aliquots of peptide solution onto glow-discharged carbon-coated collodium films on 400-mesh copper grids. The grids were blotted, stained with 1% phosphotungstic acid (PTA), and air dried. TEM micrographs were taken at a primary magnification of 58300 using a defocus of 0.8 µm.

Samples for cryo-TEM were prepared by adding a droplet of 10 µL peptide solution on a hydrophilized perforated carbon filmed grid (60 s plasma treatment at 8 W using a BALTEC MED 020 device) at room temperature. The supernatant fluid was removed with filter paper and the grids were immediately vitrified in liquid ethane at its freezing point (- 184 °C) using a standard plunging device. The vitrified samples were transferred under liquid nitrogen into a Philips CM12 transmission electron microscope by using the Gatan cryo holder and stage (model 626). Microscopy was carried out at a sample temperature of -175 °C by using the low-dose protocol of the microscope at a primary magnification of 58300× with a defocus of 1.5µm.

All negative staining TEM and cryo-TEM data were analysed using ImageJ 1.50i (NIH, USA).[266]

6.5. Infrared nano-spectroscopy[2]

Near-field IR microscopy (SNIM) and nano-FTIR spectroscopy are super resolution techniques used for chemical imaging and spectroscopy on a nanoscale. The instrumentation is equipped with an AFM and tunable laser, capable of recording topography and images of the infrared light scattered, revealing the local IR response of the sample.

Owing to the different peptide folding conformation, the amide bond absorbs in different regions of the IR spectra. For α-helical conformations the bands in the range of 1648 and 1660 cm^{-1} are assigned to amide I and the range of 1545 and

[2] Work performed in collaboration with Katerina Kanevche and Emanuel Pfitzner from the Heberle group of the Department of Physics, Arnimallee 14, 14195 Berlin.

1551 cm^{-1} to amide II; for β-sheet similar absorption bands will occur between 1625 and 16 cm^{-1} and 1521 and 1525 cm^{-1}, respectively.[267]

Samples for nano-FTIR were prepared by depositing 5 µL of peptide solutions onto a gold substrate, followed by spin coating and drying.

6.6. ^{19}F MRI[3]

Magnetic resonance imaging is based on the same principles governing nuclear magnetic resonance (NMR).

Three peptide solutions were prepared by adding sterile phosphate-buffered saline (PBS) to freeze-dried peptide. Upon each buffer addition, the solution was vortexed, centrifuged and the supernatant transferred to a new tube. Concentration determination was performed accordingly to described in Section 6.3.4. Because of the low concentration, two tubes were combined (**Table 6.6**).

Table 6.6. Solutions used for magnetic resonance measurements**.**[3]

Tube	Conditions	Volume (µL)	Concentration (µM)	Estimated total number of F atoms
1	Untreated solution	500	5.12	4.7×10^{15}
2	Annealed solution	500	19.4	5.2×10^{16}

Spectroscopy experiments were performed using the untreated solution. No ^{19}F peak or relaxation time were obtained for the thermally annealed solution.

[3] Performed by Dr. Sonia Waiczies and Dr. Min-Chi Ku from the Berlin Ultrahigh Field Facility, Max Delbrück Center for Molecular Medicine, Berlin, Germany.

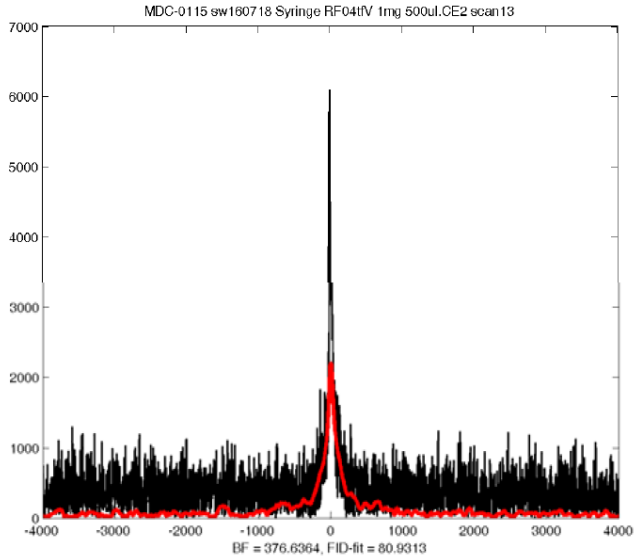

Figure 6.20. ^{19}F peak in a single voxel using a PRESS sequence (512 averages, 6m52s800ms) of an untreated solution.

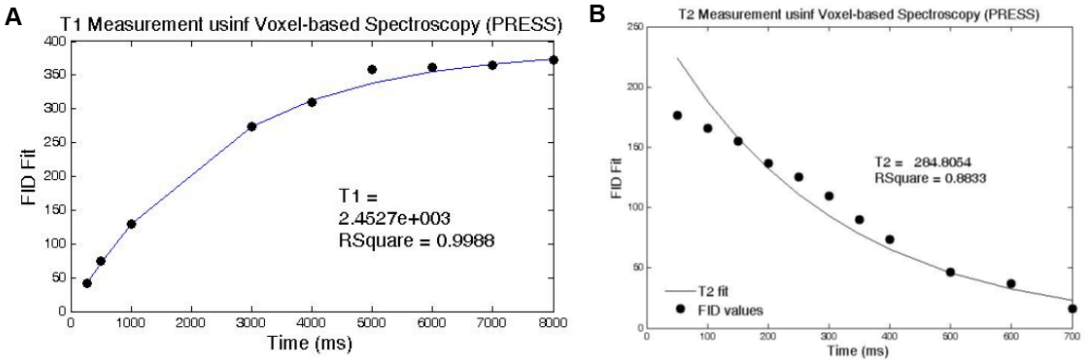

Figure 6.21. Relaxation times measured using PRESS. (**A**) T1 and (**B**) T2 obtained 3 days after solution preparation.

6.7. Catalytical activity protocol

Untreated and thermal annealed solutions were prepared as previously described.

Table 6.7. Conditions used for catalytical activity determination. Absorbance was measured at 405 nm.

	Conditions
Blank	980 µL buffer + 14.24 µL MeCN + 5.76 µL *p*NPA in MeCN
Peptide	900 µL buffer + 80 µL PT01H17 (6.5 µM) + 14.24 µL MeCN + 5.76 µL *p*NPA in MeCN
Blank	980 µL buffer + 14.24 µL ACN + 5.76 µL *p*NPA in MeCN + 1.3 µL $ZnCl_2$ (2.2 µM)
Peptide	900 µL buffer + 80 µL PT01H17 (6.5 µM) + 14.24 µL ACN + 5.76 µL *p*NPA in CAN + 1.3 µL $ZnCl_2$ (2.2 µM)

Buffer: 50 mM phosphate buffer, pH 7.4.

7. References

1. Luo, Q., Hou, C., Bai, Y., Wang, R. & Liu, J. Protein Assembly: Versatile Approaches to Construct Highly Ordered Nanostructures. *Chem. Rev.* **116**, 13571–13632 (2016).
2. Krieg, E., Bastings, M. M. C., Besenius, P. & Rybtchinski, B. Supramolecular Polymers in Aqueous Media. *Chem. Rev.* **116**, 2414–2477 (2016).
3. Yan, X., Zhu, P. & Li, J. Self-assembly and application of diphenylalanine-based nanostructures. *Chem. Soc. Rev.* **39**, 1877–1890 (2010).
4. Goor, O. J. G. M., Hendrikse, S. I. S., Dankers, P. Y. W. & Meijer, E. W. From supramolecular polymers to multi-component biomaterials. *Chem. Soc. Rev.* **46**, 6621–6637 (2017).
5. MacPhee, C. E. & Woolfson, D. N. Engineered and designed peptide-based fibrous biomaterials. *Curr. Opin. Solid State Mater. Sci.* **8**, 141–149 (2004).
6. Lehn, J.-M. Perspectives in Supramolecular Chemistry—From Molecular Recognition towards Molecular Information Processing and Self-Organization. *Angew. Chemie Int. Ed. English* **29**, 1304–1319 (1990).
7. Woolfson, D. N. & Mahmoud, Z. N. More than just bare scaffolds: towards multi-component and decorated fibrous biomaterials. *Chem. Soc. Rev.* **39**, 3464–79 (2010).
8. Zhang, S. Fabrication of novel biomaterials through molecular self-assembly. *Nat. Biotechnol.* **21**, 1171–1178 (2003).
9. Smith, K. H., Tejeda-Montes, E., Poch, M. & Mata, A. Integrating top-down and self-assembly in the fabrication of peptide and protein-based biomedical materials. *Chem. Soc. Rev.* **40**, 4563–4577 (2011).
10. Philp, D. & Fraser Stoddart, J. Self-Assembly in natural and unnatural systems. *Angew. Chemie (International Ed. English)* **35**, 1154–1196 (1996).
11. Nie, Z. & Kumacheva, E. Patterning surfaces with functional polymers. *Nat. Mater.* **7**, 277 (2008).
12. Whitesides, G. M. Self-Assembly at All Scales. *Science.* **295**, 2418–2421 (2002).
13. Makam, P. & Gazit, E. Minimalistic peptide supramolecular co-assembly: Expanding the conformational space for nanotechnology. *Chem. Soc. Rev.* **47**, 3406–3420 (2018).
14. Brunsveld, L., Folmer, B. J. B., Meijer, E. W. & Sijbesma, R. P. Supramolecular Polymers. *Chem. Rev.* **101**, 4071–4098 (2001).
15. Zhang, S. Emerging biological materials through molecular self-assembly. *Biotechnol. Adv.* **20**, 321–339 (2002).
16. Lupas, A. N. & Bassler, J. Coiled Coils – A Model System for the 21st Century. *Trends Biochem. Sci.* **42**, 130–140 (2017).
17. Wu, C. *et al.* Fluorine substitution enhances the self-assembling ability of hydrogelators. *Nanoscale* **9**, 11429–11433 (2017).
18. Fleming, S. & Ulijn, R. V. Design of nanostructures based on aromatic peptide amphiphiles. *Chem. Soc. Rev.* **43**, 8150–8177 (2014).
19. Mart, R. J., Osborne, R. D., Stevens, M. M. & Ulijn, R. V. Peptide-based stimuli-responsive biomaterials. *Soft Matter* **2**, 822–835 (2006).
20. Gazit, E. Self-assembled peptide nanostructures: The design of molecular building blocks and their technological utilization. *Chem. Soc. Rev.* **36**, 1263–1269 (2007).

21. Branco, M. C. & Schneider, J. P. Self-assembling materials for therapeutic delivery. *Acta Biomater.* **5**, 817–831 (2009).
22. De Santis, E. & Ryadnov, M. G. Peptide self-assembly for nanomaterials: The old new kid on the block. *Chem. Soc. Rev.* **44**, 8288–8300 (2015).
23. Tao, K., Makam, P., Aizen, R. & Gazit, E. Self-assembling peptide semiconductors. *Science.* **358**, eaam9756 (2017).
24. Webber, M. J., Appel, E. A., Meijer, E. W. & Langer, R. Supramolecular biomaterials. *Nat. Mater.* **15**, 13–26 (2015).
25. Ulijn, R. V. & Smith, A. M. Designing peptide based nanomaterials. *Chem. Soc. Rev.* **37**, 664–675 (2008).
26. Stephanopoulos, N., Ortony, J. H. & Stupp, S. I. Self-assembly for the synthesis of functional biomaterials. *Acta Mater.* **61**, 912–930 (2013).
27. Toksoz, S., Acar, H. & Guler, M. O. Self-assembled one-dimensional soft nanostructures. *Soft Matter* **6**, 5839–5849 (2010).
28. Löwik, D. W. P. M., Leunissen, E. H. P., Van Den Heuvel, M., Hansen, M. B. & Van Hest, J. C. M. Stimulus responsive peptide based materials. *Chem. Soc. Rev.* **39**, 3394–3412 (2010).
29. Ekiz, M. S., Cinar, G., Khalily, M. A. & Guler, M. O. Self-assembled peptide nanostructures for functional materials. *Nanotechnology* **27**, 402002 (2016).
30. Webber, M. J. Engineering responsive supramolecular biomaterials: Toward smart therapeutics. *Bioeng. Transl. Med.* **1**, 252–266 (2016).
31. Crick, F. H. C. Is alpha-keratin a coiled coil? *Nature* **170**, 882–883 (1952).
32. Crick, F. H. C. The packing of α-helices: simple coiled-coils. *Acta Crystallogr.* **6**, 689–697 (1953).
33. O'Shea, E., Klemm, J., Kim, P. & Alber, T. X-ray structure of the GCN4 leucine zipper, a two-stranded, parallel coiled coil. *Science.* **254**, 539–544 (1991).
34. Landschulz, W., Johnson, P. & McKnight, S. The leucine zipper: a hypothetical structure common to a new class of DNA binding proteins. *Science.* **240**, 1759–1764 (1988).
35. Glover, J. N. M. & Harrison, S. C. Crystal structure of the heterodimeric bZIP transcription factor c-Fos–c-Jun bound to DNA. *Nature* **373**, 257 (1995).
36. *Fibrous Proteins: Structures and Mechanisms*. **82**, (Springer International Publishing, 2017).
37. Fasshauer, D. Structural insights into the SNARE mechanism. *Biochim. Biophys. Acta - Mol. Cell Res.* **1641**, 87–97 (2003).
38. Woolfson, D. N. The Design of Coiled-Coil Structures and Assemblies. in *Advances in Protein Chemistry* **70**, 79–112 (Academic Press, 2005).
39. Woolfson, D. N. Building fibrous biomaterials from alpha-helical and collagen-like coiled-coil peptides. *Biopolymers* **94**, 118–127 (2010).
40. Pauling, L., Corey, R. B. & Branson, H. R. The structure of proteins: Two hydrogen-bonded helical configurations of the polypeptide chain. *Proc. Natl. Acad. Sci.* **37**, 205–211 (1951).
41. Pettersen, E. F. *et al.* UCSF Chimera - A visualization system for exploratory research and analysis. *J. Comput. Chem.* **25**, 1605–1612 (2004).
42. Harbury, P. B., Zhang, T., Kim, P. S. & Alber, T. A switch between two-, three-, and four-stranded coiled coils revealed by mutants of the GCN4 leucine zipper. *Science.* **262**, 1401–1407 (1993).
43. Lupas, A. N. & Gruber, M. The structure of alpha-helical coiled-coils. *Adv. Protein Chem.* **70**, 37–78 (2005).

44. O'Shea, E., Klemm, J., Kim, P. & Alber, T. X-ray structure of the GCN4 leucine zipper, a two-stranded, parallel coiled coil. *Science.* **254**, 539–544 (1991).
45. Harbury, P. B., Kim, P. S. & Alber, T. Crystal structure of an isoleucine-zipper trimer. *Nature* **371**, 80–83 (1994).
46. Gonzalez, L., Woolfson, D. N. & Alber, T. Buried polar residues and structural specificity in the GCN4 leucine zipper. *Nat. Struct. Biol.* **3**, 1011–1018 (1996).
47. Monera, O. D., Sönnichsen, F. D., Hicks, L., Kay, C. M. & Hodges, R. S. The relative positions of alanine residues in the hydrophobic core control the formation of two-stranded or four-stranded α-helical coiled-coils. *Protein Eng.* **9**, 353–363 (1996).
48. Monera, O. D., Zhou, N. E., Lavigne, P., Kay, C. M. & Hodges, R. S. Formation of Parallel and Antiparallel Coiled-coils Controlled by the Relative Positions of Alanine Residues in the Hydrophobic Core. *J. Biol. Chem.* **271**, 3995–4001 (1996).
49. Oakley, M. & Kim, P. S. A Buried Polar Interaction Can Direct the Relative Orientation of Helices in a Coiled Coil. *Biochemistry* **37**, 12603–12610 (1998).
50. McClain, D. L., Binfet, J. P. & Oakley, M. Evaluation of the energetic contribution of interhelical coulombic interactions for coiled coil helix orientation specificity. *J. Mol. Biol.* **313**, 371–383 (2001).
51. Monera, O. D., Kay, C. M. & Hodges, R. S. Electrostatic Interactions Control the Parallel and Antiparallel Orientation of α-Helical Chains in Two-Stranded α-Helical Coiled-Coils. *Biochemistry* **33**, 3862–3871 (1994).
52. Zhou, N. E., Kay, C. M. & Hodges, R. S. The net energetic contribution of interhelical electrostatic attractions to coiled-coil stability. *Protein Eng. Des. Sel.* **7**, 1365–1372 (1994).
53. Zhou, N. E., Kay, C. M. & Hodges, R. S. The Role of Interhelical Ionic Interactions in Controlling Protein Folding and Stability. *J. Mol. Biol.* **237**, 500–512 (1994).
54. Kohn, W. D., Kay, C. M. & Hodgson, L. Protein destabilization by electrostatic repulsions in the two-stranded α-helical coiled-coil/leucine zipper. *Protein Sci.* **4**, 237–250 (1995).
55. Kojima, S., Kuriki, Y., Yoshida, T., Yazaki, K. & Miura, K. Fibril Formation By an Amphipathic Alpha-Helix-Forming Polypeptide Produced By Gene Engineering. *Proc. Japan Acad. Ser. B-Physical Biol. Sci.* **73**, 7–11 (1997).
56. Kojima, S., Kuriki, Y., Yazaki, K. & Miura, K. Stabilization of the fibrous structure of an α-helix-forming peptide by sequence reversal. *Biochem. Biophys. Res. Commun.* **331**, 577–582 (2005).
57. Takei, T. *et al.* Effects of chain length of an amphipathic polypeptide carrying the repeated amino acid sequence (LETLAKA)n on α-helix and fibrous assembly formation. *Biochemistry* **52**, 2810–2820 (2013).
58. Potekhin, S. A. *et al.* De novo design of fibrils made of short α-helical coiled coil peptides. *Chem. Biol.* **8**, 1025–1032 (2001).
59. Melnik, T. N. *et al.* Shift of fibril-forming ability of the designed -helical coiled-coil peptides into the physiological pH region. *Protein Eng. Des. Sel.* **16**, 1125–1130 (2003).
60. Pandya, M. J. *et al.* Sticky-End Assembly of a Designed Peptide Fiber Provides Insight into Protein Fibrillogenesis †. *Biochemistry* **39**, 8728–8734 (2000).
61. Zimenkov, Y., Conticello, V. P., Guo, L. & Thiyagarajan, P. Rational design of

a nanoscale helical scaffold derived from self-assembly of a dimeric coiled coil motif. *Tetrahedron* **60**, 7237–7246 (2004).
62. Zimenkov, Y. *et al.* Rational design of a reversible pH-responsive switch for peptide self-assembly. *J. Am. Chem. Soc.* **128**, 6770–6771 (2006).
63. Dublin, S. N. & Conticello, V. P. Design of a selective metal ion switch for self-assembly of peptide-based fibrils. *J. Am. Chem. Soc.* **130**, 49–51 (2008).
64. Wagner, D. E. *et al.* Toward the development of peptide nanofilaments and nanoropes as smart materials. *Proc. Natl. Acad. Sci. U. S. A.* **102**, 12656–12661 (2005).
65. Gribbon, C. *et al.* MagicWand: A Single, Designed Peptide That Assembles to Stable, Ordered α-Helical Fibers †. *Biochemistry* **47**, 10365–10371 (2008).
66. Dong, H., Paramonov, S. E. & Hartgerink, J. D. Self-Assembly of α-Helical Coiled Coil Nanofibers. *J. Am. Chem. Soc.* **130**, 13691–13695 (2008).
67. Ryadnov, M. G. & Woolfson, D. N. Engineering the morphology of a self-assembling protein fibre. *Nat. Mater.* **2**, 329–332 (2003).
68. Ryadnov, M. G. & Woolfson, D. N. Introducing branches into a self-assembling peptide fiber. *Angew. Chemie - Int. Ed.* **42**, 3021–3023 (2003).
69. Smith, A. M., Banwell, E. F., Edwards, W. R., Pandya, M. J. & Woolfson, D. N. Engineering Increased Stability into Self-Assembled Protein Fibers. *Adv. Funct. Mater.* **16**, 1022–1030 (2006).
70. Ryadnov, M. G. & Woolfson, D. N. Self-Assembled Templates for Polypeptide Synthesis. *J. Am. Chem. Soc.* **129**, 14074–14081 (2007).
71. Papapostolou, D. *et al.* Engineering nanoscale order into a designed protein fiber. *Proc. Natl. Acad. Sci.* **104**, 10853–10858 (2007).
72. Seo, J. & Cohen, C. Pitch diversity in alpha-helical coiled coils. *Proteins* **15**, 223–34 (1993).
73. Sharp, T. H. *et al.* Cryo-transmission electron microscopy structure of a gigadalton peptide fiber of de novo design. *Proc. Natl. Acad. Sci.* **109**, 13266–13271 (2012).
74. Xu, C. *et al.* Rational design of helical nanotubes from self-assembly of coiled-coil lock washers. *J. Am. Chem. Soc.* **135**, 15565–15578 (2013).
75. Burgess, N. C. *et al.* Modular Design of Self-Assembling Peptide-Based Nanotubes. *J. Am. Chem. Soc.* **137**, 10554–10562 (2015).
76. Thomas, F., Burgess, N. C., Thomson, A. R. & Woolfson, D. N. Controlling the Assembly of Coiled-Coil Peptide Nanotubes. *Angew. Chemie Int. Ed.* **55**, 987–991 (2016).
77. Egelman, E. H. *et al.* Structural Plasticity of Helical Nanotubes Based on Coiled-Coil Assemblies. *Structure* **23**, 280–289 (2015).
78. Faruqui, N. *et al.* Differentially instructive extracellular protein micro-nets. *J. Am. Chem. Soc.* **136**, 7889–7898 (2014).
79. Fletcher, J. M. *et al.* Self-Assembling Cages from Coiled-Coil Peptide Modules. *Science.* **340**, 595–599 (2013).
80. Banwell, E. F. *et al.* Rational design and application of responsive α-helical peptide hydrogels. *Nat. Mater.* **8**, 596–600 (2009).
81. Ryadnov, M. G. A self-assembling peptide polynanoreactor. *Angew. Chemie - Int. Ed.* **46**, 969–972 (2007).
82. Gradišar, H. *et al.* Design of a single-chain polypeptide tetrahedron assembled from coiled-coil segments. *Nat. Chem. Biol.* **9**, 362–366 (2013).
83. Apostolovic, B., Danial, M. & Klok, H.-A. Coiled coils: Attractive protein folding

motifs for the fabrication of self-assembled, responsive and bioactive materials. *Chem. Soc. Rev.* **39**, 3541–3575 (2010).
84. Nambiar, M., Wang, L.-S., Rotello, V. & Chmielewski, J. Reversible Hierarchical Assembly of Trimeric Coiled-Coil Peptides into Banded Nano- and Microstructures. *J. Am. Chem. Soc.* **140**, 13028–13033 (2018).
85. Wang, W., Nema, S. & Teagarden, D. Protein aggregation-Pathways and influencing factors. *Int. J. Pharm.* **390**, 89–99 (2010).
86. Pagel, K. & Koksch, B. Following polypeptide folding and assembly with conformational switches. *Curr. Opin. Chem. Biol.* **12**, 730–739 (2008).
87. Qi, G.-B., Gao, Y.-J., Wang, L. & Wang, H. Self-Assembled Peptide-Based Nanomaterials for Biomedical Imaging and Therapy. *Adv. Mater.* **30**, 1703444 (2018).
88. Webber, M. J., Kessler, J. A. & Stupp, S. I. Emerging peptide nanomedicine to regenerate tissues and organs. *J. Intern. Med.* **267**, 71–88 (2010).
89. Cui, H., Webber, M. J. & Stupp, S. I. Self-assembly of peptide amphiphiles: from molecules to nanostructures to biomaterials. *Biopolymers* **94**, 1–18 (2010).
90. Zhang, P., Cheetham, A. G., Lin, Y. & Cui, H. Self-Assembled Tat Nanofibers as Effective Drug Carrier and Transporter. *ACS Nano* **7**, 5965–5977 (2013).
91. Frankel, A. D. & Pabo, C. O. Cellular uptake of the tat protein from human immunodeficiency virus. *Cell* **55**, 1189–1193 (1988).
92. Lim, Y. B., Lee, E. & Lee, M. Controlled bioactive nanostructures from self-assembly of peptide building blocks. *Angew. Chemie - Int. Ed.* **46**, 9011–9014 (2007).
93. Conticello, V. P., Hughes, S. & Modlin, C. Biomaterials Made from Coiled-Coil Peptides. in *Fibrous Proteins: Structures and Mechanisms* 575–600 (2017). doi:10.1007/978-3-319-49674-0_17
94. Mehrban, N. *et al.* Functionalized α-Helical Peptide Hydrogels for Neural Tissue Engineering. *ACS Biomater. Sci. Eng.* **1**, 431–439 (2015).
95. Gajjeraman, S., He, G., Narayanan, K. & George, A. Biological Assemblies Provide Novel Templates for the Synthesis of Biocomposites and Facilitate Cell Adhesion. *Adv. Funct. Mater.* **18**, 3972–3980 (2008).
96. Huang, C.-C., Ravindran, S., Yin, Z. & George, A. 3-D self-assembling leucine zipper hydrogel with tunable properties for tissue engineering. *Biomaterials* **35**, 5316–5326 (2014).
97. Zacco, E. *et al.* A Self-Assembling Peptide Scaffold for the Multivalent Presentation of Antigens. *Biomacromolecules* **16**, 2188–2197 (2015).
98. Adamo, R. *et al.* Synthetically defined glycoprotein vaccines: Current status and future directions. *Chem. Sci.* **4**, 2995–3008 (2013).
99. Apostolovic, B., Deacon, S. P. E., Duncan, R. & Klok, H.-A. Hybrid Polymer Therapeutics Incorporating Bioresponsive, Coiled Coil Peptide Linkers. *Biomacromolecules* **11**, 1187–1195 (2010).
100. Apostolovic, B., Deacon, S. P. E., Duncan, R. & Klok, H.-A. Cell Uptake and Trafficking Behavior of Non-covalent, Coiled-coil Based Polymer–Drug Conjugates. *Macromol. Rapid Commun.* **32**, 11–18 (2011).
101. Ding, L., Jiang, Y., Zhang, J., Klok, H.-A. & Zhong, Z. pH-Sensitive Coiled-Coil Peptide-Cross-Linked Hyaluronic Acid Nanogels: Synthesis and Targeted Intracellular Protein Delivery to CD44 Positive Cancer Cells. *Biomacromolecules* **19**, 555–562 (2018).

102. Litowski, J. R. & Hodges, R. S. Designing heterodimeric two-stranded α-helical coiled-coils. Effects of hydrophobicity and α-helical propensity on protein folding, stability, and specificity. *J. Biol. Chem.* **277**, 37272–37279 (2002).
103. Apostolovic, B. & Klok, H.-A. pH-Sensitivity of the E3/K3 Heterodimeric Coiled Coil. *Biomacromolecules* **9**, 3173–3180 (2008).
104. Yao, M. H. *et al.* Polypeptide-engineered physical hydrogels designed from the coiled-coil region of cartilage oligomeric matrix protein for three-dimensional cell culture. *J. Mater. Chem. B* **2**, 3123–3132 (2014).
105. Mikolajczak, D. J., Heier, J. L., Schade, B. & Koksch, B. Catalytic Activity of Peptide–Nanoparticle Conjugates Regulated by a Conformational Change. *Biomacromolecules* **18**, 3557–3562 (2017).
106. Mikolajczak, D. J., Scholz, J. & Koksch, B. Tuning the Catalytic Activity and Substrate Specificity of Peptide-Nanoparticle Conjugates. *ChemCatChem* **10**, 5665–5668 (2018).
107. Mikolajczak, D. J. & Koksch, B. Peptide-Gold Nanoparticle Conjugates as Sequential Cascade Catalysts. *ChemCatChem* **10**, 4324–4328 (2018).
108. Müller, K., Faeh, C. & Diederich, F. Fluorine in Pharmaceuticals: Looking Beyond Intuition. *Science.* **317**, 1881–1886 (2007).
109. Zhang, Q., Kelly, M. A., Bauer, N. & You, W. The Curious Case of Fluorination of Conjugated Polymers for Solar Cells. *Acc. Chem. Res.* **50**, 2401–2409 (2017).
110. Stuart, A. C. *et al.* Fluorine substituents reduce charge recombination and drive structure and morphology development in polymer solar cells. *J. Am. Chem. Soc.* **135**, 1806–1815 (2013).
111. Berger, R., Resnati, G., Metrangolo, P., Weber, E. & Hulliger, J. Organic fluorine compounds: A great opportunity for enhanced materials properties. *Chem. Soc. Rev.* **40**, 3496–3508 (2011).
112. Brooks, A. F., Topczewski, J. J., Ichiishi, N., Sanford, M. S. & Scott, P. J. H. Late-stage [18 F]fluorination: new solutions to old problems. *Chem. Sci.* **5**, 4545–4553 (2014).
113. Studer, A. *et al.* Fluorous synthesis: A fluorous-phase strategy for improving separation efficiency in organic synthesis. *Science.* **275**, 823–826 (1997).
114. Zhang, W. Fluorous Linker-Facilitated Chemical Synthesis. *Chem. Rev.* **109**, 749–795 (2009).
115. Fustero, S., Sedgwick, D. M., Román, R. & Barrio, P. Recent advances in the synthesis of functionalised monofluorinated compounds. *Chem. Commun.* **54**, 9706–9725 (2018).
116. Marsh, E. N. G. & Suzuki, Y. Using 19F NMR to probe biological interactions of proteins and peptides. *ACS Chem. Biol.* **9**, 1242–1250 (2014).
117. Chen, H., Viel, S., Ziarelli, F. & Peng, L. F NMR: A valuable tool for studying biological events. *Chem. Soc. Rev.* **42**, 7971–7982 (2013).
118. Ruiz-Cabello, J., Barnett, B. P., Bottomley, P. A. & Bulte, J. W. M. Fluorine (19F) MRS and MRI in biomedicine. *NMR Biomed.* **24**, 114–129 (2011).
119. Tirotta, I. *et al.* F Magnetic Resonance Imaging (MRI): From Design of Materials to Clinical Applications. *Chem. Rev.* **115**, 1106−1129 (2015).
120. Purser, S., Moore, P. R., Swallow, S. & Gouverneur, V. Fluorine in medicinal chemistry. *Chem. Soc. Rev.* **37**, 320–330 (2008).
121. Wang, J. *et al.* Fluorine in pharmaceutical industry: Fluorine-containing drugs

introduced to the market in the last decade (2001-2011). *Chem. Rev.* **114**, 2432–2506 (2014).
122. Jeschke, P. The unique role of fluorine in the design of active ingredients for modern crop protection. *ChemBioChem* **5**, 570–589 (2004).
123. Jeschke, P. The unique role of halogen substituents in the design of modern agrochemicals. *Pest Manag. Sci.* **66**, 10–27 (2010).
124. Berger, A. A., Völler, J. S., Budisa, N. & Koksch, B. Deciphering the Fluorine Code - The Many Hats Fluorine Wears in a Protein Environment. *Acc. Chem. Res.* **50**, 2093–2103 (2017).
125. O'Hagan, D. Understanding organofluorine chemistry. An introduction to the C-F bond. *Chem. Soc. Rev.* **37**, 308–319 (2008).
126. Bondi, A. van der Waals Volumes and Radii. *J. Phys. Chem.* **68**, 441–451 (1964).
127. Smart, B. E. Fluorine substituent effects (on bioactivity). *J. Fluor. Chem.* **109**, 3–11 (2001).
128. Jagodzinska, M., Huguenot, F., Candiani, G. & Zanda, M. Assessing the bioisosterism of the trifluoromethyl group with a protease probe. *ChemMedChem* **4**, 49–51 (2009).
129. Meanwell, N. A. Fluorine and Fluorinated Motifs in the Design and Application of Bioisosteres for Drug Design. *J. Med. Chem.* **61**, 5822–5880 (2018).
130. Hesler, C. B., Swenson, T. L. & Tall, A. R. Purification and characterization of a human plasma cholesteryl ester transfer protein. *J. Biol. Chem.* **262**, 2275–2282 (1987).
131. Massa, M. A. *et al.* Novel heteroaryl replacements of aromatic 3-tetrafluoroethoxy substituents in trifluoro-3-(tertiaryamino)-2-propanols as potent inhibitors of cholesteryl ester transfer protein. *Bioorg. Med. Chem. Lett.* **11**, 1625–1628 (2001).
132. Yamazaki, T., Taguchi, T. & Ojima, I. *Unique Properties of Fluorine and their Relevance to Medicinal Chemistry and Chemical Biology*. *Fluorine in Medicinal Chemistry and Chemical Biology* (2009). doi:10.1002/9781444312096.ch1
133. Schlosser, M. Parametrization of Substituents: Effects of Fluorine and Other Heteroatoms on OH, NH, and CH Acidities. *Angew. Chemie Int. Ed.* **37**, 1496–1513 (1998).
134. Böhm, H.-J. *et al.* Fluorine in medicinal chemistry. *ChemBioChem* **5**, 637–43 (2004).
135. O'Hagan, D. Fluorine in health care: Organofluorine containing blockbuster drugs. *J. Fluor. Chem.* **131**, 1071–1081 (2010).
136. Hoveyda, H. R. *et al.* Optimization of the Potency and Pharmacokinetic Properties of a Macrocyclic Ghrelin Receptor Agonist (Part I): Development of Ulimorelin (TZP-101) from Hit to Clinic. *J. Med. Chem.* **54**, 8305–8320 (2011).
137. Zhou, Y. *et al.* Next Generation of Fluorine-Containing Pharmaceuticals, Compounds Currently in Phase II-III Clinical Trials of Major Pharmaceutical Companies: New Structural Trends and Therapeutic Areas. *Chem. Rev.* **116**, 422–518 (2016).
138. Filler, R. & Novar, H. Fluorinated Aromatic Amino Acids. I. o-, m-, and p-Trifluoromethylphenylalanines 1. *J. Org. Chem.* **25**, 733–736 (1960).
139. Dalvit, C. Ligand- and substrate-based 19F NMR screening: Principles and

applications to drug discovery. *Prog. Nucl. Magn. Reson. Spectrosc.* **51**, 243–271 (2007).
140. Buer, B. C. & Marsh, E. N. G. Fluorine: A new element in protein design. *Protein Sci.* **21**, 453–462 (2012).
141. Marsh, E. N. G. Fluorinated proteins: From design and synthesis to structure and stability. *Acc. Chem. Res.* **47**, 2878–2886 (2014).
142. Salwiczek, M., Nyakatura, E. K., Gerling, U. I. M., Ye, S. & Koksch, B. Fluorinated amino acids: compatibility with native protein structures and effects on protein–protein interactions. *Chem. Soc. Rev.* **41**, 2135–2171 (2012).
143. Jäckel, C. & Koksch, B. Fluorine in peptide design and protein engineering. *European J. Org. Chem.* 4483–4503 (2005). doi:10.1002/ejoc.200500205
144. Huhmann, S. & Koksch, B. Fine-tuning the proteolytic stability of peptides with fluorinated amino acids. *European J. Org. Chem.* 3667–3679 (2018). doi:10.1002/ejoc.201800803
145. Agostini, F. *et al.* Biocatalysis with Unnatural Amino Acids: Enzymology Meets Xenobiology. *Angew. Chemie - Int. Ed.* **56**, 9680–9703 (2017).
146. Vukelić, S. *et al.* Synthesis of Side Chain Fluorinated Amino Acids and Their Effects on the Properties of Peptides and Proteins. in *Modern Synthesis Processes and Reactivity of Fluorinated Compounds* 427–464 (Elsevier, 2017). doi:10.1016/B978-0-12-803740-9.00015-9
147. Samsonov, S. A., Salwiczek, M., Anders, G., Koksch, B. & Pisabarro, M. T. Fluorine in protein environments: A QM and MD study. *J. Phys. Chem. B* **113**, 16400–16408 (2009).
148. Erdbrink, H. *et al.* Synthesis of enantiomerically pure (2S,3S)-5,5,5-trifluoroisoleucine and (2R,3S)-5,5,5-trifluoro-allo-isoleucine. *Beilstein J. Org. Chem.* **9**, 2009–2014 (2013).
149. Gerling, U. I. M. *et al.* Fluorinated amino acids in amyloid formation: a symphony of size, hydrophobicity and α-helix propensity. *Chem. Sci.* **5**, 819–830 (2014).
150. Huhmann, S. Stabilization of peptides by site-specific incorporation of fluorinated amino acids: Model studies and the development of fluorinated, peptide-based HIV-1 fusion inhibitors. (Freie Universität Berlin, 2018).
151. Robalo, J. R., Huhmann, S., Koksch, B. & Vila Verde, A. The Multiple Origins of the Hydrophobicity of Fluorinated Apolar Amino Acids. *Chem* **3**, 881–897 (2017).
152. Chiu, H.-P. *et al.* Helix propensity of highly fluorinated amino acids. *J. Am. Chem. Soc.* **128**, 15556–15557 (2006).
153. Chiu, H.-P. & Cheng, R. P. Chemoenzymatic Synthesis of (S)-Hexafluoroleucine and (S)-Tetrafluoroleucine. *Org. Lett.* **9**, 5517–5520 (2007).
154. Erdbrink, H. *et al.* Conjugate hydrotrifluoromethylation of α,β-unsaturated acyl-oxazolidinones: Synthesis of chiral fluorinated amino acids. *Org. Biomol. Chem.* **10**, 8583–8586 (2012).
155. Tang, Y. *et al.* Stabilization of Coiled-Coil Peptide Domains by Introduction of Trifluoroleucine. *Biochemistry* **40**, 2790–2796 (2001).
156. Son, S., Tanrikulu, I. C. & Tirrell, D. A. Stabilization of bzip peptides through incorporation of fluorinated aliphatic residues. *ChemBioChem* **7**, 1251–1257 (2006).

157. Bilgiçer, B., Fichera, A. & Kumar, K. A Coiled Coil with a Fluorous Core. *J. Am. Chem. Soc.* **123**, 4393–4399 (2001).
158. Bilgiçer, B., Xing, X. & Kumar, K. Programmed Self-Sorting of Coiled Coils with Leucine and Hexafluoroleucine Cores. *J. Am. Chem. Soc.* **123**, 11815–11816 (2001).
159. Lee, K. H., Lee, H. Y., Slutsky, M. M., Anderson, J. T. & Marsh, E. N. G. Fluorous effect in proteins: De novo design and characterization of a four-α-helix bundle protein containing hexafluoroleucine. *Biochemistry* **43**, 16277–16284 (2004).
160. Lee, H. Y., Lee, K. H., Al-Hashimi, H. M. & Marsh, E. N. G. Modulating protein structure with fluorous amino acids: Increased stability and native-like structure conferred on a 4-helix bundle protein by hexafluoroleucine. *J. Am. Chem. Soc.* **128**, 337–343 (2006).
161. Buer, B. C., De La Salud-Bea, R., Al Hashimi, H. M. & Marsh, E. N. G. Engineering protein stability and specificity using fluorous amino acids: The importance of packing effects. *Biochemistry* **48**, 10810–10817 (2009).
162. Buer, B. C., Meagher, J. L., Stuckey, J. A. & Marsh, E. N. G. Structural basis for the enhanced stability of highly fluorinated proteins. *Proc. Natl. Acad. Sci.* **109**, 4810–4815 (2012).
163. Buer, B. C., Meagher, J. L., Stuckey, J. A. & Marsh, E. N. G. Comparison of the structures and stabilities of coiled-coil proteins containing hexafluoroleucine and t-butylalanine provides insight into the stabilizing effects of highly fluorinated amino acid side-chains. *Protein Sci.* **21**, 1705–1715 (2012).
164. Buer, B. C., Levin, B. J. & Marsh, E. N. G. Influence of fluorination on the thermodynamics of protein folding. *J. Am. Chem. Soc.* **134**, 13027–13034 (2012).
165. Montclare, J. K. & Tirrell, D. A. Evolving Proteins of Novel Composition. *Angew. Chemie Int. Ed.* **45**, 4518–4521 (2006).
166. Panchenko, T., Zhu, W. W. & Montclare, J. K. Influence of global fluorination on chloramphenicol acetyltransferase activity and stability. *Biotechnol. Bioeng.* **94**, 921–930 (2006).
167. Jäckel, C., Seufert, W., Thust, S. & Koksch, B. Evaluation of the molecular interactions of fluorinated amino acids with native polypeptides. *ChemBioChem* **5**, 717–720 (2004).
168. Jäckel, C., Salwiczek, M. & Koksch, B. Fluorine in a native protein environment - How the spatial demand and polarity of fluoroalkyl groups affect protein folding. *Angew. Chemie - Int. Ed.* **45**, 4198–4203 (2006).
169. Salwiczek, M. & Koksch, B. Effects of fluorination on the folding kinetics of a heterodimeric coiled coil. *ChemBioChem* **10**, 2867–2870 (2009).
170. Salwiczek, M. *et al.* Position-Dependent Effects of Fluorinated Amino Acids on the Hydrophobic Core Formation of a Heterodimeric Coiled Coil. *Chem. - A Eur. J.* **15**, 7628–7636 (2009).
171. Vagt, T., Nyakatura, E., Salwiczek, M., Jäckel, C. & Koksch, B. Towards identifying preferred interaction partners of fluorinated amino acids within the hydrophobic environment of a dimeric coiled coil peptide. *Org. Biomol. Chem.* **8**, 1382 (2010).
172. Nyakatura, E. K., Reimann, O., Vagt, T., Salwiczek, M. & Koksch, B. Accommodating fluorinated amino acids in a helical peptide environment.

RSC Adv. **3**, 6319 (2013).
173. Huhmann, S. *et al.* Effects of single substitutions with hexafluoroleucine and trifluorovaline on the hydrophobic core formation of a heterodimeric coiled coil. *J. Fluor. Chem.* **175**, 32–35 (2015).
174. More, H. T., Zhang, K. S., Srivastava, N., Frezzo, J. A. & Montclare, J. K. Influence of Fluorination on Protein-Engineered Coiled-Coil Fibers. *Biomacromolecules* **16**, 1210–1217 (2015).
175. Hume, J. *et al.* Engineered Coiled-Coil Protein Microfibers. *Biomacromolecules* **15**, 3503–3510 (2014).
176. Yuvienco, C., More, H. T., Haghpanah, J. S., Tu, R. S. & Montclare, J. K. Modulating supramolecular assemblies and mechanical properties of engineered protein materials by fluorinated amino acids. *Biomacromolecules* **13**, 2273–2278 (2012).
177. L. Villaraza, A. J., Bumb, A. & Brechbiel, M. W. Macromolecules, Dendrimers, and Nanomaterials in Magnetic Resonance Imaging: The Interplay between Size, Function, and Pharmacokinetics. *Chem. Rev.* **110**, 2921–2959 (2010).
178. Holland, G. ., Bottomley, P. . & Hinshaw, W. . 19F magnetic resonance imaging. *J. Magn. Reson.* **28**, 133–136 (1977).
179. Knight, J. C., Edwards, P. G. & Paisey, S. J. Fluorinated contrast agents for magnetic resonance imaging; A review of recent developments. *RSC Adv.* **1**, 1415–1425 (2011).
180. Higuchi, M. *et al.* 19 F and 1 H MRI detection of amyloid β plaques in vivo. *Nat. Neurosci.* **8**, 527–533 (2005).
181. Oishi, M., Sumitani, S. & Nagasaki, Y. On-off regulation of 19F magnetic resonance signals based on pH-sensitive PEGylated nanogels for potential tumor-specific smart 19F MRI probes. *Bioconjug. Chem.* **18**, 1379–1382 (2007).
182. Ahrens, E. T., Flores, R., Xu, H. & Morel, P. A. In vivo imaging platform for tracking immunotherapeutic cells. *Nat. Biotechnol.* **23**, 983 (2005).
183. Srinivas, M., Morel, P. A., Ernst, L. A., Laidlaw, D. H. & Ahrens, E. T. Fluorine-19 MRI for visualization and quantification of cell migration in a diabetes model. *Magn. Reson. Med.* **58**, 725–734 (2007).
184. Waiczies, S. *et al.* Enhanced Fluorine-19 MRI Sensitivity using a Cryogenic Radiofrequency Probe: Technical Developments and Ex Vivo Demonstration in a Mouse Model of Neuroinflammation. *Sci. Rep.* **7**, 1–10 (2017).
185. Waiczies, H. *et al.* Visualizing brain inflammation with a shingled-leg radio-frequency head probe for 19F/1H MRI. *Sci. Rep.* **3**, 1280 (2013).
186. Kirberger, S. E. *et al.* Synthesis of Intrinsically Disordered Fluorinated Peptides for Modular Design of High-Signal 19 F MRI Agents. *Angew. Chemie - Int. Ed.* **56**, 6440–6444 (2017).
187. Maki, J. *et al.* The MR tracking of transplanted ATDC5 cells using fluorinated poly-l-lysine-CF3. *Biomaterials* **28**, 434–440 (2007).
188. Mizukami, S. *et al.* Paramagnetic relaxation-based 19F MRI probe to detect protease activity. *J. Am. Chem. Soc.* **130**, 794–795 (2008).
189. Mizukami, S., Takikawa, R., Sugihara, F., Shirakawa, M. & Kikuchi, K. Dual-function probe to detect protease activity for fluorescence measurement and 19F MRI. *Angew. Chemie - Int. Ed.* **48**, 3641–3643 (2009).
190. Falenski, J. A., Gerling, U. I. M. & Koksch, B. Multiple glycosylation of de novo designed alpha-helical coiled coil peptides. *Bioorganic Med. Chem.* **18**, 3703–

3706 (2010).
191. Shindy, H. A. Fundamentals in the chemistry of cyanine dyes: A review. *Dye. Pigment.* **145**, 505–513 (2017).
192. Luo, S., Zhang, E., Su, Y., Cheng, T. & Shi, C. A review of NIR dyes in cancer targeting and imaging. *Biomaterials* **32**, 7127–7138 (2011).
193. Kim, J., Watson, A., Henary, M. & Patonay, G. Near-Infrared Cyanine Dye – Protein Interactions. *Top. Heterocycl. Chem.* **14**, 31–39 (2008).
194. Cooper, M. E., Gregory, S., Adie, E. & Kalinka, S. pH-Sensitive Cyanine Dyes for Biological Applications. *J. Fluoresc.* **12**, 425–429 (2002).
195. Armitage, B. A. Cyanine dye-DNA interactions: Intercalation, groove binding, and aggregation. in *Topics in Current Chemistry* **253**, 55–76 (2005).
196. Spano, F. C. The Spectral Signatures of Frenkel Polarons in H- and J-Aggregates. *Acc. Chem. Res.* **43**, 429–439 (2010).
197. Berlepsch, H. V., Brandenburg, E., Koksch, B. & Böttcher, C. Peptide adsorption to cyanine dye aggregates revealed by cryo-transmission electron microscopy. *Langmuir* **26**, 11452–11460 (2010).
198. Audain, E., Ramos, Y., Hermjakob, H., Flower, D. R. & Perez-Riverol, Y. Accurate estimation of isoelectric point of protein and peptide based on amino acid sequences. *Bioinformatics* **32**, 821–827 (2016).
199. Thurlkill, R. L., Grimsley, G. R., Scholtz, J. M. & Pace, C. N. pK values of the ionizable groups of proteins. *Protein Sci.* **15**, 1214–1218 (2006).
200. Nozaki, Y. & Tanford, C. B. T.-M. in E. Examination of titration behavior. in *Enzyme Structure* **11**, 715–734 (Academic Press, 1967).
201. Baumeister, W. Electron tomography: towards visualizing the molecular organization of the cytoplasm. *Curr. Opin. Struct. Biol.* **12**, 679–684 (2002).
202. Schöne, D., Schade, B., Böttcher, C. & Koksch, B. Impact of multivalent charge presentation on peptide-nanoparticle aggregation. *Beilstein J. Org. Chem.* **11**, 792–803 (2015).
203. Long, M. M., Urry, D. W. & Stoeckenius, W. Circular dichroism of biological membranes: purple membrane of Halobacterium halobium. *Biochem Biophys Res Commun* **75**, 725–731 (1977).
204. Benjwal, S. Monitoring protein aggregation during thermal unfolding in circular dichroism experiments. *Protein Sci.* **15**, 635–639 (2006).
205. McLachlan, A. D. & Stewart, M. Tropomyosin coiled-coil interactions: Evidence for an unstaggered structure. *J. Mol. Biol.* **98**, 293–304 (1975).
206. O'Neil, K. & DeGrado, W. F. A thermodynamic scale for the helix-forming tendencies of the commonly occurring amino acids. *Science.* **250**, 646–651 (1990).
207. Lau, S. Y., Taneja, a K. & Hodges, R. S. Synthesis of a model protein of defined secondary and quaternary structure. Effect of chain length on the stabilization and formation of two-stranded alpha-helical coiled-coils. *J. Biol. Chem.* **259**, 13253–13261 (1984).
208. Zhou, N. E., Zhu, B. -Y, Kay, C. M. & Hodges, R. S. The two-stranded α-helical coiled-coil is an ideal model for studying protein stability and subunit interactions. *Biopolymers* **32**, 419–426 (1992).
209. Yu, Y., Monera, O. D., Hodges, R. S. & Privalov, P. L. Ion pairs significantly stabilize coiled-coils in the absence of electrolyte. *J. Mol. Biol.* **255**, 367–372 (1996).
210. Krylov, D., Barchi, J. & Vinson, C. Inter-helical interactions in the leucine

zipper coiled coil dimer: pH and salt dependence of coupling energy between charged amino acids. *J. Mol. Biol.* **279**, 959–972 (1998).
211. Riddiford, L. M. & Scheraga, H. A. Structural Studies of Paramyosin. II. Conformational Changes *. *Biochemistry* **1**, 108–114 (1962).
212. O'Shea, E. K., Lumb, K. J. & Kim, P. S. Peptide 'Velcro': Design of a heterodimeric coiled coil. *Curr. Biol.* **3**, 658–667 (1993).
213. Kohn, W. D., Monera, O. D., Kay, C. M. & Hodges, R. S. The effects of interhelical electrostatic repulsions between glutamic acid residues in controlling the dimerization and stability of two-stranded α- helical coiled-coils. *J. Biol. Chem.* **270**, 25495–25506 (1995).
214. Mustroph, H. *et al.* Relationship between the molecular structure of merocyanine dyes and the vibrational fine structure of their electronic absorption spectra. *Angew. Chemie - Int. Ed.* **48**, 8773–8775 (2009).
215. Berlepsch, H. V. & Böttcher, C. H-Aggregates of an Indocyanine Cy5 Dye: Transition from Strong to Weak Molecular Coupling. *J. Phys. Chem. B* **119**, 11900–11909 (2015).
216. Wallimann, P., Kennedy, R. J., Miller, J. S., Shalongo, W. & Kemp, D. S. Dual wavelength parametric test of two-state models for circular dichroism spectra of helical polypeptides: Anomalous dichroic properties of alanine-rich peptides. *J. Am. Chem. Soc.* **125**, 1203–1220 (2003).
217. Wang, D., Chen, K., Kulp, J. L. & Arora, P. S. Evaluation of biologically relevant short α-helices stabilized by a main-chain hydrogen-bond surrogate. *J. Am. Chem. Soc.* **128**, 9248–9256 (2006).
218. Elcock, A. H. The stability of salt bridges at high temperatures: Implications for hyperthermophilic proteins. *J. Mol. Biol.* **284**, 489–502 (1998).
219. Gsponer, J. & Vendruscolo, M. Theoretical approaches to protein aggregation. *Protein Pept. Lett.* **13**, 287–293 (2006).
220. Hwang, W., Zhang, S., Kamm, R. D. & Karplus, M. Kinetic control of dimer structure formation in amyloid fibrillogenesis. *Proc. Natl. Acad. Sci.* **101**, 12916–12921 (2004).
221. Chan, D. I., Prenner, E. J. & Vogel, H. J. Tryptophan- and arginine-rich antimicrobial peptides: Structures and mechanisms of action. *Biochim. Biophys. Acta - Biomembr.* **1758**, 1184–1202 (2006).
222. Dougherty, D. A. Cation-pi Interactions in Chemistry and Biology: A New View of Benzene, Phe, Tyr, and Trp. *Science.* **271**, 163–168 (1996).
223. Hu, W. & Cross, T. A. Tryptophan Hydrogen Bonding and Electric Dipole Moments: Functional Roles in the Gramicidin Channel and Implications for Membrane Proteins. *Biochemistry* **34**, 14147–14155 (1995).
224. Falcone, N. *et al.* A Ferrocene–Tryptophan Conjugate: The Role of the Indolic Nitrogen in Supramolecular Assembly. *Chempluschem* **82**, 1282–1289 (2017).
225. Gallivan, J. P. & Dougherty, D. A. Cation-pi interactions in structural biology. *Proc. Natl. Acad. Sci.* **96**, 9459–9464 (1999).
226. Pace, C. N. & Scholtz, J. M. A helix propensity scale based on experimental studies of peptides and proteins. *Biophys. J.* **75**, 422–427 (1998).
227. Javid, N. *et al.* Cooperative Self-Assembly of Peptide Gelators and Proteins. *Biomacromolecules* **14**, 4368–4376 (2013).
228. Marqusee, S. & Baldwin, R. L. Helix stabilization by Glu-...Lys+ salt bridges in short peptides of de novo design. *Proc. Natl. Acad. Sci. U. S. A.* **84**, 8898–

8902 (1987).
229. Scholtz, J. M. *et al.* Calorimetric determination of the enthalpy change for the alpha-helix to coil transition of an alanine peptide in water. *Proc. Natl. Acad. Sci.* **88**, 2854–2858 (1991).
230. Weerakkody, D. *et al.* Novel pH-Sensitive Cyclic Peptides. *Sci. Rep.* **6**, 31322 (2016).
231. Lambers, H., Piessens, S., Bloem, A., Pronk, H. & Finkel, P. Natural skin surface pH is on average below 5, which is beneficial for its resident flora. *Int. J. Cosmet. Sci.* **28**, 359–370 (2006).
232. Zhou, N. E., Kay, C. M. & Hodges, R. S. Synthetic model proteins. Positional effects of interchain hydrophobic interactions on stability of two-stranded alpha-helical coiled-coils. *J. Biol. Chem.* **267**, 2664–70 (1992).
233. Hu, J. C., O'Shea, E. K., Kim, P. S. & Sauer, R. T. Sequence requirements for coiled-coils: Analysis with λ repressor-GCN4 leucine zipper fusions. *Science.* **250**, 1400–1403 (1990).
234. Zhu, B.-Y., Zhou, M. E., Kay, C. M. & Hodges, R. S. Packing and hydrophobicity effects on protein folding and stability: Effects of β-branched amino acids, valine and isoleucine, on the formation and stability of two-stranded α-helical coiled coils/leucine zippers. *Protein Sci.* **2**, 383–394 (1992).
235. Zhao, Y. H., Abraham, M. H. & Zissimos, A. M. Fast Calculation of van der Waals Volume as a Sum of Atomic and Bond Contributions and Its Application to Drug Compounds. *J. Org. Chem.* **68**, 7368–7373 (2003).
236. Kwon, O.-H. *et al.* Hydration dynamics at fluorinated protein surfaces. *Proc. Natl. Acad. Sci.* **107**, 17101–17106 (2010).
237. Creamer, T. P. & Rose, G. D. Side-chain entropy opposes alpha-helix formation but rationalizes experimentally determined helix-forming propensities. *Proc. Natl. Acad. Sci.* **89**, 5937–5941 (1992).
238. Kukhar, V. P. Fluorine-containing amino acids. *J. Fluor. Chem.* **69**, 199–205 (1994).
239. Zacco, E. *et al.* Tailored Presentation of Carbohydrates on a Coiled Coil-Based Scaffold for Asialoglycoprotein Receptor Targeting. *ACS Chem. Biol.* **10**, 2065–2072 (2015).
240. Chakrabartty, A., Kortemme, T. & Baldwin, R. L. Helix propensities of the amino acids measured in alanine-based peptides without helix-stabilizing side-chain interactions. *Protein Sci.* **3**, 843–852 (1994).
241. Chakrabartty, A., Kortemme, T. & Baldwin, R. L. Helix propensities of the amino acids measured in alanine-based peptides without helix-stabilizing side-chain interactions. *Protein Sci.* **3**, 843–852 (2008).
242. Wood, C. W. & Woolfson, D. N. CCBuilder 2.0: Powerful and accessible coiled-coil modeling. *Protein Sci.* **27**, 103–111 (2017).
243. Trapp, B. D. & Nave, K.-A. Multiple Sclerosis: An Immune or Neurodegenerative Disorder? *Annu. Rev. Neurosci.* **31**, 247–269 (2008).
244. Wallin, M. T. *et al.* Global, regional, and national burden of multiple sclerosis 1990–2016: a systematic analysis for the Global Burden of Disease Study 2016. *Lancet Neurol.* **18**, 269–285 (2019).
245. Baranzini, S. E. & Oksenberg, J. R. The Genetics of Multiple Sclerosis: From 0 to 200 in 50 Years. *Trends Genet.* **33**, 960–970 (2017).
246. Constantinescu, C. S., Farooqi, N., O'Brien, K. & Gran, B. Experimental autoimmune encephalomyelitis (EAE) as a model for multiple sclerosis (MS).

Br. J. Pharmacol. **164**, 1079–1106 (2011).
247. Nakahara, J., Maeda, M., Aiso, S. & Suzuki, N. Current concepts in multiple sclerosis: Autoimmunity versus oligodendrogliopathy. *Clin. Rev. Allergy Immunol.* **42**, 26–34 (2012).
248. Reindl, M. & Waters, P. Myelin oligodendrocyte glycoprotein antibodies in neurological disease. *Nat. Rev. Neurol.* **15**, 89–102 (2019).
249. Pham-Dinh, D. *et al.* Myelin/oligodendrocyte glycoprotein is a member of a subset of the immunoglobulin superfamily encoded within the major histocompatibility complex. *Proc. Natl. Acad. Sci.* **90**, 7990–7994 (2006).
250. Brunner, C., Lassmann, H., Waehneldt, T. V., Matthieu, J. -M & Linington, C. Differential Ultrastructural Localization of Myelin Basic Protein, Myelin/Oligodendroglial Glycoprotein, and 2′,3′-Cyclic Nucleotide 3′-Phosphodiesterase in the CNS of Adult Rats. *J. Neurochem.* **52**, 296–304 (1989).
251. Ethofer, T. *et al.* Comparison of longitudinal metabolite relaxation times in different regions of the human brain at 1.5 and 3 Tesla. *Magn. Reson. Med.* **50**, 1296–1301 (2003).
252. Zhang, C. *et al.* Self-Assembled Peptide Nanofibers Designed as Biological Enzymes for Catalyzing Ester Hydrolysis. *ACS Nano* **8**, 11715–11723 (2014).
253. Gao, Y., Zhao, F., Wang, Q., Zhang, Y. & Xu, B. Small peptide nanofibers as the matrices of molecular hydrogels for mimicking enzymes and enhancing the activity of enzymes. *Chem. Soc. Rev.* **39**, 3425–3433 (2010).
254. Heier, J. L. De novo self-assembling peptides possessing esterase properties. (Freie Universität Berlin, 2015).
255. Merrifield, R. B. Solid Phase Peptide Synthesis. I. The Synthesis of a Tetrapeptide. *J. Am. Chem. Soc.* **85**, 2149–2154 (1963).
256. *Circular Dichroism and the Conformational Analysis of Biomolecules*. (Springer US, 1996). doi:10.1007/978-1-4757-2508-7
257. Greenfield, N. J. Using circular dichroism spectra to estimate protein secondary structure. *Nat. Protoc.* **1**, 2876–2890 (2006).
258. Greenfield, N. J. Analysis of Circular Dichroism Data. *Methods Enzymol.* **383**, 282–317 (2004).
259. Greenfield, N. J. Applications of circular dichroism in protein and peptide analysis. *TrAC - Trends Anal. Chem.* **18**, 236–244 (1999).
260. Chen, Y.-H., Yang, J. T. & Chau, K. H. Determination of the helix and β form of proteins in aqueous solution by circular dichroism. *Biochemistry* **13**, 3350–3359 (1974).
261. Gans, P. J., Lyu, P. C., Manning, M. C., Woody, R. W. & Kallenbach, N. R. The helix–coil transition in heterogeneous peptides with specific side-chain interactions: Theory and comparison with CD spectral data. *Biopolymers* **31**, 1605–1614 (1991).
262. Anthis, N. J. & Clore, G. M. Sequence-specific determination of protein and peptide concentrations by absorbance at 205 nm. *Protein Sci.* **22**, 851–858 (2013).
263. Inkson, B. J. *Scanning Electron Microscopy (SEM) and Transmission Electron Microscopy (TEM) for Materials Characterization*. *Materials Characterization Using Nondestructive Evaluation (NDE) Methods* (Elsevier Ltd, 2016). doi:10.1016/B978-0-08-100040-3.00002-X
264. Kiselev, N. A., Sherman, M. B. & Tsuprun, V. L. Negative staining of proteins.

Electron Microsc. Rev. **3**, 43–72 (1990).
265. Kühlbrandt, W. Cryo-EM enters a new era. *Elife* **3**, e03665 (2014).
266. Schneider, C. A., Rasband, W. S. & Eliceiri, K. W. NIH Image to ImageJ: 25 years of image analysis. *Nat. Methods* **9**, 671–675 (2012).
267. Jackson, M. & Mantsch, H. H. The use and misuse of FTIR spectroscopy in the determination of protein structure. *Crit. Rev. Biochem. Mol. Biol.* **30**, 95–120 (1995).